MINISTRY OF EDUCATION AND TRAINING
VIETNAM ACADEMY OF SCIENCE AND TECHNOLOGY

GRADUATE UNIVERSITY OF SCIENCE AND TECHNOLOGY

NGUYEN THANH PHU

DEVELOPMENT OF A TARGETED NANOGELS SYSTEM BASED ON FUCOIDAN-POLOXAMER CONJUGATED FOLIC ACID FOR CO-DELIVERY CHEMOTHERAPEUTIC DRUGS

MASTER DISSERTATION ON MATERIAL SCIENCE

Major: Organic chemistry

Code: 8 44 01 14

SUPERVIORS:

Supervisor 1	Supervisor 2
PhD.Pham Dinh Chuong	PhD.Le Thi Phuong

Ho Chi Minh - 2026

DECLARATION

I hereby declare that this thesis is entirely my own work, carried out based on materials and data that I have independently collected and studied. The results presented are truthful, objective, and have not been previously published in any other study. All data and findings in this thesis are accurate and reliable, and I take full legal responsibility for any errors or misrepresentations.

Ho Chi Minh, Jun 15th, 2026

Master student

Nguyen Thanh Phu

ACKNOWLEDGEMENTS

I would like to express my sincere gratitude to the Graduate University of Science and Technology, Vietnam Academy of Science and Technology, for providing me with the invaluable opportunity to study and develop academically during the studied period from 2024 to 2026.

My deepest appreciation goes to PhD. Pham Dinh Chuong and PhD. Le Thi Phuong for dedicated supervision throughout this research. Their profound expertise, insightful guidance, and continuous encouragement have been instrumental in helping me overcome challenges and successfully complete this work.

I also gratefully acknowledge the Department of Natural Active Ingredient Technology, Institute of Advanced Technology, Vietnam Academy of Science and Technology, for providing essential chemicals, instrumentation, and laboratory facilities that were critical to the successful completion of this study.

Finally, I would like to extend my heartfelt thanks to my family and friends for their unwavering support, encouragement, and understanding throughout my academic journey and research process.

TABLE OF CONTENTS

LIST OF ABBREVIATION

Abbreviation	Meanings
^{1}H-NMR	Proton nuclear magnetic resonance
ATP	Adenosine triphosphate
Cis	Cisplatin
CMC	Critical micelle concentration
Cur	Curcumin
DIW	Deionized Water
DLS	Dynamic light scattering
EPR	Enhanced Permeability and Retention
FA	Folic acid
FDA	Food and Drug Administration
FTIR	Fourier-transform infrared spectroscopy
ICP-MS	Inductively coupled plasma mass spectrometry
LCST	Lower critical solution temperature
MCF-7	Michigan Cancer Foudation-7
MDR	Multi-drug resistance
MDT	Mean dissolution time
MWCO	Molecular weight cut-off
NF-κB	Nuclear factor kappa B
PBS	Phosphate-buffered saline
PDI	Polydispersity Index
PEO	Poly(ethylene oxide)
PPO	Poly(propylene oxide)
ROS	reactive oxygen species
TBNS	2,4,6-trinitrobenzenesulfonic acid
TEM	Transmission Electrons Microscope
UCST	Upper critical solution temperature
UV-Vis	Ultraviolet-visible spectroscopy
WHO	World Health Organization

LIST OF TABLES

LIST OF FIGURES

ABSTRACT

Multi-drug delivery systems offer a promising strategy in cancer therapy by enhancing synergistic effects, improving tumor targeting, and minimizing drug resistance and systemic toxicity. In this study, folic acid-functionalized fucoidan–poloxamer nanogels were developed for the co-delivery of cisplatin and curcumin. Poloxamers P403 was grafted onto fucoidan and functionalized with folic acid, with successful formation confirmed by ^{1}H-NMR, FT-IR, and DLS. Among them, FA-Fud-P403 exhibited a lower CMC and smaller particle size, resulting in superior drug encapsulation efficiency. The nanogels displayed pH-responsive release behavior, featuring an initial burst release under acidic conditions (pH 5.5) followed by sustained diffusion-controlled release. *In vitro* studies showed that dual drug-loaded FA-Fud-P403 significantly enhanced cytotoxicity against MCF-7 cells while reducing toxicity toward normal HDF cells, indicating improved selectivity. Importantly, *in vivo* evaluation in MCF-7 tumor-bearing mice demonstrated that FA-Fud-P403@Cur/Cis achieved the most effective tumor growth inhibition, confirming its superior synergistic therapeutic efficacy and reduced systemic toxicity compared to single-drug formulations.

TÓM TẮT

Hệ dẫn truyền đa thuốc đang nổi lên như một chiến lược hiệu quả trong điều trị ung thư nhờ khả năng tăng cường tác dụng hiệp đồng, nâng cao khả năng hướng đích đến khối u, đồng thời hạn chế tình trạng kháng thuốc và độc tính toàn thân. Trong nghiên cứu này, nanogels trên cơ sở fucoidan–poloxamer được chức năng hóa bằng acid folic đã được thiết kế nhằm đồng phân phối hai tác nhân chống ung thư là cisplatin và curcumin. Cụ thể, poloxamer P403 được ghép lên khung fucoidan, sau đó gắn thêm acid folic để tạo hệ nanogels hướng đích; cấu trúc vật liệu được xác nhận bằng các kỹ thuật ^{1}H-NMR, FT-IR và DLS. Hệ nanogels FA-Fud-P403 thể hiện giá trị CMC thấp và kích thước hạt nhỏ, qua đó nâng cao rõ rệt hiệu suất bao gói thuốc so với các hệ tương đương. Về đặc tính giải phóng, nanogels cho thấy cơ chế đáp ứng pH rõ rệt, với pha giải phóng nhanh ban đầu trong môi trường acid (pH 5,5), tiếp theo là quá trình giải phóng kéo dài chi phối bởi khuếch tán. Trên phương diện sinh học, thử nghiệm *in vitro* chứng minh rằng hệ FA-Fud-P403 đồng tải Cur và Cis (FA-Fud-P403@Cur/Cis) làm tăng cường độc tính trên tế bào ung thư vú MCF-7, đồng thời giảm ảnh hưởng lên tế bào bình thường HDF, cho thấy khả năng chọn lọc cao nhờ axit folic gắn lên bề mặt của hệ nanogels. Quan trọng hơn, đánh giá *in vivo* trên mô hình chuột mang khối u MCF-7 cho thấy hệ FA-Fud-P403@Cur/Cis đạt hiệu quả ức chế tăng trưởng khối u vượt trội. Kết quả này khẳng định tiềm năng của hệ nanogels hướng đích trong việc tạo ra hiệu ứng hiệp đồng mạnh mẽ, đồng thời giảm thiểu độc tính so với các liệu pháp đơn trị truyền thống

INTRODUCTION

1. The motivation: Nanogels drug delivery system - An alternative approach to conventional cancer treatment

Cancer remains one of the most challenging global health issues and continues to attract significant attention from the medical community worldwide. According to the World Health Organization, approximately 20 million new cancer cases and 10 million cancer-related deaths were reported globally. Among these, breast cancer is the most prevalent malignancy in women, accounting for approximately 31% of all diagnosed cancer cases worldwide. In Vietnam, the WHO reported 21.555 new breast cancer cases in 2020, with 9.345 deaths, placing the country among those with the highest mortality rates globally R. [1]. Conventional cancer treatment modalities, including chemotherapy, radiotherapy, and surgical resection, have significantly contributed to cancer management. Chemotherapy employs cytotoxic agents such as cisplatin, doxorubicin, paclitaxel, and trabectedin to eliminate cancer cells. Radiotherapy utilizes ionizing radiation, such as X-rays, to damage DNA and inhibit cell proliferation, while surgical resection remains the most effective approach, particularly in early-stage cancers [2]. Nevertheless, their lack of selectivity often results in severe systemic toxicity, including cardiotoxicity, immunosuppression, and damage to normal tissues. In addition, poor aqueous solubility, rapid clearance, low bioavailability, and the development of multidrug resistance further limit their clinical efficacy. These drawbacks highlight the necessity for advanced drug delivery systems capable of enhancing therapeutic outcomes while minimizing adverse effects [3]. In recent years, nanotechnology has emerged as a promising platform for cancer therapy, particularly in the development of nanoscale drug delivery systems. Nanocarriers offer unique advantages, including enhanced drug solubility, prolonged circulation time, improved pharmacokinetics, and the ability to achieve targeted drug delivery. One of the key mechanisms underlying the effectiveness of nanocarriers is the EPR effect, which allows nanoparticles to preferentially accumulate in tumor tissues due to the leaky vasculature and impaired lymphatic drainage characteristic of tumors [4]. Nanogels exhibit small particle size and favorable surface characteristics, which enhance drug transport efficiency and bioavailability. Their nanoscale dimensions allow penetration into the smallest capillaries, reduce renal clearance, prolong circulation half-life, and facilitate accumulation in pathological tissues such as solid

tumors, inflamed regions, and infected sites. Notably, tumor tissues exhibit enhanced vascular permeability, enabling nanoparticles to preferentially accumulate via the EPR effect, thereby improving drug concentration and selectivity at the tumor site. Among various nanocarrier systems, nanogels have attracted considerable attention due to their distinctive physicochemical properties that facilitate deep tumor penetration and efficient cellular uptake. Furthermore, nanogels exhibit excellent biocompatibility and biodegradability, making them highly suitable for biomedical applications [5]. Functionalization of nanocarriers with folic acid enables receptor-mediated endocytosis, thereby enhancing cellular uptake and selective drug accumulation at tumor sites. Moreover, the combination of multiple therapeutic agents within a single nanocarrier system can produce synergistic effects, leading to improved anticancer efficacy [6]. Moreover, co-delivery of multiple therapeutic agents within a single carrier system can produce synergistic effects, thereby enhancing anticancer efficacy [7].

Multifunctional nanogels, particularly those derived from amphiphilic block copolymers such as Pluronic F127 and P123, have emerged as highly promising drug delivery platforms due to their excellent biocompatibility, structural tunability, and capacity for dual drug encapsulation. Surface functionalization of these nanogels with targeting ligands further enhances their specificity and therapeutic performance. *Niu et al.* (2020) developed dual-functionalized Pluronic P105 nanogels incorporating glucose and folic acid to facilitate both blood–brain barrier (BBB) penetration and tumor targeting. The glucose moiety enabled transport via GLUT1-mediated pathways, while folic acid selectively targeted cancer cells overexpressing folate receptors. This dual-targeting approach significantly improved drug delivery efficiency, particularly in brain tumor models [8]. Mi et al. (2019) developed PEGylated gelatin nanoparticles coated with hyaluronic acid (HA) for targeted delivery of epigallocatechin gallate and low-dose doxorubicin to gastric cancer cells via CD44 receptor interaction. The combination therapy exhibited enhanced tumor growth inhibition and apoptosis compared to single-drug treatments, as confirmed by both *in vitro* and *in vivo* experiments [9]. Furthermore, Anirudhan et al. (2021) reported that HA-coated mixed micelles based on Pluronic F127/P123 for the co-delivery of paclitaxel and curcumin exhibited pronounced synergistic anticancer effects and reduced systemic toxicity, particularly in MCF-7 breast cancer cells [10]

In Vietnam, Dinh Van Thoai et al. conducted a systematic investigation into the effect of lipophilic characteristics across different poloxamer types (Pluronics P123, F127, F87, and F68), demonstrating their significant impact on self-assembly dynamics and drug encapsulation efficiency within gelatin-modified poloxamer systems [11]. Van Toan Nguyen et al. explored chitosan-based nanogels platforms incorporating similar poloxamer variants, highlighting their potential in achieving controlled and sustained release of curcumin [12]. Ngoc The Nguyen et al. engineered a thermoresponsive micellar system based on Fud-functionalized poloxamer P407, which markedly enhanced the aqueous solubility of encapsulated drugs and facilitated site-specific, controlled drug release within the tumor microenvironment. This nanocarrier platform enabled the efficient co-delivery of paclitaxel and curcumin, thereby significantly improving antitumor therapeutic outcomes while concurrently reducing systemic toxicity associated with treatment [13]. Prof. Tran Ngoc Quyen has made significant contributions to the development of pluronic-based nanogels systems grafted with various biocompatible polymers, including chitosan, heparin, gelatin, and fucoidan. These multifunctional nanogels have been effectively employed for the delivery of a wide range of chemotherapeutic agents, such as doxorubicin, paclitaxel, cisplatin, and quercetin, demonstrating promising antitumor efficacy in both *in vitro* and *in vivo* models [14]. Nguyen Dinh Trung et al. developed a thermoresponsive nanogels system based on poloxamer P403–gelatin, functionalized with folic acid as an active targeting moiety (FA-P403-Ge). This system was engineered for the co-delivery of quercetin and paclitaxel, forming a dual-drug nanoplatform (FA-GP-P403/QU/PTX). Experimental results demonstrated that this targeted system significantly enhanced the bioavailability of both drugs and exhibited markedly increased cytotoxicity against MCF-7 and HeLa cancer cell lines compared to free drug counterparts and non-targeted systems (GP-P403/QU/PTX). These findings highlight the synergistic interplay between dual-drug delivery and ligand-mediated targeting, ultimately leading to superior therapeutic performance [15]. However, previous studies have largely concentrated on formulation optimization and drug release profiles, with limited attention given to a comprehensive evaluation of targeting efficiency, selective anticancer activity in both *in vitro* and *in vivo* settings, as well as the potential for multidrug co-delivery [16]

Therefore, in this study, we synthesised the Fud-FA conjugated P403 nanogels systems co-delivery Cur/Cis, with proposing to enhance the stability, dispersibility, and biocompatibility of the nanogels system. Additionally, the incorporation of folic acid as an active targeting ligand is expected to enable site-specific drug delivery and sustained release, ultimately improving therapeutic efficacy.

2. Aim of research

This research was successful construct a nanogels system, namely FA-decorated Fud–P403 capable of co-encapsulating Cur and Cis, with the achieving synergistic modulation of pharmacokinetics, enhanced tumor-specific accumulation via active targeting, reduced systemic toxicity, and finely tuned spatiotemporal drug release, ultimately leading to a substantial improvement in anticancer efficacy against breast cancer cells

3. Scope of research

The research will focus on the synthesis, structural characterization, and comprehensive physicochemical and biological evaluation of Fud-P403 nanocarrier systems for drug delivery. The fabricated nanostructures are expected to meet essential criteria for efficient drug delivery materials, including: (i) the ability to exist as a solution at low temperatures and undergo self-assembly into nanostructures in response to changes in temperature and concentration; (ii) an appropriate nanoscale size (100–200 nm) with good colloidal stability and dispersion; (iii) a significant improvement in the solubility of chemotherapeutic agents; (iv) high drug encapsulation efficiency; (v) excellent stability during storage and circulation in the bloodstream; (vi) tunable and sustained drug release profiles; and (vii) minimal cytotoxicity toward normal cells. Subsequently, nanocarrier systemswill be further functionalized with active targeting ligands, such as folic acid, to enable receptor-mediated targeting. This modification is expected to enhance selective uptake by cancer cells while minimizing off-target toxicity through specific interactions with overexpressed receptors in the tumor microenvironment.

The anticancer efficacy of the FA-Fud-P403 will be initially evaluated *in vitro* using the MCF-7 breast cancer cell line, with particular emphasis on cellular uptake, cytotoxicity, and targeting efficiency. In addition, the underlying mechanisms of tumor targeting and cell death induction will be systematically investigated and compared with those of conventional chemotherapy. Furthermore, *in vivo* studies will be

conducted using appropriate tumor-bearing animal models to assess therapeutic efficacy, biodistribution, pharmacokinetics, and systemic safety. Special attention will be given to tumor accumulation via both passive and active targeting mechanisms, as well as the circulation stability of the nanocarrier system. Importantly, the synergistic therapeutic potential of the co-delivered drugs, Cis and Cur, will be comprehensively evaluated in both *in vitro* and *in vivo* models. This combination is anticipated to enhance anticancer efficacy through complementary mechanisms, including increased apoptosis induction, inhibition of tumor proliferation, and modulation of oxidative stress within the tumor microenvironment. Comparative studies with single-drug treatments and conventional chemotherapy will be performed to quantitatively assess tumor growth inhibition, therapeutic synergy, thereby providing a promising strategy for effective and safe breast cancer treatment.

4. Theoretical basis and practical significant of research

Building upon previously reported poloxamer-based nanogels drug delivery systems, it is evident that pluronic copolymers conjugated with various polysaccharides and functionalized with targeting ligands exhibit significant potential for the encapsulation of hydrophobic anticancer agents. These hybrid systems demonstrate enhanced biocompatibility and high drug-loading efficiency, thereby improving drug dispersion while reducing systemic toxicity, ultimately leading to increased bioavailability and improved anticancer efficacy. Furthermore, the surface of poloxamer micelles can be readily functionalized with biologically active targeting moieties (e.g., peptides, PEG, hyaluronic acid, biotin, or folic acid), enabling selective recognition of overexpressed receptors on cancer cell membranes. This active targeting capability significantly enhances cellular uptake and therapeutic efficiency against cancer cells. Therefore, the scientific basis of this study is founded on the development of nanogels drug delivery systems, particularly nanogels derived from amphiphilic block copolymers. Moreover, the co-delivery of multiple anticancer agents within a single nanocarrier system has been recognized as an effective strategy to achieve synergistic therapeutic effects.

5. Contribution of research

- Successfully developed a biocompatible nanogels based on FA–Fud conjugated to P403, capable of co-delivering curcumin and cisplatin for selective anticancer by folate-mediated tumor targeting

- Successful co-encapsulation Cis/Cur into FA-Fud-P403 based on the hydrophobic and electrostatic interaction between anticancer drug with the FA-Fud-P403 nanogels that achieved high dual-drug encapsulation with nanogels core

- The *in vitro* studies exhibited higher cytotoxicity toward breast cancer cell line compared to normal cells, attributing to the enhanced selectivity to cancer cells of targeted nanogels.

-The both *in vitro* and *in vivo* studies highlighted the potential synergistic therapeutic efficacy and minimized adverse side effect of dual-drug nanogels into MCF-7 cell line and MCF-7 tumor-bearing mice associated with conventional chemotherapy that confirmed the superior tumor inhibition with FA-Fud-P403@Cur/Cis.

CHAPTER 1. LITERATURE REVIEW

1.1. Overview of cancer disease and the challenges into chemotherapy treatment

Cancer is a major global health challenge and remains one of the leading causes of morbidity and mortality worldwide, placing a substantial burden on healthcare systems. Among the most commonly diagnosed cancers are breast, lung, colorectal, and prostate cancers, while lung cancer remains the leading cause of cancer-related mortality worldwide [17]. According to GLOBOCAN 2022 data, the country recorded approximately 180.000 new cancer cases and over 120.000 cancer-related deaths annually, with a five-year prevalence exceeding 400.000 cases [18]. The most common cancers include breast, liver, lung, colorectal, and stomach cancers, reflecting both infection-related and lifestyle-associated disease patterns. Notably, Vietnam is among the countries with relatively high cancer mortality rates, largely due to late-stage diagnosis and limited early screening programs [19]. The increasing incidence of cancer strongly associated with modifiable risk factors, including tobacco use, alcohol consumption, unhealthy diets, obesity, physical inactivity, and environmental pollution [20]. Cancer is characterized by uncontrolled cell proliferation, tissue invasion, and the ability to metastasize through the bloodstream or lymphatic system [21]. Unlike normal cells, cancer cells evade regulatory mechanisms controlling the cell cycle and apoptosis, leading to the accumulation of abnormal cells and the formation of malignant tumors [22]. Currently, anticancer approches primarily include surgery, radiotherapy, and chemotherapy [23]. While surgery is effective for early-stage localized tumors and radiotherapy can inhibit tumor growth through DNA damage, both approaches have limitations, particularly in advanced or metastatic disease [24]. Chemotherapy remains a cornerstone of systemic treatment; however, its clinical efficacy is significantly hindered by several drawbacks. Most notably, chemotherapeutic agents lack selectivity, leading to damage of normal rapidly dividing cells and causing severe side effects such as myelosuppression, gastrointestinal toxicity, and immunosuppression [25]. Additionally, the narrow therapeutic index of these drugs often necessitates suboptimal dosing to minimize toxicity, which may compromise treatment outcomes. Furthermore, the tumor microenvironment presents significant barriers to effective drug delivery, including

abnormal vasculature, high interstitial pressure, and hypoxia, resulting in uneven drug distribution and therapeutic resistance [26]

1.2. Overview about anticancer drugs

1.2.1. Cisplatin (Cis)

1.2.1.1. Structural and physicochemical characterizations of Cis

Cis (cis-diamminedichloroplatinum (II)) is commonly used as first-line chemotherapeutic drug in the treatment of human cancers, approved by FDA in 1987 [27]. Although the compound was first synthesized by M. Peyrone in 1844, its pharmacological potential remained undiscovered until 1965, when Barnett Rosenberg's seminal research at Michigan State University revealed its ability to inhibit cell division [28]. Clinically, Cis has demonstrated pronounced efficacy against ovarian and testicular cancers, as well as head and neck cancers, and has been evaluated across multiple solid tumors, including sarcomas and cancers of soft tissue, bone, muscle, and vascular origin

Structurally, Cis is a square-planar Pt(II) coordination compound in which two chloride ligands and two ammine ligands adopt a Cis geometry, a configuration that is critical for its cytotoxic activity **(Figure 1.1)**. It exhibits poor aqueous solubility but dissolves readily in polar aprotic solvents, including DMSO and DMF. Cis displays good physicochemical stability under standard conditions, although gradual isomerization to the pharmacologically inactive trans form may occur upon prolonged storage. Key physicochemical parameters include a molecular weight of 301.1 g/mol, a density of 3.74 g/cm³, a melting point near 270 °C, a low octanol–water partition coefficient ($\log K_{o}w = -2.19$), and a water solubility of approximately 2.53 g/L at 25 °C, underscoring its predominantly hydrophilic character.

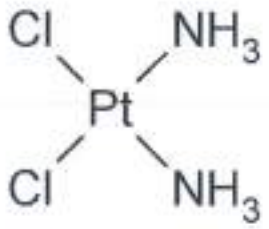

Figure 1.1. The chemical structure of Cis

Despite its remarkable clinical efficacy, the therapeutic application of Cis is severely constrained by significant dose-limiting toxicities, such as nephrotoxicity,

neurotoxicity, and ototoxicity, as well as the frequent emergence of acquired drug resistance [29].

1.2.1.2. Biological activity of Cis

Cis has played an important role in cancer chemotherapy. Its anticancer activity is primarily associated with its interaction with cellular DNA, resulting in inhibition of DNA synthesis, suppression of RNA transcription, disruption of cell cycle progression, and causing to apoptosis [30]. A key factor influencing the biological activity of Cis is the difference in chloride ion concentration between the extracellular and intracellular environments. In extracellular fluids or blood plasma, the chloride ion concentration is relatively high (approximately 90–100 mM), whereas the intracellular chloride concentration is markedly lower (around 4–10 mM). The high chloride concentration in the bloodstream stabilizes Cis in its neutral dichloro form, thereby limiting premature activation and nonspecific reactions **(Figure 1.2).**

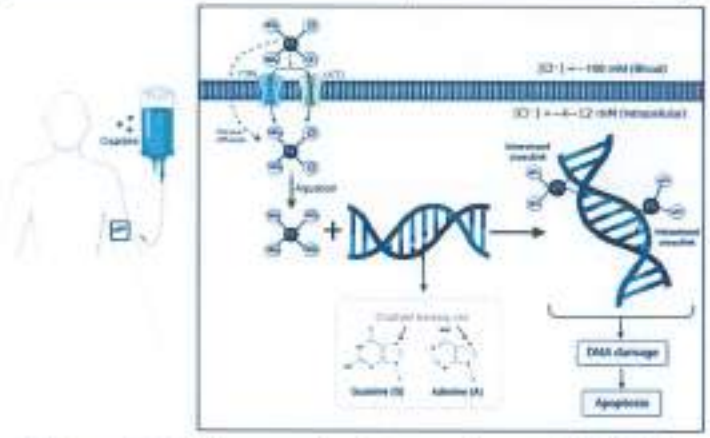

Figure 1.2. The mechanism action of Cis [31]

Upon entering the intracellular environment, Cis undergoes hydrolysis, during which one or both chloride ligands are replaced by water molecules, forming mono-aqua or di-aqua platinum complexes [29]. Specifically, Cis preferentially binds to guanine residues, which are purine nucleobases present in both DNA and RNA. The N7 position of guanine serves as the primary coordination site for platinum binding, leading to the formation of Pt–DNA adducts that distort the DNA double helix and interfere with DNA replication and transcription processes. Among these adducts, 1,2-intrastrand crosslinks, particularly d(GpG) and d(ApG), are the most abundant and biologically relevant, whereas 1,3-intrastrand and interstrand crosslinks occur less frequently. These DNA lesions hinder the progression of DNA polymerases, activate DNA damage recognition pathways, and induce cell cycle arrest, especially during the

S and G2/M phases. When the extent of DNA damage exceeds the repair capacity of the cell, apoptotic cell death may occur **(Figure 1.3)**.

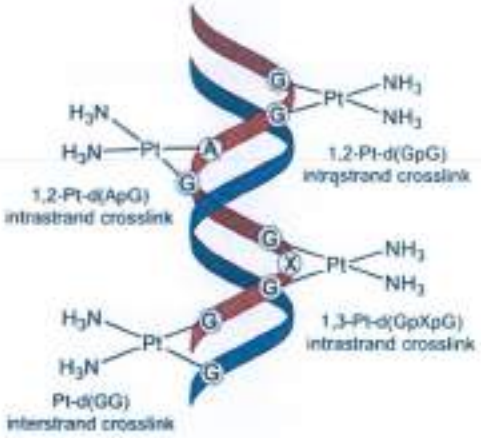

Figure 1.3. The schematic illustration of platinum–DNA interactions showing interstrand crosslinks formed by platinum-based anticancer drugs [32]

Furthermore, Cis-induced ROS generation may exceed the oxidative tolerance threshold of cancer cells, contributing to its cytotoxic effects. In the intracellular environment, the hydrolyzed forms of Cis have been reported to exhibit increased reactivity and may interact with mitochondrial components that can induce the release of Ca^{2+} from the mitochondrial matrix, leading to transient elevations in cytosolic Ca^{2+} levels [33]. This disturbance of calcium homeostasis promotes mitochondrial depolarization, increases mitochondrial membrane permeability, and further exacerbates mitochondrial dysfunction. Cis-induced mitochondrial impairment is associated with inhibition of mitochondrial respiratory function, depletion of ATP, and dysregulation of mitochondrial signaling pathways [34]. In addition, loss of mitochondrial membrane integrity facilitates the release of pro-apoptotic factors, which contributes to the activation of the intrinsic apoptotic pathway.

1.2.1.3. Cytotoxicity of Cis

While these mechanisms underlie the anticancer efficacy of Cis, they also account for its toxicity toward normal tissues. Because Cis lacks strict selectivity for cancer cells, its interaction with DNA and mitochondria in healthy cells can result in a range of adverse effects [35]. Clinically, Cis treatment is associated with nausea and vomiting, nephrotoxicity, cardiotoxicity, hepatotoxicity, and neurotoxicity **(Figure 1.4)**.

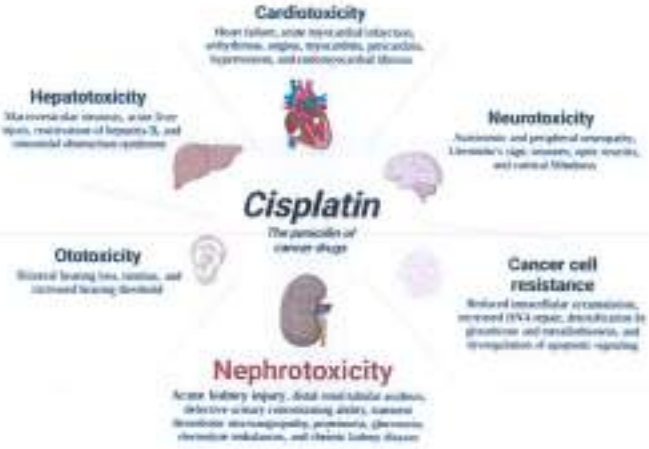

Figure 1.4. The side effects associated with Cis administration [31]

Nephrotoxicity is another major dose-limiting toxicity of Cis. The kidneys serve as the primary route of Cis excretion and tend to accumulate Cis at higher levels than other organs, including the liver that are likely by enhancing renal clearance and decreasing renal drug accumulation [36]. The peripheral sensory nervous system is most commonly affected, with clinical manifestations including peripheral sensory neuropathy, hearing loss, seizures, and Lhermitte's sign, particularly in patients receiving high-dose Cis therapy [37]. Taken together, the therapeutic efficacy and dose-limiting toxicities of Cis arise from the same fundamental mechanisms involving DNA damage, mitochondrial dysfunction, oxidative stress, and calcium imbalance. Understanding these mechanisms provides a critical basis for the development of strategies aimed at enhancing antitumor efficacy while minimizing systemic toxicity.

Cis resistance arises from a complex network of cellular adaptations that collectively reduce intracellular drug availability, attenuate DNA damage signaling, and suppress apoptosis [38]. These mechanisms include decreased drug accumulation, enhanced DNA repair capacity, intracellular drug inactivation, and increased drug efflux. Among these mechanisms, reduced intracellular accumulation of Cis is considered a central determinant of resistance **(Figure 1.5)**. Cellular uptake of Cis is largely mediated by the copper transporter 1 (CTR1). Genetic alterations, downregulation, or functional impairment of CTR1 significantly diminish Cis influx into tumor cells [39]. Notably, CTR1 exhibits a high affinity for copper ions (Cu^+), which compete directly with Cis for transport. Consequently, increased copper binding or copper availability reduces Cis uptake and lowers intracellular platinum concentrations. In addition, tumor cells may develop resistance mechanism through

enhanced DNA repair process, which counteract Cis-induced DNA lesions and weaken the DNA damage response [40]. Another major contributor to Cis resistance is the intracellular inactivation of Cis which are subsequently expelled from the cell via MRPs. Studies in ovarian cancer cell lines have demonstrated that elevated GSH levels strongly correlate with increased Cis inactivation and resistance **(Figure 1.5)**. In addition, enhanced drug efflux mechanisms further reduce intracellular Cis concentrations and reinforce resistance. The ATP-binding cassette transporters ATP7A and ATP7B are actively involved in exporting platinum-based drugs from cancer cells [41].

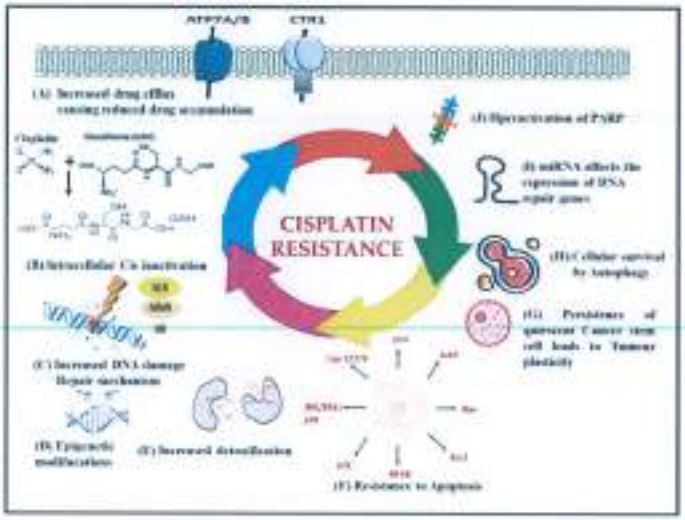

Figure 1.5.The mechanism of Cis-resistance [42]

1.2.2. Curcumin (Cur)

1.2.2.1. Structural and physicochemical characterizations of Cur

Cur is a naturally occurring hydrophobic polyphenolic compound isolated from the rhizome of Curcuma longa (turmeric). It is the principal bioactive constituent of turmeric and belongs to the diarylheptanoid family of natural compounds, which are characterized by two aromatic rings connected by a seven-carbon linker.

The IUPAC name: (1E,6E)-1,7-bis(4-hydroxy-3-methoxyphenyl)hepta-1,6-diene-3,5-dione

Molecular formular: $C_{21}H_{20}O_6$ with molecular weight of approximately 368.38 g/mol

Structurally, Cur contains two substituted phenyl rings bearing phenolic hydroxyl (–OH) and methoxy ($–OCH_3$) groups, linked by a conjugated heptadienedione chain that incorporates an α,β-unsaturated β-diketone moiety **(Figure 1.6)**. The molecule contains several important functional groups, including phenolic

hydroxyl groups, methoxy and a β-diketone structure that contribute significantly to its physicochemical behavior, such [82-83].

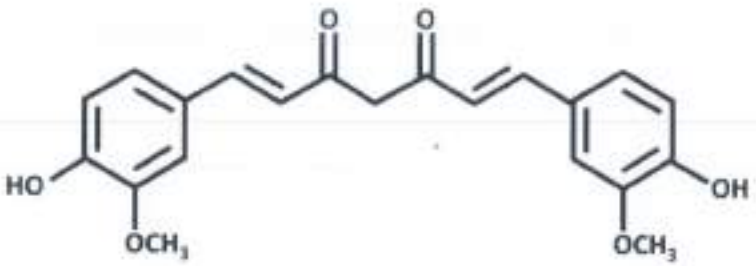

Figure 1.6. The chemical structure of Cur [45]

In addition, Cur exhibits poor aqueous solubility and dissolves more readily in organic solvents such as ethanol, methanol, acetone, and dimethyl sulfoxide that is mainly attributed to its extensive aromatic conjugated structure and the limited number of ionizable functional groups, leading to the limitations of pharmaceutical applications [46]. Additionally, Cur demonstrates pH-dependent chemical stability, remaining relatively stable under acidic to neutral conditions but undergoing rapid degradation in alkaline environments through hydrolytic and oxidative processes [47]. Furthermore, the structural features of Cur, particularly the phenolic hydroxyl groups and the β-diketone moiety, enable the molecule to participate in hydrogen atom donation, radical scavenging, and metal ion chelation.

1.2.2.2. Biological activity of Cur

Cur has attracted considerable attention in biomedical and pharmaceutical research due to its broad spectrum of biological activities. Extensive studies have demonstrated that Cur exhibits a wide range of pharmacological effects, including antioxidant, anti-inflammatory, antimicrobial, wound-healing, and anticancer properties [48]. These biological activities are largely attributed to the unique chemical structure of Cur, which consists of two aromatic phenolic rings linked that enables Cur to participate in redox reactions and interact with numerous biomolecules such as proteins, enzymes, transcription factors, and signaling molecules **(Figure 1.7)**. Through these interactions, Cur is able to modulate multiple intracellular signaling pathways involved in oxidative stress, inflammation, cell proliferation, apoptosis, and tumor progression [49].

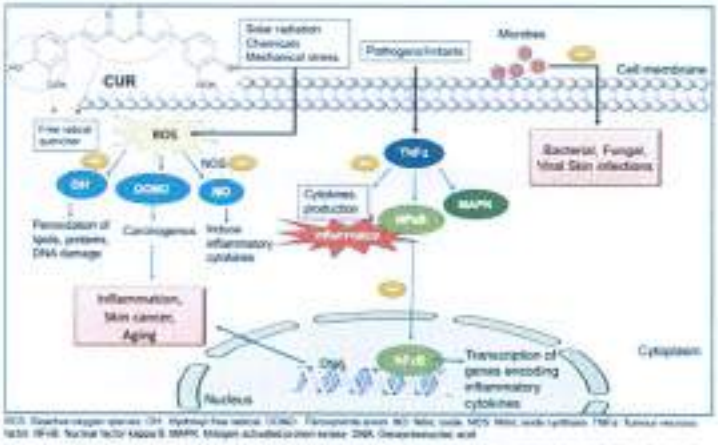

Figure 1.7.The mechanism of Cur action [50]

One of the most extensively studied biological functions of Cur is its potent antioxidant activity, which plays a crucial role in protecting cells from oxidative stress [48]. This radical-scavenging ability occurs through hydrogen atom transfer and single-electron transfer mechanisms, allowing Cur to neutralize reactive molecules and interrupt the chain reactions of lipid peroxidation. Consequently, Cur prevents oxidative degradation of membrane lipids and protects cellular structures from oxidative damage. Cur suppresses inflammatory processes primarily by inhibiting the activation of nuclear factor kappa B (NF-κB), a key transcription factor responsible for regulating the expression of genes encoding proinflammatory cytokines, chemokines, and adhesion molecules[51]. By blocking the nuclear translocation and activation of NF-κB, Cur downregulates the transcription of inflammatory mediators such as tumor necrosis factor-alpha (TNF-α), interleukin-1β (IL-1β), interleukin-6 (IL-6), and cyclooxygenase-2 (COX-2) [52]. Moreover, Cur can regulate the expression of growth factors and cytokines involved in tissue repair and regeneration. By reducing oxidative stress and suppressing excessive inflammatory responses at the wound site, Cur creates a favorable microenvironment that facilitates tissue regeneration and improves wound healing outcomes [53].

Among its diverse pharmacological properties, the anticancer activity of Cur has been the most extensively investigated. Cur has been shown to interfere with multiple stages of cancer development, including tumor initiation, promotion, and progression. Cur modulates the expression and activity of numerous oncogenes and tumor suppressor genes involved in cell proliferation, apoptosis, angiogenesis, and metastasis. Cur has been reported to downregulate the expression of the human epidermal growth factor receptor 2 (HER2) gene, which is frequently overexpressed

in several aggressive types of cancer [54]. By suppressing HER2 expression, Cur inhibits tumor cell proliferation and reduces oncogenic signaling associated with tumor growth, promoting tumor growth and resistance to apoptosis [55]. Cur induces cell cycle arrest primarily at the G1 phase by downregulating the expression of Cyclin D1 and inhibiting cyclin-dependent kinases responsible for the transition from the G1 phase to the S phase that prevents uncontrolled cell division and suppresses tumor cell proliferation and cell division [56]. Furthermore, Cur plays a significant role in inhibiting tumor invasion and metastasis by suppressesing epithelial–mesenchymal transition (EMT) by regulating transcription factors which are responsible for the loss of epithelial characteristics and the acquisition of mesenchymal phenotypes in cancer cells. By inhibiting these transcription factors, Cur prevents cancer cells from gaining migratory and invasive properties [57]. In addition, Cur reduces the expression of adhesion molecules such as vascular cell adhesion molecule-1 (VCAM-1) and matrix metalloproteinases, thereby limiting the interaction between cancer cells and vascular endothelial cells and reducing metastatic dissemination [58].

1.2.2.3. Research trends on the synergistic potential of combinatorial chemotherapeutic drugs and bioactive phytochemicals for cancer treatment

Despite significant role in cancer therapy, conventional chemotherapeutic agents such as Cis, methotrexate, 5-fluorouracil (5-FU), doxorubicin, and paclitaxel are frequently associated with severe systemic toxicity, limited tumor selectivity, and the rapid emergence of drug resistance due to high-dose and long-term treatment regimens, which further exacerbate adverse effects and compromise patients' quality of life [59]. To overcome these limitations, combinatorial therapeutic strategies integrating chemotherapeutic drugs with bioactive phytochemicals have gained increasing attention. Plant-derived compounds such as polyphenols, flavonoids, and other secondary metabolites are abundant in nature and exhibit diverse biological activities, including antioxidants, anti-inflammatory, immunomodulatory, and anticancer effects. Accumulating evidence indicates that the phytochemicals can synergize with conventional chemotherapeutic agents to enhance antitumor efficacy and simultaneously alleviating chemotherapy-induced cytotoxicity [60]. The synergistic anticancer effects of phytochemicals arise from their ability to modulate multiple signaling pathways involved in tumor progression and treatment resistance.

In addition to suppressing tumor cell proliferation and inducing apoptosis, these compounds regulate redox balance, attenuate chronic inflammation, modulate immune responses, and interfere with oncogenic signaling cascades such as NF-κB, STAT3, Wnt/β-catenin, and PI3K/Akt [61]. Thus, the advantage of phytochemical–chemotherapy combinations are their capacity to mitigate the severe adverse effects commonly attributing to anticancer drugs. Natural bioactive compounds have been shown to improve the tolerability of conventional chemotherapeutic agents, reduce off-target toxicity, and protect normal tissues, thereby enabling dose reduction without compromising antitumor outcomes[62]. Notably, Cur also suppressed EMT by reducing the expression of polycomb repressive complex components such as BMI1, SUZ12, and EZH2, thereby limiting tumor invasion and metastasis [63]. Furthermore, Parveen Kumar *et al.* reported that co-administration of Cur with Cis markedly reduced Cis-induced nephrotoxicity while improving its pharmacokinetic profile, ultimately contributing to enhanced antitumor efficacy [64]. Recently, Abadi, Asal Jalal, *et al.* further demonstrated that Cur not only attenuates Cis-induced toxicity in multiple organs but also significantly potentiates its anticancer activity by activating apoptotic pathways, inhibiting STAT3 and NF-κB signaling, and suppressing EMT. These combined effects rendered cancer cells more susceptible to Cis and underscored the potential of Cur as a chemosensitizing agent [65]. Li *et al.* reported that quercetin effectively suppressed invasion and reversed Cis resistance in nasopharyngeal carcinoma cells by modulating the Hippo/Yes-associated protein (YAP) signaling pathway. Quercetin-induced YAP phosphorylation prevented its nuclear translocation and subsequent activation of genes associated with proliferation and survival, leading to reduced tumor growth, enhanced apoptosis, and limited metastatic potential [66].

Phytochemical compounds such as Cur and quercetin suffer from extremely low aqueous solubility, poor chemical stability under physiological conditions, rapid metabolism, and limited systemic bioavailability [67,68]. Furthermore, the nonspecific biodistribution of both chemotherapeutic agents and phytochemicals often results in insufficient drug accumulation at tumor sites while increasing off-target toxicity in healthy tissues [67]. In recent years, nanotechnology-based drug delivery systems have emerged as a rational and powerful solution to overcome these limitations. Nanocarriers such as polymeric micelles, nanogels, nanoparticles, liposomes, and hybrid nanostructures offer unique advantages, including improved

solubilization of hydrophobic phytochemicals, protection against premature degradation, prolonged circulation time, and enhanced tumor accumulation via the EPR effect **(Figure 1.8)** [69]. Importantly, nanocarrier systems enable the co-encapsulation to co-delivery of chemotherapeutic drugs and phytochemicals at controlled drug-released acceleration, thereby preserving synergistic interactions and ensuring pharmacokinetics at the tumor site.

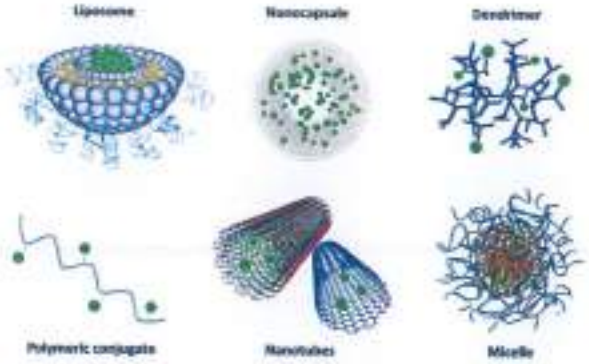

Figure 1.8. The illustration of various nanocarrier platforms for drug delivery, including liposomes, nanocapsules, dendrimers, polymeric conjugates, nanotubes, and micelles

Among various nanocarrier platforms, polymeric micelles have attracted particular interest due to their high drug-loading capacity, tunable physicochemical properties, and stimuli-responsive behavior. Amphiphilic copolymers, such as pluronic-based systems, can self-assemble into core–shell micellar structures that effectively encapsulate hydrophobic within the core while maintaining colloidal stability in aqueous environments. Furthermore, the incorporation of stimuli-responsive elements (e.g., pH-, redox-, or enzyme-sensitive linkages) enables site-specific drug release in the acidic and enzyme-rich tumor microenvironment, thereby enhancing therapeutic efficacy and minimizing systemic toxicity [70,71]. Additionally, surface functionalization of nanocarriers with targeting ligands, such as folic acid, peptides, or antibodies, further improves cellular uptake through receptor-mediated endocytosis and enhances tumor selectivity. By integrating active targeting, controlled release, and combination therapy within a single nanosystem, phytochemical-loaded nanocarriers represent an advanced and versatile platform for next-generation cancer treatment [72]. These approaches not only maximize antitumor efficacy and overcome chemoresistance but also significantly reduce systemic

toxicity, thereby offering a promising pathway toward safer, more effective, and clinically translatable cancer therapies.

1.3. Nanogels drug delivery systems – an alternative approach to traditional cancer treatment

1.3.1. Overviews of nanogels drug delivery system

The combination of chemotherapeutic agents with bioactive natural compounds has emerged as an effective strategy to enhance anticancer efficacy while alleviating treatment-associated toxicity. However, aqueous insolubility, low chemical stability, rapid metabolism, and reduced bioavailability are among the principal challenges that compromise drug absorption, resulting in insufficient drug concentrations at the target site, thereby increases the risk of systemic toxicity and adverse effects. To address these challenges, substantial research efforts have been directed toward the development of advanced drug delivery systems capable of improving drug solubility, stability, and bioavailability. Nanotechnology-based drug delivery platforms—including liposomes, polymeric micelles, dendrimers, nanoemulsions, and nanogels—have attracted considerable attention due to their ability to modulate pharmacokinetic behavior and biodistribution profiles of therapeutic agents [73,74]. By encapsulating drugs within nanoscale carriers, these systems can protect active compounds from premature degradation, enhance circulation time, improve accumulation at pathological sites, and reduce nonspecific distribution to healthy tissues, contributing to improved therapeutic outcomes and reduced off-target toxicity.

Among various nanocarrier systems, nanogels have emerged as particularly promising candidates for systemic drug delivery applications. Nanogels are nanosized hydrogel particles, typically ranging from 20 to 200 nm in diameter, composed of three-dimensional polymer networks formed through physical or chemical crosslinking [75,76]. Common polymeric building blocks include amphiphilic copolymers and triblock copolymers, which can undergo spontaneous self-assembly into nanogels structures, as well as polymers bearing reactive functional groups that enable direct chemical crosslinking **(Figure 1.9)**. These design strategies allow nanogels to encapsulate a broad spectrum of therapeutic payloads, including small-molecule drugs, nucleic acids, peptides, and proteins. A defining feature of nanogels is their exceptionally high-water content and pronounced swelling behavior in

aqueous and biological environments [77,78]. Upon exposure to water or physiological fluids, nanogels absorb substantial amounts of liquid and swell without dissolving, thereby maintaining their structural integrity. This swelling behavior not only facilitates efficient drug loading but also enables nanogels to function as stable reservoirs for sustained and controlled drug release [79]. The highly hydrated polymeric shell of nanogels plays a crucial role in enhancing their biological performance. The hydrophilic corona effectively minimizes nonspecific interactions with serum proteins, thereby reducing protein adsorption and subsequent opsonization by the mononuclear phagocyte system [80]. As a result, nanogels exhibit prolonged circulation time in the bloodstream, improved colloidal stability, and enhanced drug retention during systemic transport. Moreover, the internal polymer network can accommodate both hydrophilic and hydrophobic drugs, protecting them from chemical degradation and enzymatic hydrolysis during storage and circulation [81].

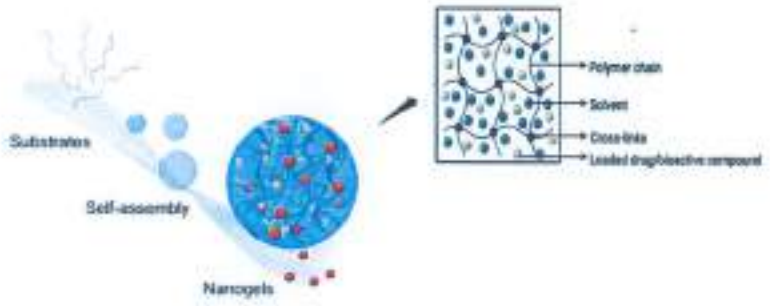

Figure 1.9. The schematic representation of self-assembly nanogels matrix

Recently, nanogels can be engineered to exhibit responsiveness to specific internal stimuli present in the biological environment, such as changes in pH, temperature, redox potential, enzyme activity, or ionic strength [82,83]. External stimuli, including light, ultrasound, or magnetic fields, can also be exploited to trigger drug release in a spatially and temporally controlled manner. Stimuli-responsive nanogels undergo reversible structural or conformational changes upon exposure to these triggers, most commonly swelling or deswelling of the polymer network. These changes alter the permeability of the nanogels matrix and regulate the diffusion of encapsulated drugs, enabling controlled and site-specific drug release [84]. Therefore, nanogels-based drug delivery systems combine high drug-loading capacity, excellent biocompatibility, tunable physicochemical properties, and stimuli-responsive behavior within a single platform. These attributes position nanogels as highly promising carriers for the efficient delivery of chemotherapeutic agents and bioactive

natural compounds, thereby enhanced efficacy, reduced systemic toxicity, and improved clinical treatment.

1.3.2. Characterizations of thermoresponsive nanogels drug delivery system

Thermoresponsive nanogels represent a stimuli-responsive nanosystems engineered to reversibly modulate their physicochemical properties that are adaptive capability for regulation of drug encapsulation, nanosystem stability, and release kinetics. In aqueous, the phase behavior of these systems is typically defined by LCST and, occasionally, an UCST. For biomedical applications, particularly injectable drug delivery, the ideal LCST is generally designed to fall within the physiological to mildly hyperthermic range (37 °C–42 °C) [85]. Within this thermal window, nanogels maintain a hydrated, stable state under normal physiological conditions but undergo controlled structural transitions upon localized heating, such as that found in tumor microenvironments or induced by external hyperthermia [86].

However, a significant limitation of many conventional thermosensitive copolymers is that their intrinsic LCST lies below physiological temperature which triggers premature phase separation immediately following intravenous administration, leading to aggregation, and reduced bioavailability. To overcome these limitations, modern strategies focus on chemical modifications of the polymer backbone to elevate the LCST and enhance systemic stability **(Figure 1.10).**

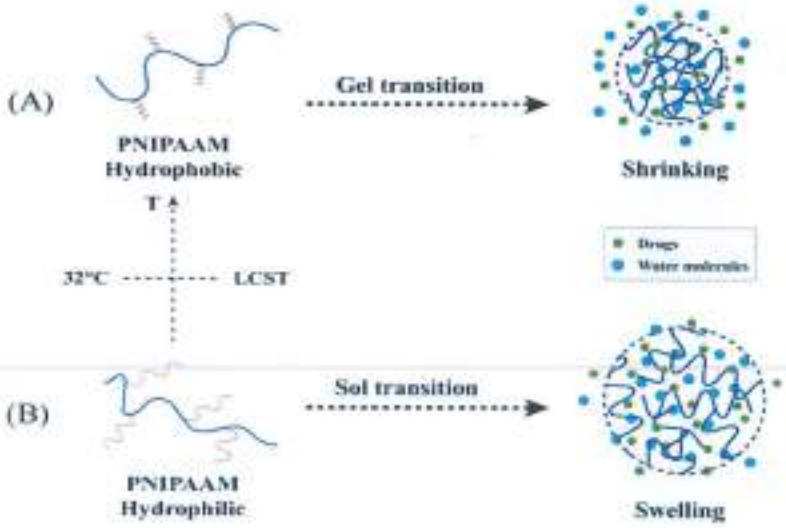

***Figure 1.10. The thermoresponsive behavior of nanogels structure** [87]*

Poly(N-isopropylacrylamide) (PNIPAM) is widely regarded as the gold standard, exhibiting a sharp, reversible coil–globule transition at an LCST of approximately 32 °C. Below this threshold, hydrogen bonding between amide groups

and water molecules maintains the polymer chains in a hydrated, expanded conformation. When the temperature exceeds the LCST, the disruption of these bonds and the dominance of hydrophobic interactions among isopropyl groups trigger abrupt nanogels shrinkage [88]. Poloxamer copolymers consist of amphiphilic PEO–PPO–PEO triblock structures that exist as unimers in solution at low temperatures. As temperature rises, the PPO blocks progressively dehydrate, driving self-assembly into micelles featuring a hydrophobic core and a hydrophilic PEO corona, leading to nanogels shrinkage or a sol–gel transition [89]. Importantly, the hydrophilic PEO shell provides essential steric stabilization, minimizing nonspecific protein adsorption and prolonging systemic circulation [90].

1.3.3. Nanogel-based systems for targeted drug delivery for anticancer treatment

Nanogels-based drug delivery systems have emerged as highly promising platforms for anticancer therapy owing to their nanoscale dimensions, three-dimensional crosslinked polymeric networks, and exceptional capacity for physicochemical and biological customization. Nanogels offer substantial advantages in improving the solubility and bioavailability of poorly water-soluble drugs, prolonging systemic circulation time, and reducing nonspecific toxicity [75,91].

1.3.3.1. Passive targeting via the EPR effect

Passive targeting constitutes a fundamental mechanism governing the preferential accumulation of nanogels-based systems in solid tumors relied on the EPR effect, which originates from the abnormal vascular architecture and impaired lymphatic drainage characteristic of tumor tissues **(Figure 1.11)**. Rapid and uncontrolled tumor angiogenesis results in the formation of structurally defective blood vessels with enlarged inter-endothelial gaps, typically ranging from approximately 400 to 800 nm, thereby permitting nanoscale drug carriers to extravasate selectively into the tumor interstitium [92]. Nanogels engineered within an appropriate size window can effectively exploit the EPR effect to achieve preferential tumor accumulation. In addition, the absence or dysfunction of lymphatic drainage in tumor tissues limits the clearance of macromolecules and nanoparticles, leading to prolonged retention of nanogels within the tumor microenvironment that increases the local concentration of anticancer drugs at the tumor site, thereby

enhancing therapeutic efficacy while reducing systemic exposure and dose-limiting toxicities such as cardiotoxicity, nephrotoxicity, and myelosuppression.

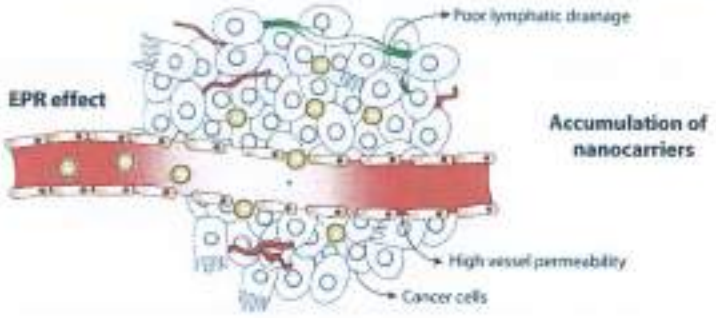

Figure 1.11.The passive-tumor targeting of nanocarriers by EPR effect

The hydrophilic corona of amphiphilic copolymers-based nanogels further contributes to prolonged blood circulation, increasing the likelihood of repeated vascular passaging and subsequent tumor extravasation [93]. However, despite its central role in nanomedicine, EPR-mediated passive targeting alone is often insufficient to ensure uniform and effective drug delivery. The magnitude of the EPR effect is highly heterogeneous and depends on multiple factors, including tumor type, tumor size, vascular density, interstitial fluid pressure, and stromal composition [94]. As a result, passive targeting frequently leads to uneven intratumoral drug distribution, with limited penetration into poorly vascularized or hypoxic tumor regions. These limitations highlight the need for additional targeting mechanisms to improve delivery efficiency at the cellular level.

1.3.3.2. Active targeting strategies and receptor-mediated cellular uptake

To overcome the intrinsic shortcomings of passive targeting, active targeting strategies have been developed to enhance the specificity and efficiency of nanogels-based drug delivery systems through surface functionalization of nanogels with ligands capable of selectively recognizing and binding to receptors overexpressed on the surface of cancer cells while exhibiting minimal expression in normal tissues. Upon ligand-receptor recognition, the nanogels are internalized via receptor-mediated endocytosis, effectively by passing the MDR efflux pumps that often compromise the efficacy of free chemotherapeutics [95]. Active targeting not only enhances intracellular drug delivery but also minimizes nonspecific accumulation in healthy tissues, leading to improved therapeutic efficacy and reduced systemic toxicity. Beyond reaching the target site, the ultimate performance of a nanogels is dictated by its ability to release the drug in response to specific physiological triggers. Commonly

targeted receptors include folate receptors, integrins (e.g., αvβ3), transferrin receptors, epidermal growth factor receptors, and HER2 [96] **(Figure 1.12)**.

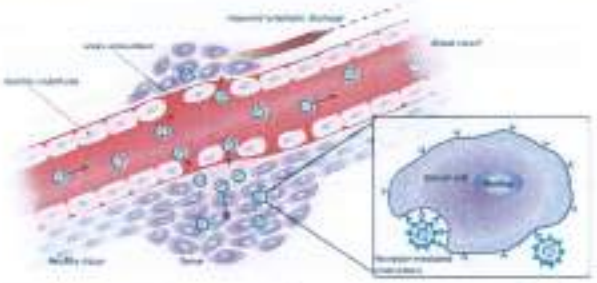

Figure 1.12. The active -tumor targeting of nanocarriers by specific ligands

Ligands such as folic acid, RGD peptides, antibodies, aptamers, and other small molecules are conjugated to the nanogels surface via covalent or noncovalent interactions. In practical terms, nanogels must first reach and accumulate within the tumor microenvironment through EPR-mediated passive targeting before ligand–receptor interactions can exert their effects at the cellular level [97]. Nanogels are increasingly designed as stimuli-responsive systems that remain stable under physiological conditions (pH 7.4) but undergo rapid structural transitions within the tumor microenvironment. These triggers often include the acidic pH of endosomal compartments (pH 5.0–6.0), which are cleavage of pH-sensitive or redox-responsive crosslinks within the nanogels network, enabling site-specific and efficient intracellular drug release [72]. The integration of EPR-mediated accumulation, ligand-driven cellular uptake, and stimuli-responsive drug release provides a synergistic framework for maximizing antitumor efficacy while minimizing off-target toxicity

1.4. Overview of P403

1.4.1. Chemical structure of P403

P430 polymers are amphiphilic triblock copolymers widely utilized in pharmaceutical and biomedical applications due to their remarkable biocompatibility and thermoresponsive behavior that have been approved for medical use by the FDA for human use, which has further promoted their extensive investigation as drug delivery materials. Chemically, P403 (pluronic P123) has attracted considerable attention in nanomedicine research. This copolymers typically contains approximately 20 ethylene oxide units in each hydrophilic block and around 70 propylene oxide units in the hydrophobic segment as thermosensitive part [98]. Additonally, the ratio PEO/PPO of P403 are relative to HLB value about 8 that affect to particle size, drug encapsulation and stability of P403 polymer polymer [99] **(Figure 1.13)**.

Figure 1.13.The chemical structure of P403

1.4.2. Characterization of P403

P403 has received increasing attention as a functional material in nanomedicine. Due to its relatively high hydrophilic–lipophilic balance compared with more hydrophobic poloxamers, P403 exhibits improved aqueous solubility and enhanced compatibility with biological environments [100]. The relatively large hydrophilic domain of P403 facilitates its dispersion in aqueous media and contributes to the formation of stable micellar assemblies capable of encapsulating hydrophobic therapeutic agents within their PPO cores. Meanwhile, the outer PEO chains provide steric stabilization and reduce nonspecific interactions with biological components. The micellar structures formed by P403 play a crucial role in drug delivery applications [101]. Hydrophobic drugs can be incorporated into the PPO core through hydrophobic interactions, thereby significantly enhancing their apparent aqueous solubility and physicochemical stability. In addition, the hydrophilic PEO corona improves the colloidal stability of the carrier and promotes better biodistribution in physiological environments that allow to enhance the bioavailability and therapeutic performance of poorly water-soluble drugs and improve intracellular drug accumulation, thereby contributing to improved anticancer efficacy [102].

In addition to its self-assembly properties, P403 offers substantial versatility through its terminal hydroxyl (–OH) groups, which serve as reactive sites for further chemical modification. These functional groups enable conjugation with other polymers, cross-linkers, or bioactive molecules, facilitating the construction of multifunctional nanogels systems with enhanced structural stability and tailored release behavior [103]. Such modifications allow precise control over particle size, surface characteristics, and responsiveness to physiological stimuli, thereby expanding the scope of P403-based delivery platforms [104]. From a biological activity, the hydrated PEO corona of P403-based nanocarriers provides an effective steric barrier that minimizes protein adsorption and opsonization, resulting in prolonged systemic circulation time [105]. Furthermore, P403, characterized by a lower HLB value, possesses larger hydrophobic domains, which may disrupt cellular

membranes, inhibit cell proliferation, and induce cytotoxic effects by inhibiting ATP-dependent efflux transporters associated with multidrug resistance, thereby enhancing intracellular drug retention and improving therapeutic efficacy [106]. P403 has been reported to interact with cellular membranes and modulate membrane fluidity, which can facilitate intracellular drug transport [107].

1.4.3. Aplication of P403 into drug delivery system

P403 has emerged as a particularly promising amphiphilic polymer in biomedical and pharmaceutical applications, especially in the design of nanocarrier systems for anticancer drug delivery. In aqueous environments, P403 undergoes spontaneous self-assembly once its concentration exceeds the CMC value, forming nano-sized micelles or nanogels-like assemblies with a well-defined core–shell architecture. The hydrophobic PPO segments aggregate to form a compact inner core that efficiently encapsulates poorly water-soluble drugs, while the hydrophilic PEO chains extend outward to form a hydrated corona that stabilizes the nanostructure under physiological conditions. This structural organization significantly enhances the apparent solubility, colloidal stability, and bioavailability of hydrophobic drugs, thereby addressing one of the major challenges in conventional drug formulation [108]. As the temperature increases to approximately 37 °C, corresponding to physiological temperature, these hydrogen bonds are progressively disrupted, leading to dehydration of the PEO segments and enhanced hydrophobic interactions among the PPO blocks that controlled release agents and critical for maximizing antitumor efficacy while minimizing systemic toxicity [109].

Despite these advantages, P403-based systems still face certain limitations. One major challenge is their relatively physical instability and susceptibility to rapid erosion when exposed to changes in temperature or dilution conditions. This instability can lead to premature drug leakage and a burst-release effect, which may reduce the therapeutic efficiency of the encapsulated drugs [98]. Furthermore, the thermoresponsive nature of P403 can sometimes complicate their administration, as the transition from liquid to gel at physiological temperature may influence their injectability or oral delivery behavior [110]. To address these issues, various strategies have been proposed to conjugated P403 with natural polysaccharides, including chitosan, gelatin, or Fud, has been employed to enhance biological interactions, impart stealth properties, and improve nanoparticle stability and *in vivo* performance

[111,112]. These drug carrier systems have demonstrated promising potential as advanced platforms for the delivery of poorly water-soluble drugs and other therapeutic agents and significant interest in pharmaceutical as well as biomedical research.

1.5. Overview of fucoidan (Fud)

1.5.1. Origin and chemical structure of Fud

Fud is a naturally occurring sulfated polysaccharide predominantly extracted from the cell walls and extracellular matrices of brown seaweeds. As one of the major bioactive components found in brown algae, Fud has gained considerable interest in pharmaceutical and biomedical research due to its unique structural characteristics and diverse biological activities.

IUPAC name: [(2S,3S,4S,5S,6R)-4-hydroxy-5-methoxy-2,6-dimethylhexan-3-yl] hydrogen sulfate, which reflects the sulfated sugar moiety that constitutes the repeating structural unit of the polymer backbone.

Chemically, Fud is primarily composed of L-fucose residues and sulfate ester groups, which represent the key structural features responsible for its biological functionality. The backbone of Fud generally consists of α-L-fucopyranose units connected through glycosidic linkages (**Figure 1.14**). The sulfate groups, which play a crucial role in determining the biological and physicochemical properties of Fud, are mainly substituted at the C-2 and/or C-4 positions of the fucopyranose ring. In certain cases, sulfation may also occur at the C-3 position depending on the species and extraction conditions [113].

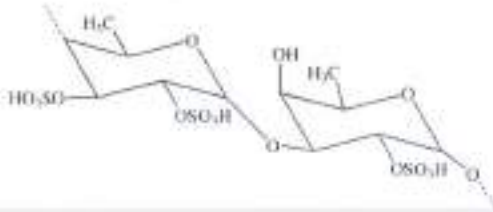

Figure 1.14. The chemical structure of Fud

The presence of these sulfate groups imparts a strong polyanionic character to Fud, enabling electrostatic interactions with positively charged biomolecules such as proteins, enzymes, growth factors, and cell surface receptors. Besides L-fucose, Fud may also contain minor amounts of other monosaccharides, including galactose, mannose, xylose, glucose, and uronic acids [114]. The molecular weight of Fud can vary widely depending on the algal species, extraction method, and purification

process, typically ranging from approximately 10 kDa to over 1000 kDa that are significantly influences the physicochemical behavior and biological performance of Fud. The presence of abundant hydroxyl (–OH) and sulfate ($–SO_3^-$) functional groups provides Fud with remarkable hydrophilicity and strong intermolecular interaction capabilities [115]. Fud typically exhibits a polyanionic character, as the sulfate groups present along the polymer backbone contribute negative charges under physiological conditions facilitating electrostatic interactions with positively charged biomolecules such as proteins, peptides, and cationic polymers. Another important physicochemical characteristic of Fud is its biodegradability and biocompatibility [116]. As a naturally occurring marine polysaccharide, Fud is generally considered safe and exhibits low cytotoxicity in biological systems. These properties make Fud an attractive candidate for biomedical and pharmaceutical applications [117]. Additionally, the abundant functional groups present in Fud allow chemical modification and functionalization, enabling the introduction of targeting ligands, crosslinking agents, or drug molecules. Such modifications can significantly enhance the stability, targeting ability, and therapeutic efficiency of Fud-based drug delivery systems [118].

1.5.2. Biological properties of Fud

Fud has attracted significant attention in biomedical and pharmaceutical research owing to its broad spectrum of biological activities [119]. These biological functions are closely related to its distinctive structural characteristics, including the presence of L-fucose residues, abundant sulfate ester groups, and a highly negatively charged polysaccharide backbone. Fud exhibits multiple pharmacological activities, including anticancer, anticoagulant, anti-inflammatory, antioxidant, antiviral, and immunomodulatory effects [119]. Among these biological properties, the anticancer activity of Fud has been the most extensively studied due to its potential application in cancer therapy by the induction of apoptosis, inhibition of cancer cell proliferation, suppression of angiogenesis, prevention of metastasis, and modulation of immune responses **(Figure 1.15)** [120]. Importantly, the sulfated structure of Fud allows it to interact with key signaling molecules involved in tumor development and progression, thereby influencing several intracellular pathways associated with cancer cell survival. In addition to inducing apoptosis, Fud can also inhibit cancer cell proliferation by regulating cell cycle progression. The uncontrolled proliferation of cancer cells is closely associated with dysregulation of cell cycle checkpoints. Several studies have

demonstrated that Fud can induce cell cycle arrest at different phases, particularly the G0/G1 or G2/M phase. This effect is mediated through the regulation of cyclins and cyclin-dependent kinases (CDKs), which are essential regulators of cell cycle transitions [121]. By disrupting these regulatory mechanisms, Fud effectively suppresses cancer cell growth and proliferation [122].

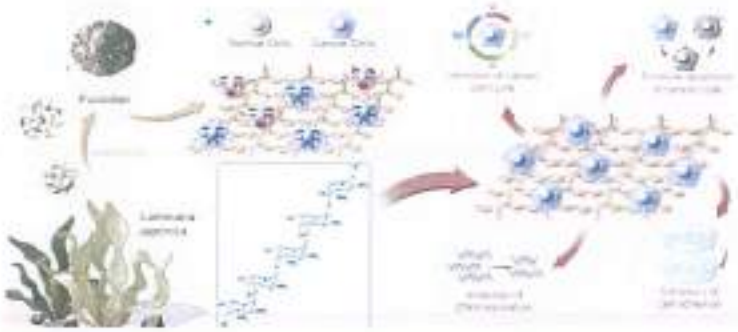

Figure 1.15. The effect of Fud on the cell cycle of cancer cells

Furthermore, Fud has demonstrated the ability to suppress cancer cell migration and metastasis, which are major causes of cancer-related mortality [123]. Another important aspect of Fud's anticancer activity is its ability to modulate MDR in cancer cells [124]. Several studies have suggested that Fud may suppress the expression or activity of P-glycoprotein, thereby increasing the intracellular retention of anticancer drugs and enhancing chemotherapy sensitivity. This property highlights the potential of Fud as an adjuvant agent capable of overcoming drug resistance and improving the effectiveness of conventional anticancer treatments [125]. In addition to its direct cytotoxic effects on tumor cells, Fud also exhibits immunomodulatory properties that contribute to its anticancer activity.

1.5.3. Fud-based strategies for drug delivery systems

In recent years, the development of nanotechnology has significantly advanced the field of biomedical sciences, particularly in the design of novel drug delivery systems aimed at improving the therapeutic efficacy and safety of pharmaceutical agents. Among various naturally derived biomaterials, Fud has emerged as a promising candidate for nanomedicine applications due to its excellent biocompatibility, biodegradability, low toxicity, and diverse biological activities [117]. The unique physicochemical and biological characteristics of Fud make it highly suitable for the fabrication of functional nanocarriers designed for targeted drug delivery, controlled drug release, and enhanced therapeutic performance. One of the most important advantages of Fud in nanomedicine lies in its abundant sulfate groups

and hydrophilic polysaccharide backbone, which provide numerous reactive sites for chemical modification and conjugation with other polymers, ligands, or therapeutic molecules. These structural features enable Fud to form various types of nanostructured delivery systems, including nanoparticles, nanogels, micelles, liposomes, and polymeric nanocomposites [126]. Through these nanostructures, Fud can serve not only as a structural component of the nanocarrier but also as a bioactive molecule that contributes to therapeutic effects. In drug delivery applications, Fud can also facilitate active targeting mechanisms through interactions with specific receptors overexpressed on cancer cells or tumor-associated endothelial cells. Several studies have demonstrated that Fud can interact with various biological receptors, including P-selectin, L-selectin, and scavenger receptors, which are often upregulated in tumor microenvironments [127]. These interactions can enhance cellular uptake of Fud-based nanocarriers and improve the intracellular delivery of therapeutic agents. Furthermore, Fud-based nanocarriers have shown great potential in combination chemotherapy, where multiple therapeutic agents are co-delivered within a single nanostructure [128]. The co-encapsulation of drugs with complementary mechanisms of action can produce synergistic anticancer effects, reduce the required dosage of individual drugs, and minimize adverse side effects. In addition, nanocarrier systems can provide controlled and sustained drug release profiles, allowing drugs to be released gradually over time in response to physiological stimuli [126].

1.6. A targeted ligand-folic acid

Folic acid (FA), also referred to as vitamin B9, is a water-soluble B-complex vitamin with a molecular weight of 441.4 g/mol and a melting point of approximately 250 °C. It is an indispensable micronutrient involved in one-carbon metabolism, playing a pivotal role in cellular proliferation, differentiation, and genomic stability. At the molecular level, FA functions as a one-carbon donor in the biosynthesis of purine nucleotides (adenine and guanine) and thymidylate, which are essential for DNA replication and thymidylate, which are essential for DNA replication and RNA transcription [129,130]. Consequently, folate metabolism is closely associated with processes of rapid cell division and nucleic acid synthesis. In physiological conditions, FA predominantly circulates in the bloodstream as 5-methyltetrahydrofolate, the biologically active reduced form. Following cellular uptake, it is enzymatically converted into tetrahydrofolate (THF) via dihydrofolate reductase (DHFR) in a

NADPH-dependent manner. THF and its derivatives subsequently act as critical cofactors in amino acid biosynthesis and nucleic acid metabolism, underscoring the essential role of folate in maintaining cellular homeostasis [131].

IUPAC NAME: (S)-2-[[4-[(2-amino-4-oxo-1H-pteridin-6-yl) methylamino] benzoyl] amino] pentanedioic acid

MOLECULE EQUATION:$C_{19}H_{19}N_7O_6$

Notably, many malignant cells exhibit an elevated demand for folate as a consequence of their accelerated proliferation rate, which is accompanied by the marked overexpression of folate receptors (FRs), particularly folate receptor alpha (FR-α), on the tumor cell surface [132]. In contrast, FR expression in most normal tissues is relatively low and largely confined to the apical surfaces of epithelial cells, thereby limiting accessibility from systemic circulation. Folate receptors are glycosylphosphatidylinositol (GPI)-anchored membrane glycoproteins comprising three major isoforms (FR-α, FR-β, and FR-γ), among which FR-α is the most clinically relevant due to its pronounced overexpression in a wide range of solid tumors, including breast and lung cancers [133]. The interaction between FA and FR-α is characterized by an exceptionally high binding affinity, with a dissociation constant (K_d) in the subnanomolar range (~0.1 nM), conferring high specificity toward folate receptor–overexpressing cancer cells [134]. The cellular transport of folic-modified drug delivery systems proceeds through a multistep and highly regulated process **(Figure 1.16)** [135]. Initially, FA-conjugated nanocarriers bind to FRs on the cancer cell surface, followed by internalization predominantly via clathrin-independent, caveolae-associated folate receptor–mediated endocytosis. Subsequent membrane invagination leads to the formation of endocytic vesicles, which undergo progressive acidification as they mature into early endosomes. The decrease in endosomal pH (to approximately pH 5–6) induces partial dissociation of the FA–FR complex, allowing folate receptors to be recycled back to the plasma membrane while retaining the nanocarrier intracellularly. This recycling receptor mechanism enables multiple rounds of ligand-mediated uptake, thereby enhancing intracellular drug accumulation and prolonging cellular retention. Moreover, endocytic sequestration and non-lysosomal trafficking pathways may reduce premature drug efflux and degradation, contributing to improved intracellular bioavailability. Importantly, the post-endocytic trafficking and intracellular fate of FA-functionalized nanocarriers are strongly

influenced by their physicochemical properties, including particle size, surface charge, and ligand presentation, which collectively regulate endosomal escape and subsequent drug release.

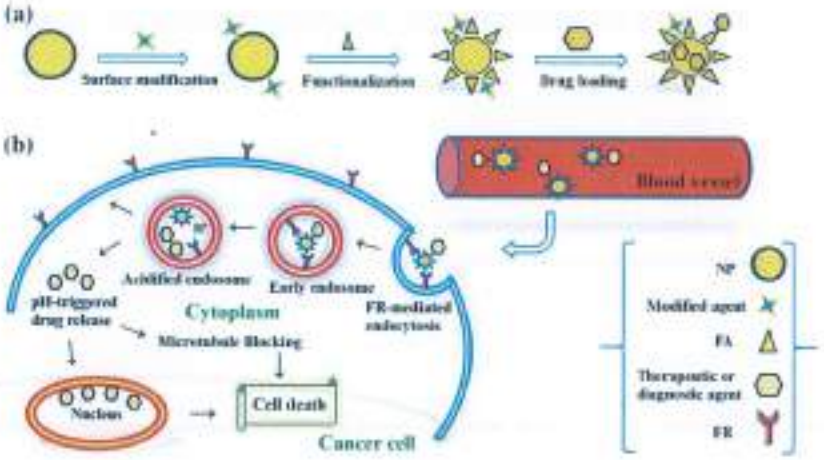

Figure 1.16. The representation of folate receptors mediated functionalization

CHAPTER 2. MATERIALS AND METHODS

2.1. Chemicals and equiments

2.1.1. Chemicals

Table 2.1. The list of used chemical agents

Number	Chemical names	Origin
Regents for synthesis		
1	Fucoidan	Viet-nam Fucoidan Joint Stock Company
2	Poloxamer P403	Sigma Aldrich (USA)
3	Folic acid	Merck (Germany)
4	Ethylendiamine	Acros Organics
5	3-amino-1-propanol	Acros Organics
6	1-ethyl-3–3-dimethylamino propyl carbodiimide (EDC, ≥97%)	Acros Organics
7	p-nitrophenyl chloroformate	Acros Organics
8	N-hydroxysuccinimide (NHS, ≥98%)	Acros Organics
9	Cisplatin	Sigma Aldrich (USA)
10	Curcumin	Sigma Aldrich (USA)
Organic solvents		
1	Ethanol	VN-CHEMSOL (Viet Nam)
2	Tetrahydrofuran	Fisher Scientific
3	Diethyl ether	Fisher Scientific
4	Dimethylfomanide	Fisher Scientific
5	Dimethyl Sulfoxide	Fisher Scientific
Reagent for cell culture		
1	Human dermal fibroblast cells (HDF)	ATCC (US)
2	Human breast cancer cells (MCF-7)	ATCC (US)
3	Rhodamine B (RhB)	Biochorm (Berlin, Germany)
4	Dulbecco's Modified Eagle Medium (DMEM)	Biochorm (Berlin, Germany)

5	Fetal bovine serum (FBS)	Biochorm (Berlin, Germany)
6	Trypsin-EDTA	Biochorm (Berlin, Germany)
7	Penicilin-streptomycin (P/S)	Biochorm (Berlin, Germany)

2.1.2. Equipment

Table 2.2. The list of used equipments

Number	Equipments' name
Synthesis equipment	
1	Analytical balance (OHAUS pioneer PA114, US)
2	Temperature-controlled magnetic stirrer (VELP Scientifica, Italy)
3	Freeze dryer (EYELA FDU-1200, Japan)
4	Centrifuge (Hermle Z32HK, Germany)
5	Rotary evaporator (Buchi Rotavapor R114, Thụy Sĩ)
6	Ultrasonic bath (Elmasonic S 80H, Germany)
Analytical instruments	
1	FT-IR spectrometer (PerkinElmer Frontier, Australia)
2	NMR Spectrometer (1H-NMR, Bruker Avance 500MHz)
3	Transmission electron microscopes (TEM, Jeol JEM-1400)
4	UV–vis spectrophotometer (UV-1900, Shimadzu, Japan)
5	Dynamic light scattering (Horiba SZ-100, Japan)
6	Microplate reader (HumaReader HS)
7	Inductively coupled plasma mass spectrometry (ICP–MS, NexION 2000, PerkinElmer, MA, USA)
8	Fluorescence microscope (LSM780 NLO, Zeiss, Germany)
9	Confocal laser scanning microscopy (CLSM)

2.2. Experiment

2.2.1. Synthesis of amphiphilic copolymers Fud-P403

2.2.2.1. Activation of P403 (NPC-P403-OH)

P403 (2.5 mmol) was initially reacted with NPC (5 mmol) in a three-neck flask under vacuum at 65 °C for 6 h. After completion, the crude product was dissolved in 20 mL of THF and subsequently precipitated with a diethyl ether/hexane mixture (1:1, v/v). The precipitate was collected and dried by rotary evaporation to obtain NPC–P403–NPC as a white solid. Subsequently, NPC–P403–NPC (2 mmol) was re-dissolved in 20 mL of THF, and 20 mL of Ami solution was added dropwise under

continuous magnetic stirring at room temperature. The reaction was allowed to proceed for 24 h. The resulting product was then precipitated using the diethyl ether/hexane mixture (1:1, v/v) and purified by rotary evaporation to yield NPC-P403-OH. Structural characterizations were carried out using ^{1}H-NMR and FTIR spectroscopy.

2.2.2.2. Synthesis of amino-terminated Fud (Fud-EDA)

5 g of Fud was dispersed in 100 mL of DIW and stirred at 40 °C for 30 min after that the carboxyl groups of Fud were subsequently activated by the addition of EDC (1.92 g, 10 mmol) and NHS (1.6 g, 13.9 mmol), and the reaction mixture was maintained under continuous stirring for 1 h. The activated solution was then slowly dropwised into 200 µL EDA (3.0 mmol) solution under constant stirring. The coupling reaction was allowed to proceed at room temperature for 24 h, promoting the formation of amide linkages and yielding the amine-functionalized derivative. The resulting product was purified by dialysis against deionized water (MWCO 3.5 kDa) to eliminate residual reagents and low-molecular-weight impurities, followed by freeze-drying to obtain Fud–EDA as a dry product. The chemical structure of the obtained derivative was confirmed by ^{1}H-NMR and FTIR spectroscopy

To further evaluate the degree of amination, the content of primary amine groups on the Fud backbone was determined using the TNBS colorimetric assay with L-alanine as a standard, reported by Hai V. Ngo, et.al. [136]. Briefly, a calibration curve was constructed from L-alanine for quantitation of amine groups. At the same time, 1 g Fud–EDA was dissolved in 5 mL of 0.1 M $NaHCO_3$ solution, followed by the addition of 2.5 mL of TNBS solution (0.01% w/v). The mixture was incubated at 37 °C for 2 h to ensure complete reaction between TNBS and free amine groups. The reaction was then quenched by adding 1.25 mL of 1 M HCl, and the absorbance was recorded at 335 nm using a UV–Vis spectrophotometer. The amine content was subsequently calculated based on the established calibration curve.

2.2.2.3. Synthesis of Fud-P403 copolymers

NPC-P403-OH (4.5 g) was dissolved in 100 mL of deionized water at 4 °C. Meanwhile, Fud–EDA (500 mg) was pre-activated using EDC/NHS chemistry, and the activated solution (50 mL) was added dropwise into the polymer solution under continuous stirring. The reaction was maintained for 24 h to enable covalent coupling. The mixture was then purified by dialysis (MWCO 12–14 kDa) to remove unreacted

species, followed by lyophilization to obtain the Fud–P403 copolymers. Structural characterization was performed using ^{1}H-NMR and FTIR, while morphological properties were evaluated by DLS and UV–Vis spectroscopy, respectively.

2.2.2. Synthesis of FA-Fud-P403

The FA-Fud-P403 copolymers was synthesised via the utherane linkage formation amine groups (-NH_2) and the carboxyl groups (–COOH) via an EDC/NHS-mediated coupling reaction (**Figure 2.1**). 25 g FA (0.06 mmol) was solubilized in 15 mL of DMSO, followed by activation using EDC (21.1 mg, 0.11 mmol) and NHS (16 mg, 0.13 mmol) for 1 h, then slowly introduced into an aqueous solution of Fud–P403 (50 mg in 10 mL DIW) under continuous stirring, and the reaction was carried out for 30 min under light-protected conditions. Afterward, the reaction mixture was subjected to dialysis using a cellulose membrane (MWCO ~3.5 kDa) to eliminate excess reagents and organic solvent. The purified product was subsequently collected by freeze-drying, yielding the FA–Fud–P403 copolymers. Structural characterizations were performed using ^{1}H-NMR UV-Vis and FTIR techniques, while the nanogels size distribution and surface charge were analyzed by DLS. The degree of FA substitution was quantified using UV–Vis spectroscopy at 280 nm.

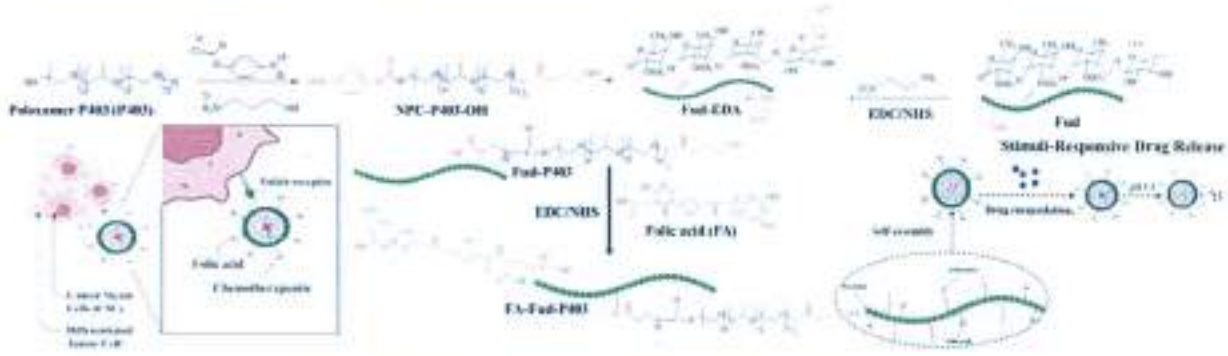

Figure 2.1. The syhthetic schemes of FA–Fud–P403 copolymers

2.2.3. Determination of critical micellar concentrations for nanogels formation

Amphiphilic copolymers containing hydrophobic PPO blocks and hydrophilic PEO blocks readily self-assemble into micelles in aqueous solution. Above a certain concentration, these copolymers were self-assembled into micellar structures in which the hydrophobic PPO segments form the inner core, while the hydrophilic PEO segments constitute the outer shell, thereby stabilizing the micelles, as illustrated in the **Figure 2.2**. Briefly, a KI/I_2 stock solution was prepared by dissolving 0.25 g of iodine (I_2) and 0.5 g of potassium iodide (KI) in 25 mL of distilled water. For CMC

determination, a series of 20 copolymers solutions with concentrations ranging from 0.00001 %wt to 0.1 %wt was prepared was supplemented with 10 µL of the KI/I_2 solution and incubated in the dark at room temperature for 12 hours prior to measurement. The UV absorbance of the samples at 366 nm was recorded using a UV–Vis spectrophotometer (Shimadzu UV-2401, Shimadzu, Tokyo, Japan). Absorbance values were plotted as a function of the logarithm of copolymers concentration. The CMC was determined as the concentration at which a significant increase in absorbance occurred. The absorbance intensity corresponding to I_2 was plotted against copolymers concentration at 366 nm [16].

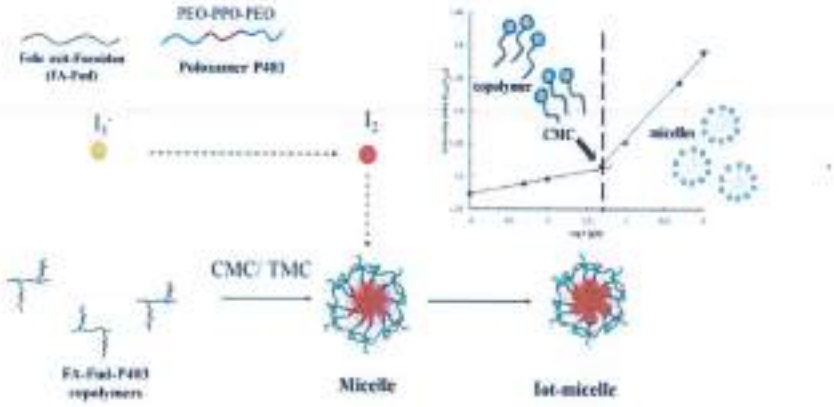

Figure 2.2. The schematic diagram of the iodine method

2.2.4. Co-loading of Cur and Cis in FA-Fud-P403 nanogels (FA-Fud-P403@Cur/Cis)

Cur (5 mg) was initially solubilized in mixture solvent of ethanol and dichloromethane (7:3, v/v), then this solution was slowly introduced gradually into an aqueous FA–Fud–P403 solution (100 mg in 10 mL deionized water) under probe sonication at 4 °C for 30 min. The resulting suspension was subjected to solvent evaporation, redissolved in 5 mL of DIW before centrifuged at 7000 rpm for 20 min at 20 °C to eliminate free Cur to collected and freeze-dried to yield Cur-loaded nanogels (FA–Fud–P403@Cur). Subsequently, Cis (5 mg) was dissolved in DMF and slowly added into the FA–Fud–P403@Cur dispersion (100 mg in 10 mL). The mixture was maintained at 20 °C for 30 min in a thermostatically controlled bath to facilitate drug incorporation. The resulting formulation was purified by dialysis to remove residual solvent, followed by centrifugation to separate free Cis. The purified product was then lyophilized to obtain dual drug-loaded nanogels (FA–Fud–P403@Cur/Cis).

The Cur content in the nanogels was quantified by UV–Vis spectrophotometry (λ = 426 nm, Agilent, USA), while the Cis content was determined using ICP–MS. The drug loading capacity (%DL) and entrapment efficiency (%EE) of Cur and Cis were calculated according to the following equations [137]:

$$\%EE = \frac{\text{weight of drug encapsulated into nanogels}}{\text{initial weight of feeding drug}} \times 100$$

$$\%DL = \frac{\text{weight of drug encapsulated into nanogels}}{\text{total weight of nanogels and drug}} \times 100$$

2.2.5. Determination of stability of drug-loaded nanogels

The physicochemical stability of FA–Fud–P403@Cur/Cis nanogels was investigated by evaluating temporal changes in hydrodynamic size and Cur retention. The nanogels were dispersed in PBS (pH 7.4) and Dulbecco's Modified Eagle Medium (DMEM), followed by incubation at 37 °C to mimic physiological environments. At predetermined intervals (0, 24, 48, 72, and 96 h), the colloidal behavior of the system was analyzed by DLS to detect size distribution. Concurrently, the stability of the encapsulated Cur was assessed using UV–Vis spectrophotometry. Specifically, 1 mL aliquots of the nanogels suspension were withdrawn at each time point, mixed with an equal volume of ethanol, and the absorbance was measured at 420 nm. The remaining Cur content was subsequently calculated by comparison with the initial loading, providing the percentage of drug retained within the nanogels throughout the incubation period.

2.2.6. Determination of *in vitro* release profiles and release kinetics of drug from nanogels

FA-Fud-P403@Cur/Cis, free Cur, and free Cis were diluted in the distilled water after that each sample was added to Polysorbate 80 (1%) to increase the dispersion of as well as to inhibit the precipitate of Cur, then place in these mixture solutions into the cellulose membrane package to dialysis (MWCO 3.5kDA) in the phosphate-buffered saline (PBS) solutions (pH 7.4 and 5.5 respectively) at 37°C. At a certain time, the mixture samples dialyzed into two PBS solutions as pH 7.4 and 5.5 were withdrawn 1 mL of sample out of the dialysis bags and continued to add 1 ml PBS solution to maintain the constant volume of sample. The release profile of drug-loaded into nanogels was calculated by the standard curve that concentration of Cur was quantified by UV–Vis spectrophotometry at 430 nm, while the Cis content was

measured using an ICP–MS. The cumulative release percentage (CR%) of Cur and Cis was calculated according to the following equation:

$$CR\ (\%) = \sum_{t=4}^{t=a} \frac{M_t}{M_0}\ x\ 100$$

Where M_t is the amount of Cur/Cis released at a certain time (t)

M_o is the amount of Cur/Cis encapsulated in the nanogels.

The drug release mechanism was analyzed by fitting the release profiles to various kinetic models, including Zero-order, First-order, Higuchi, and Korsmeyer–Peppas models. The coefficient of determination (R^2) was used to identify the model that best described the release behavior of Cur and Cis from the nanogels. In addition, the MDT was calculated to evaluate the duration of sustained release of the active compounds within the nanogels, according to the following equation:

$$MDT\ (hour) = \left(\frac{n}{n+1}\right)k^{-\frac{1}{n}}$$

Where: n was the exponent and k were the constant rate of released profile for the Korsmeyer equation

2.2.7. Determination of *in vitro* hemolysis assay

Whole blood obtained from mice was first centrifuged at 1000 rpm for 10 min to isolate red blood cells (RBCs). The collected cells were subsequently re-suspended in PBS pH 7.4 and adjusted to a final concentration of 5% (v/v). For hemocompatibility assessment, 500 µL of the RBC suspension was incubated with an equal volume of FA–Fud–P403@Cur/Cis nanogels dispersions at concentrations ranging from 6.25 to 100 ppm. The mixtures were maintained at 37 °C for 1 h to allow potential membrane interactions. Following incubation, samples were centrifuged at 2500 rpm for 10 min to sediment intact erythrocytes

The absorbance of the supernatant was then recorded at 540 nm using a microplate reader. The hemolytic activity was calculated using a standard formula, with Triton X-100 representing complete positive control and PBS serving as the negative control.

$$\text{Hemolysis ratio } (\%) = \frac{A_{sample} - A_{negative\ control}}{A_{positive\ control} - A_{negative\ control}}$$

2.2.8. Determination of *in vitro* cytotoxic assay

2.2.9.1. In vitro cytotoxic studies

The cytotoxicity of Fud-P403 and FA-Fud-P403 nanogels was assessed by WST-1 assay. Briefly, 100 µL medium containing either HBF or MCF-7 cells (10^4

cells/well) was seeded into 96-well plate and cultured in the incubator under the standard culture conditions (37 °C, 90% humidity, and 5% CO_2) for 24 h. Then, media were removed, and cells were treated with 100 µL DMEM media containing FA-Fud-P403/P407 nanogels (125 ppm) for an additional 24 h. Then, 10 µL of WST-1 solution was added into each well , followed by a 1-h incubation period. The cytotoxicity of nanogels was determined by measuring the absorbance of reacted solution at 450 nm using a microplate reader. Cell viability was calculated as the percentage relative to the untreated control group, following to the equation:

$$\text{Cell viability (\%)} = \frac{A_t - A_b}{A_c - A_b} \times 100$$

With the A_t, A_b and A_c are the sample tests, blank (pure DMEM) and control sample (DMEM), respectively

Furthermore, to confirm cell viability, a Live/Dead assay was conducted. Briefly, 100 µL of the WST-1 reacted solution was discarded, and the cells were rinsed once with PBS. Subsequently, 100 µL of PBS containing 2 µM calcein-AM (acetoxymethyl ester derivative of calcein) and 4 µM ethidium homodimer-1 (EthD–1) was added to each well. After 15 min of incubation, the fluorescence-stained cells were qualitatively observed under a fluorescence microscope (Nikon, Japan) to assess their morphological integrity.

2.2.9.2. Qualitative uptake study

Cellular uptake was evaluated to investigate the intracellular internalization and folate receptor–mediated targeting of FA-Fud-P403 nanogels in MCF-7 cells. Rhodamine B (RhB) was used as a fluorescent probe for visualization. RhB (1 mg/mL) was incorporated into FA-Fud-P403 solution (10 mg/mL) under stirring for 4 h at 4 °C in the dark, followed by dialysis (MWCO 3.5 kDa, 6 h) to remove free dye. The purified nanogels were collected and lyophilized.MCF-7 cells were seeded on glass coverslips in 12-well plates (2×10^5 cells/mL) and incubated for 24 h. Cells were then treated with blank or RhB-loaded nanogels for 4 h, washed with PBS, fixed with 4% paraformaldehyde (30 min), and stained with DAPI (15 min). Intracellular fluorescence and distribution were observed using confocal laser scanning microscopy (CLSM, Zeiss LSM780 NLO). The resulting fluorescence images provided qualitative evidence of nanogels internalization efficiency and intracellular distribution patterns.

2.2.9.3. Synergism effect of two-drug combination against cancer cells

The synergism effect of two-drug combination analysis is based on the Combination Index (CI) that is determined by the isobologram formula.

$$CI = \frac{(D)_1 + (D)_2}{(D_X)_1 + (D_X)_2}$$

Where the $(D)_1$ and $(D)_2$ are the concentration in the combinational inhibition, $(D_x)_1$ and $(D_x)_2$ are the single-dose concentration of Cis and Cur, respectively that inhibit the growth of MCF-7 calculated from the equation $D=D_m[f_a/(1-f_a)]^{1/m}$, with Dm, fa and m as dose required for 50% effect, the affected fraction and coefficient of the dose-effect curve, respectively. The results of isobologram equation are used for analysis of the effect of drug combination, where CI < 1, CI = 1, and CI >1 determines synergism, additive effect, and antagonism, respectively [138]

2.2.9. Determination of *in vivo* tumor inhibition

All in vivo experiments were conducted in compliance with the guidelines approved by the Animal Care and Use Committee of Tra Vinh University (Approval No. 285/GCN.ĐC-HĐĐĐ). Female BALB/c mice (6–8 weeks old) were subcutaneously inoculated with MCF-7 cells (1×10^7 cells) to establish a xenograft tumor model. Once the tumor volume reached approximately 150 mm^3, the animals were randomly assigned into four groups (n = 4 per group), including: (i) saline as a negative control, (ii) free Cis as a positive control, (iii) FA–Fud–P403@Cis, and (iv) FA–Fud–P403@Cur/Cis. All formulations were administered via intravenous injection through the tail vein, with the Cis dosage fixed at 2 mg/kg across all Cis-containing groups. Treatments were performed at 3-day intervals. Throughout the study, body weight and tumor progression were monitored at designated time points. Tumor dimensions were measured using a digital caliper, and the tumor volume was calculated using the formula ½ × (length × $width^2$). At the end of the treatment period (day 15), the mice were sacrificed, and tumor tissues were harvested for histopathological analysis using hematoxylin and eosin (H&E) staining **(Figure 2.3)**.

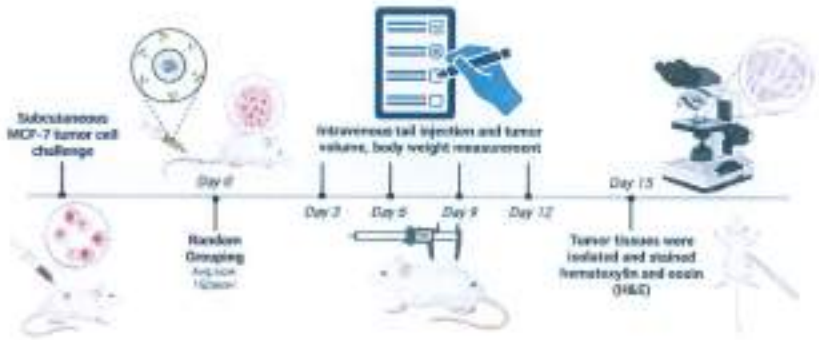

Figure 2.3. The schematic illustration of MCF-7 tumor-bearing mice and treatment with different drug formulations

2.2.10. Statistical analysis

The data was exhibited by One-way Anova, where all experiments were carried out three times and shown under the form of means ± standard deviation, with the (*), (**), and (***) as for the $p < 0.05$, $p < 0.01$, and $p < 0.001$, respectively corresponding to the statistically significant. While the non-statistically significant ($p > 0.05$) was illustrated as ns.

CHAPTER 3. RESULTS AND DISCUSSION

3.1. Characterizations of FA-Fud-P403 copolymers

3.1.1. Structural properties of FA-Fud-P403 nanogels

3.1.1.1. Structural characterization of NPC-P403-OH

The formation of NPC–P403–NPC and its subsequent conversion to NPC–P403–OH proceeds via a nucleophilic substitution mechanism involving carbonate activation. Initially, the terminal hydroxyl groups of P403 act as nucleophiles and attack the electrophilic carbonyl carbon of NPC, leading to the formation of activated carbonate intermediates. In the second stage, the primary amine group of 3-amino-1-propanol, acting as a stronger nucleophile, attacks the carbonyl carbon of the activated carbonate, resulting in the displacement of the nitrophenyl moiety and the formation of carbamate linkages. FTIR spectrum **(Figure 3.1)** provided the successful chemical modification of P403 and the formation of NPC-functionalized derivatives. The characteristic absorption bands of the P403 backbone were clearly observed in the range of 2978–2880 cm^{-1} corresponding to the stretching vibrations of $-CH_2$ and $-CH_3$ groups, confirming the presence of the PPO and PEO segments. Additionally, the strong absorption region from 1300 to 1000 cm^{-1} is attributed to the C–O–C ether linkage, which is a signature structural feature of P403. Upon functionalization with p-nitrophenyl chloroformate (NPC), several new spectral features emerged, confirming successful conjugation. Absorption band in the region of 1600–1500 cm^{-1} is assigned to the $-NO_2$ group attached to the aromatic ring, serving as a direct indicator of NPC incorporation. Importantly, a significant shift and the appearance of a new peak in the range of 1650–1770 cm^{-1} correspond to the C=O stretching vibration of ester groups (–COO–NPC) that suggests the formation of ester linkages between the hydroxyl termini of P403 and NPC, resulting in the formation of NPC–P403–NPC structures. Furthermore, the additional absorption band around 1644 cm^{-1} provides further insight into the reaction pathway that can be attributed to the urethane linkage (–NHCOO–), indicating that partial substitution reactions occurred.

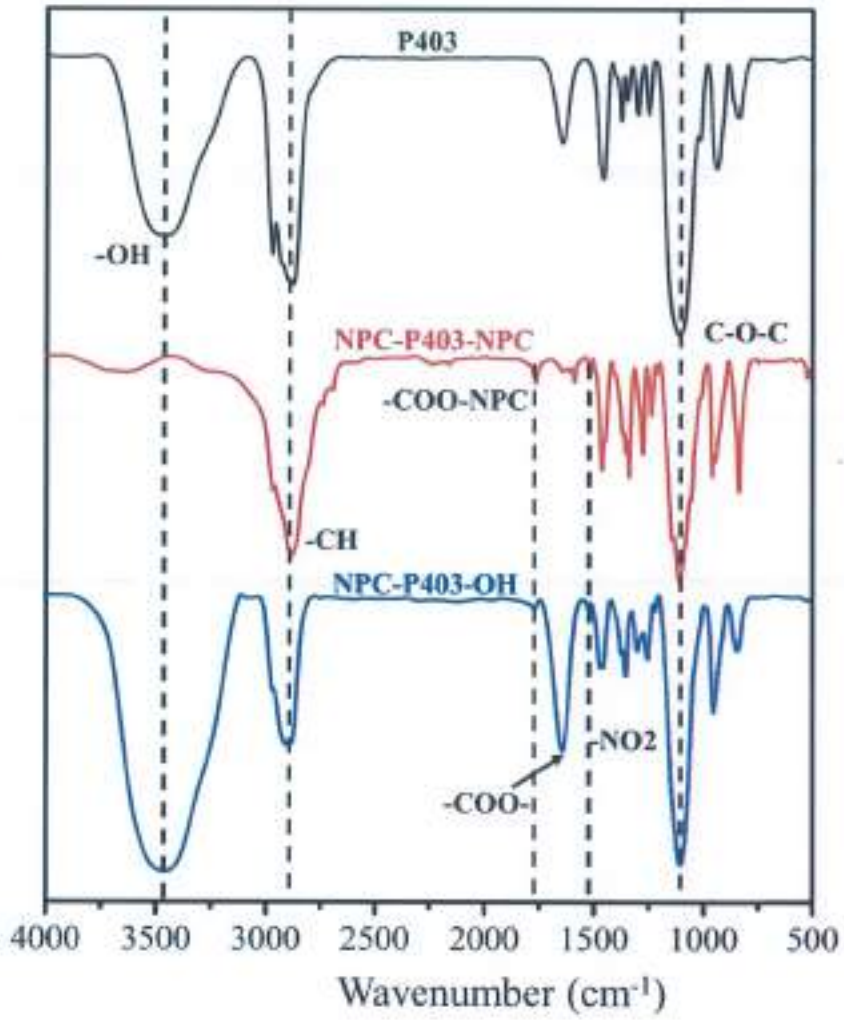

Figure 3.1. The FT-IR results of P403, NPC-P403-NPC, and NPC-P403-OH

Additonally, the ^{1}H- NMR spectrum of NPC–P403–NPC (**Figure 3.2**) clearly confirms the successful functionalization of P403 with 4-nitrophenyl chloroformate. Characteristic proton signals of the P403 backbone were observed, including a singlet at $\delta_H \approx 1.20$ ppm assigned to the methyl protons (–CH_3, c) of the PPO segment and a strong singlet at $\delta_H \approx 3.62$ ppm, corresponding to the methylene protons of the PEO blocks (–O–CH_2–CH_2–O–, d). Notably, the appearance of a new singlet at $\delta_H \approx 4.22$ ppm is attributed to the methylene protons of the –CH_2–O–NPC moiety (f') on the PEO chains, indicating the formation of carbonate linkages between the terminal hydroxyl groups of PEO and NPC. Furthermore, doublets at $\delta_H \approx 7.38$ ppm and $\delta_H \approx 8.32$ ppm are assigned to the aromatic protons (a and b) of the nitrophenyl ring, providing direct evidence for the incorporation of NPC moieties at both chain termini of P403. Similarly, the ^{1}H-NMR spectrum of NPC–P403–OH demonstrates the

structural features of both the P403 backbone. A singlet at $\delta_H \approx 1.13$ ppm corresponds to the methyl protons (–CH_3, c) of the PPO segment, while the characteristic methylene protons of the PEO blocks (–O–CH_2–CH_2–O–, d) appear in the range of $\delta_H = 3.61–3.63$ ppm. The presence of aromatic doublets at $\delta_H = 7.38–7.40$ ppm and 8.27–8.28 ppm is attributed to the aromatic protons of the NPC moiety, confirming the carbonate activation step. Importantly, a noticeable chemical shift of the methylene protons adjacent to the carbonate group from $\delta_H \approx 4.44$ ppm (–CH_2–O–NPC) to $\delta_H \approx$ 4.22 ppm was observed after reaction with 3-amino-1-propanol, indicating the displacement of the NPC group. In addition, a new singlet at $\delta_H \approx 1.7$ ppm is assigned to the methylene protons (–CH_2–, g) of the propyl chain of 3-amino-1-propanol, further confirming the formation of amino-terminated P403 via carbamate (–O–CO–NH–) linkages. These observations from FTIR and ^{1}H-NMR confirms the co-existence of multiple linkage types within the system, reflecting a more complex functionalization mechanism

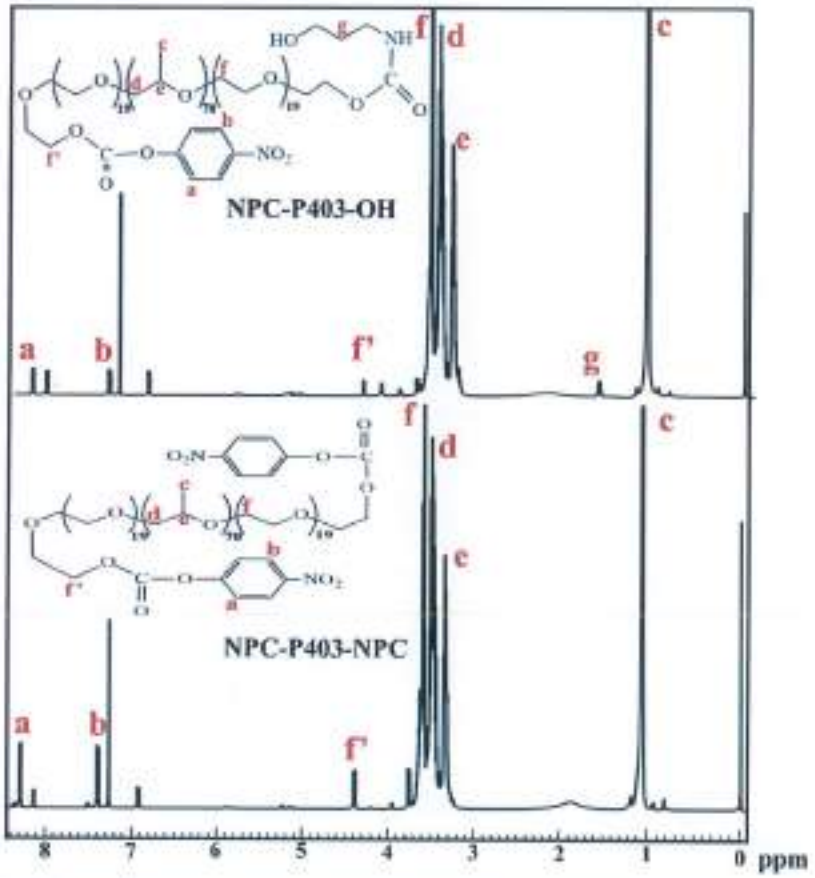

Figure 3.2. The ^{1}H-NMR results of NPC-P403-NPC and NPC-P403-OH

3.1.1.2. Structural characterization of Fud-EDA

The FTIR spectra **(Figure 3.3)** further corroborates the successful modification. Briefly, Fud and Fud-EDA display an absorption band in the range of 3500–3200 cm^{-1}, corresponding to the stretching vibrations of hydroxyl (–OH) groups inherent to the polysaccharide structure. The absorption band observed at approximately 1640 cm^{-1} are assigned to the asymmetric stretching vibration of the carboxylate ($–COO^-$) group, indicating the presence of glucuronic acid residues in Fud. Characteristic sulfate group absorptions are evidenced by the bands at 1260–1160 cm^{-1} and around 839 cm^{-1}, attributing to the asymmetric stretching of the S=O bond and C–O–S stretching vibration, respectively. Additionally, the absorption region between 1150 and 1000 cm^{-1} is associated with C–O–C stretching vibrations, confirming the saccharide ring structure of Fud. Notably, the FTIR spectrum of Fud-EDA shows new absorption bands in the range of 3100–3000 cm^{-1}, which were assigned to N–H stretching vibrations of amine groups from EDA. Furthermore, the appearance of a band in the region of 1500–1400 cm^{-1} is attributed to N–H bending vibrations, providing strong evidence for the formation of amide (–NH–CO–) linkages resulting from the conjugation between EDA and the carboxyl groups of Fud.

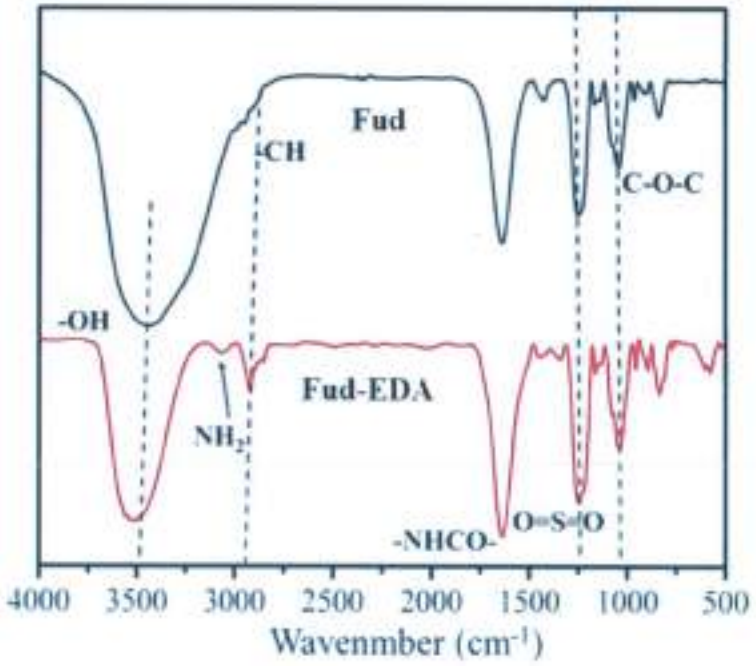

Figure 3.3. The FT-IR result of Fud and Fud-EDA

Furthermore, the ^{1}H-NMR spectrum of Fud-EDA **(Figure 3.4)** exhibited characteristic proton signals confirming the successful modification of Fud with EDA.

Broad signals observed in the range of δ_H = 3.7–5.4 ppm is attributed to the ring protons of Fud polysaccharide units. A distinct singlet at $\delta_H \approx 1.8$ ppm corresponds to the methyl protons (–CH_3) of the O-acetyl group (–$OCOCH_3$), indicating the presence of acetyl substituents on the Fud backbone. In addition, the appearance of a singlet at $\delta_H \approx 1.7$ ppm is assigned to the methylene protons (–CH_2–) of EDA, while the signal at around $\delta_H \approx 2.9$–3.1 ppm is attributed to the methylene protons adjacent to the amino group (–CH_2–NH–). These signals provide evidence for the conjugation of EDA to Fud via amide bond (–CONH–) formation between the amine groups of EDA and the carboxylate groups of Fud.

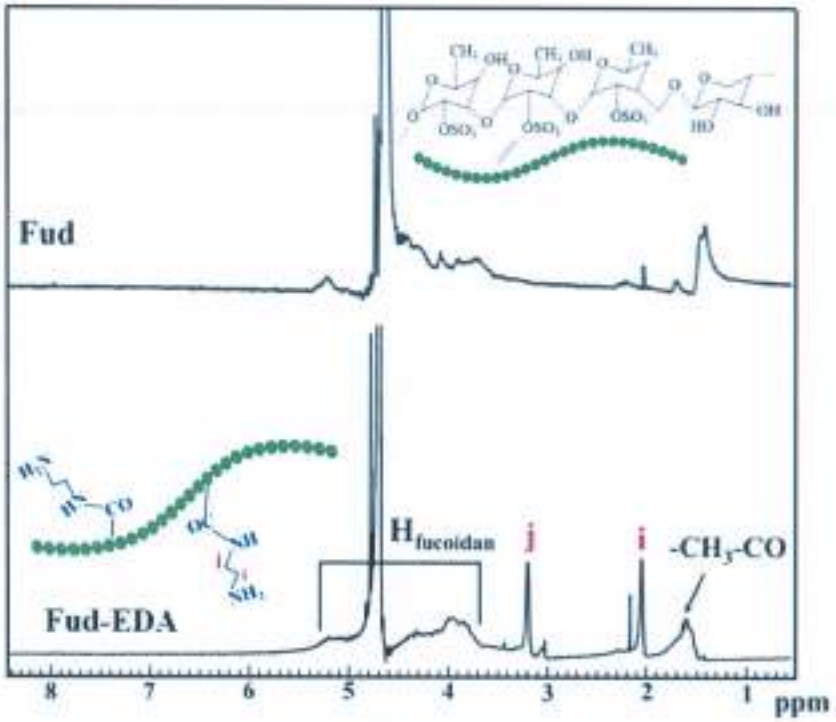

Figure 3.4.The ^{1}H-NMR results of Fud and Fud-EDA

The substitution degree of primary amine (–NH_2) groups on the Fud backbone plays a crucial role in determining the overall efficiency of subsequent functionalization processes, particularly in the conjugation of FA and amphiphilic copolymers. Based on the TNBS assay, the amine content was determined to be 2.13 ± 0.863 mmol/g, providing sufficient reactive sites for efficient FA coupling and P403 conjugation. This relatively high substitution degree indicates the successful incorporation of –NH_2 groups onto the Fud backbone that emonstrates that the modified Fud possesses an adequate and effective level of functionalization, providing a strong foundation for efficient FA coupling and subsequent P403 conjugation,

ultimately contributing to the development of a robust and well-defined multifunctional drug delivery system

3.1.1.3. Structural characterization of Fud-P403

The successful covalent conjugation of Fud onto P403 was rigorously confirmed by complementary FT-IR and ^{1}H-NMR analyses **(Figure 3.5 and 3.6)**, demonstrating both structural transformation and chemical bond formation. FT-IR analysis **(Figure 3.5)** provides clear evidence of urethane bond formation. The spectrum of NPC-P403-OH exhibits a strong carbonyl stretching band at 1769 cm^{-1}, characteristic of the activated carbonate group. The significant band disappears carbonyl absorption emerges at 1644 cm^{-1}, which is attributed to the carbamate (–NHCOO–) linkage. Furthermore, the characteristic $–NO_2$ asymmetric and symmetric stretching vibrations of the p-nitrophenyl group (1600–1500 cm^{-1}), clearly visible in NPC-P403-OH, are absent in Fud-P403, confirming the displacement of the NPC by Fud-EDA. Importantly, the broad –OH stretching band (3600–3200 cm^{-1}) and the sulfate group vibration (O=S=O, 1260–1160 cm^{-1}) confirm the presence of Fud. Meanwhile, the characteristic C–H stretching vibrations of P403 (2970–2879 cm^{-1}) and the ether C–O–C stretching bands (1300–1000 cm^{-1}).

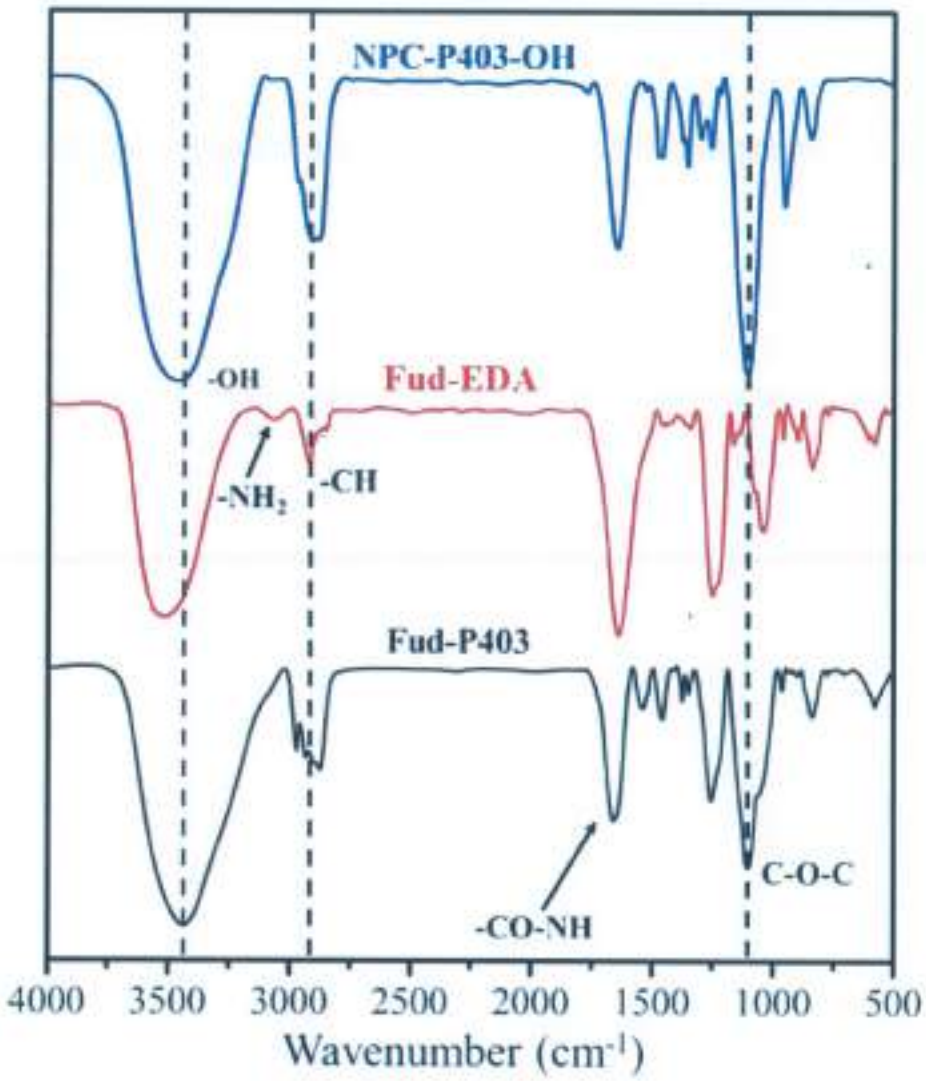

Figure 3.5.The FT-IR results of NPC-P403-OH, Fud-EDA, and Fud-P403

In addition, the ^{1}H-NMR analysis **(Figure 3.6)** further corroborates the aromatic proton signals of NPC at δ_H = 7.38–7.40 ppm and 8.27–8.28 ppm, alongside with the methylene signal at δ_H = 4.43 ppm corresponding to –CH_2–O–NPC. A singlet at δ_H = 1.74 ppm is assigned to the methylene protons of the EDA, while the signal at δ_H = 3.04 ppm corresponds to –CH_2–NH– protons. Additionally, the new signal at δ_H = 4.22 ppm is attributed to –CH_2–O– within the newly formed carbamate structure, replacing the original –CH_2–O–NPC resonance. The characteristic signals of P403 are retained, including the PPO methyl protons at δ_H = 1.10 ppm and the PEO methylene protons in the region δ_H = 3.5–3.8 ppm. Signals of Fud are observed within δ_H = 3.7–5.4 ppm, consistent with its polysaccharide backbone.

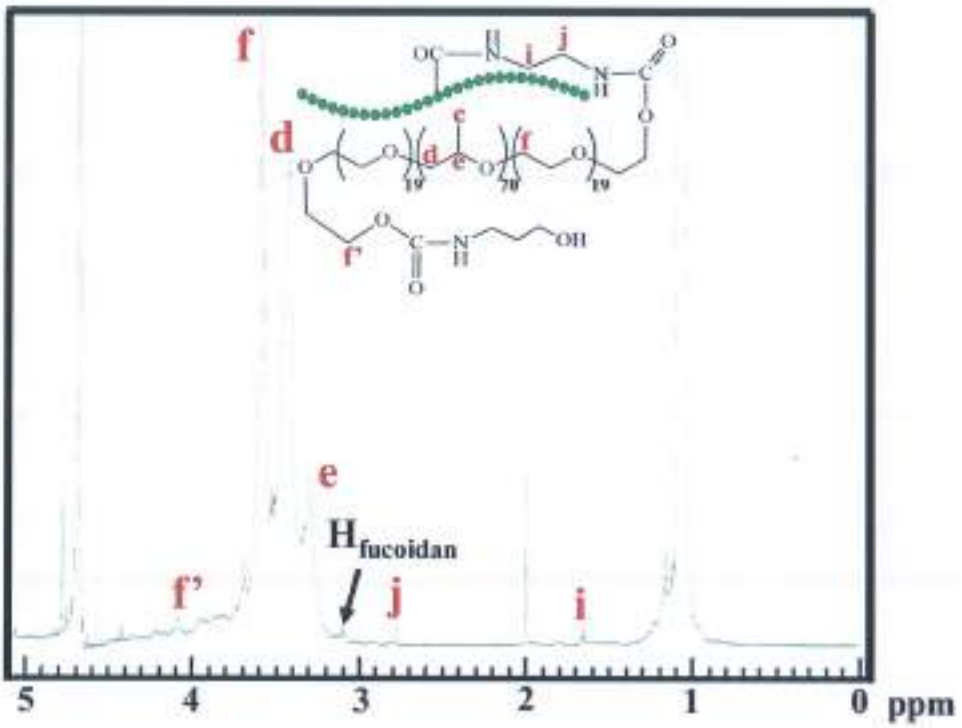

Figure 3.6.The ^{1}H-NMR result of Fud-P403

3.1.1.4. Structural characterization of FA-Fud-P403

FA functionalization of Fud–P403 copolymers was achieved via a sequential two-step reaction. Initially, NPC–P403–OH was reacted with the primary amine groups of Fud–NH_2, leading to the formation of Fud–P403 through urethane linkage formation. In the subsequent step, FA was grafted onto the Fud–P403 backbone via amide bond formation, resulting in FA–Fud–P403 copolymers. The successful incorporation of FA into the copolymers structure was verified using complementary analytical techniques, including UV–Vis spectroscopy, ^{1}H-NMR, and FTIR analysis. The FT-IR spectra on **Figure 3.7** confirmed the presence of characteristic functional groups in FA-Fud-P403 copolymers. the characteristic bands at 1300–1000 cm^{-1} are assigned to the ether (C–O–C) stretching vibrations of the P403 polyether chains, while the signals at 2995–2980 cm^{-1} correspond to aliphatic –CH (–CH_2 and –CH_3) stretching modes. The broad absorption in the 3500–3450 cm^{-1} region is attributed to –OH stretching vibrations, originating from both the polysaccharide backbone of Fud and the terminal hydroxyl groups of P403 [126,139,140]. While, the presence of sulfated groups from Fud is confirmed by the distinct absorption in the 1250–1150 cm^{-1} region, corresponding to the O=S=O stretching vibration, indicating that the sulfated polysaccharide structure is well preserved after conjugation with P403 [141].

Upon further functionalization with FA, new spectral features emerge, confirming the successful grafting of the aromatic ligand. Specifically, the bands observed in the 1485–1459 cm^{-1} region are assigned to the aromatic ring vibrations of FA. This provides direct evidence for the introduction of the folate moiety into the polymeric framework. Importantly, a pronounced shift in the carbonyl stretching region is observed upon conjugation. The C=O band, originally located at 1679 cm^{-1} for free FA, is shifted to a lower wavenumber (~1641 cm^{-1}) in the FA–Fud–P403 spectrum that consistent with the formation of a covalent linkage between the carboxyl groups of FA and the amine functionalities of Fud–P403 [142]. The decreased wavenumber can be attributed to the conversion of the free carboxylic acid into an amide (–CONH–) as well as the contribution of hydrogen bonding interactions within the polymeric network, both of which reduce the effective bond order of the C=O group.

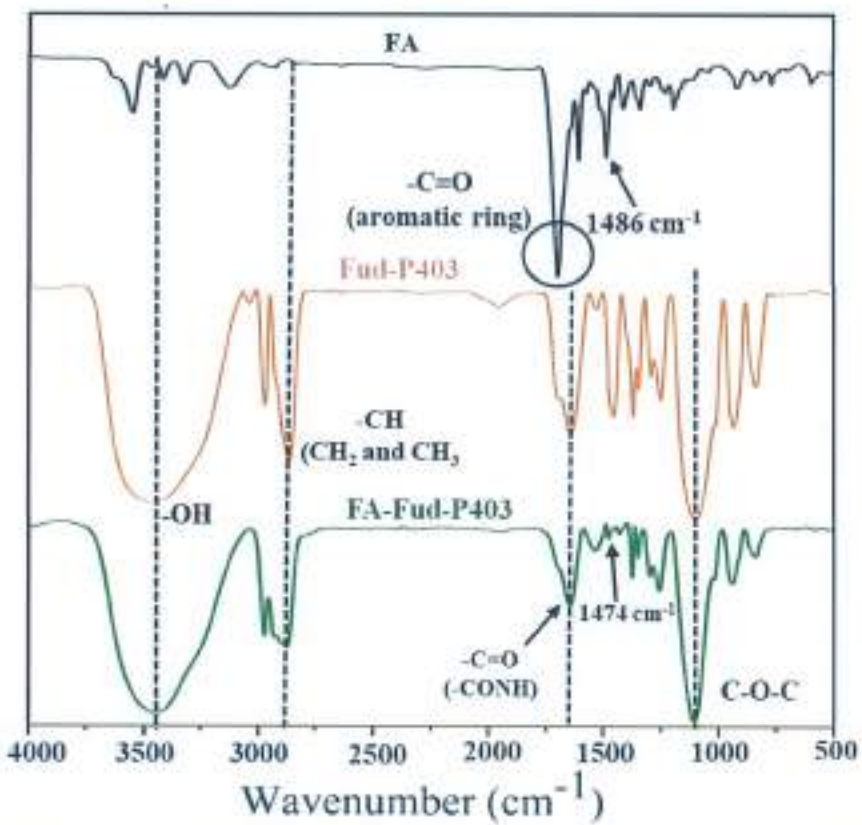

Figure 3.7.The FT-IR results of FA, Fud-P403, and FA-Fud-P403

As shown on **Figure 3.8**, the ^1H NMR spectrum of FA–Fud–P403 revealed several distinct signals corresponding to its structural components. The spectrum is dominated by the characteristic resonances of the P403 block copolymers. A strong and broad signal observed in the region of $\delta_H \approx 3.2–3.7$ ppm is attributed to the

methylene protons of the poly(ethylene oxide) (PEO) segments (–OCH_2–CH_2O–), reflecting the hydrophilic chains of the copolymers. In addition, the distinct peak at $\delta_H \approx 1.0–1.2$ ppm corresponds to the methyl (–CH_3) protons of the poly(propylene oxide) (PPO) blocks, while the overlapping methine and methylene protons of PPO contribute to signals in the $\delta_H \approx 3.3–3.8$ ppm region [143]. The presence of these well-defined peaks confirms that the amphiphilic P403 structure is preserved after the conjugation process. Signals associated with the Fud backbone are also clearly observed. The broad multiplet in the range of $\delta_H \approx 3.0–5.5$ ppm is assigned to the ring protons of the sugar units (H_{Fud}), which typically overlap due to the heterogeneous and polysaccharidic nature of Fud. Furthermore, a small but distinguishable resonance around $\delta_H \approx 1.8–2.0$ ppm is attributed to N-acetyl protons, indicating successful chemical modification of the polysaccharide [144]. Crucially, after conjugation with FA, new signals emerge in the downfield aromatic region. Specifically, peaks appearing at $\delta_H \approx 6.8–7.1$ ppm and 7.5–7.8 ppm are assigned to the aromatic protons of the FA [145]. These signals are absent in the spectrum of Fud–P403 but become clearly visible in FA–Fud–P403, providing direct evidence for the successful grafting of FA onto the polymeric backbone.

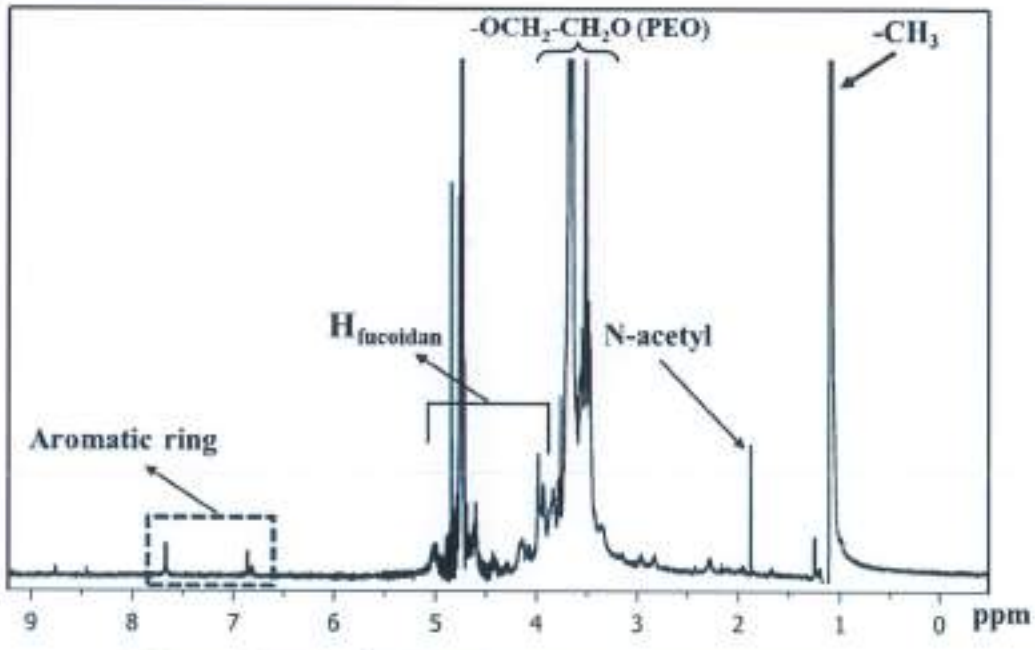

Figure 3.8. The ^{1}H-NMR result of FA-Fud-P403

Furthermore, the successful conjugation of FA into the Fud–P403 copolymers was evaluated using UV–Vis spectroscopy, as presented in **Figure 3.9.** The degree of FA incorporation was quantified at 280 nm corresponding to the π–π^* electronic

transition of the pteridine ring in FA. Based on a calibration curve established from FA solutions at different concentrations, the FA content in the FA–Fud–P403 copolymers was calculated to be approximately 5.31% [146]. Overall, the combined FT-IR, ^{1}H-NMR, and UV-Vis spectral evidence confirms the successful synthesis of the FA–Fud–P403 copolymers highlighting the efficiency of the conjugation strategy and demonstrating that the final system integrates the targeting functionality of FA with the structural and amphiphilic properties of the Fud–P403 platform. Importantly, the presence of FA is expected to provide effective ligand–receptor interactions without significantly altering the physicochemical stability or self-assembly behavior of the polymer system.

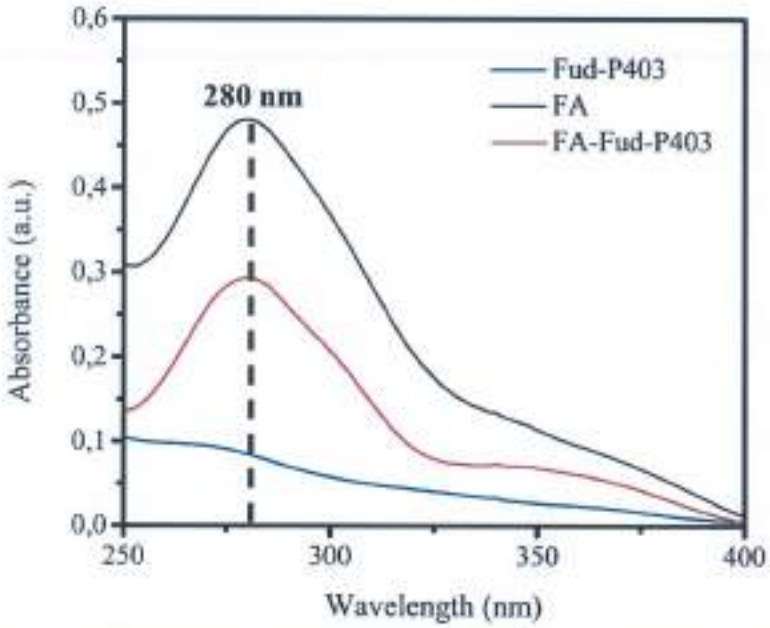

Figure 3.9.The UV-Vis results of Fud-P403, FA, and FA-Fud-P403

3.1.2. Physicochemical characterizations of FA-Fud-P403

3.1.2.1. CMC determination of nanogels

The CMC value is a key parameter for evaluating the stability of nanogels in aqueous media as well as their capacity to encapsulate hydrophobic drugs. In this study, the CMC was determined using the iodine method, using the iodine ions penetration into the hydrophobic PPO domains of P403 that converted I_3^- to I_2 in the presence of excess KI. Below the CMC, the copolymers predominantly exist as unimers rather than micelles; thus, no significant conversion of I_3^- to I_2 occurs, and the absorbance of the solution remains unchanged. Once micelles begin to form, I_3^- is transformed into I_2, which entrapped within the hydrophobic PPO core, resulting in a

marked increase in absorbance intensity. The CMC value was defined as the minimum concentration required for amphiphilic copolymers to spontaneously self-assemble into thermodynamically stable micellar structures. Above this threshold, hydrophobic segments aggregate to form a compact inner core, while hydrophilic chains bearing terminal –OH groups extend into the surrounding aqueous phase, generating a core–shell architecture, which enables efficient encapsulation of hydrophobic drug molecules within the core and contributes to the structural integrity of the nanocarrier system. A low CMC value reflects high thermodynamic stability of the assembled micelles, indicating strong intermolecular interactions within the hydrophobic domain. This property is crucial for maintaining micelle integrity under extreme dilution conditions, thereby reducing premature disassembly and improving the likelihood of successful drug delivery to the target site. Herein, we investigated the ability of nanogels to self-assemble and aggregate into micellar structures in aqueous solution by iodine method as previously reported [11]. In this study, the self-assembly behavior of the nanogels in aqueous solution was evaluated using the iodine probe method. As summarized in **Table 3.1**, the amphiphilic Fud-P403 copolymers exhibited CMC values ranging from 86.67 to 240.21 ppm. Notably, increasing the degree of P403 conjugation resulted in decreasing in CMC value that attribute to the higher proportion of PPO segments within the copolymers structure. The extended PPO chains enhance the overall hydrophobic character of the copolymers, leading to a reduction in HLB and consequently lowering the CMC value. Therefore, Fud-P403 (1:9 wt/wt) was selected for subsequent further FA conjugation, drug encapsulation and other evaluation, underscoring its promise as a potent and biocompatible nanocarrier for combination cancer therapy

After FA conjugation, the CMC of FA-Fud-P403 was determined to be 74.34 μg/mL, which is markedly lower than that of the parent Fud-P403 copolymers, indicating a significantly enhanced self-assembly tendency. This reduction in CMC can be directly correlated with the introduction of FA, in which aromatic ring and relatively hydrophobic structure increases the overall hydrophobic character of the FA-Fud-P403 copolymers [151]. FA not only contribute hydrophobicity but may also promote additional intermolecular interactions, such as π–π stacking between aromatic rings, which further stabilize the assembled micellar structure. These cooperative interactions strengthen the core-forming tendency of the PPO segments and enhance

the cohesion of the hydrophobic domain, enabling micellization to occur at significantly lower polymer concentrations. The reduction in CMC is particularly important in the context of biological applications. Upon systemic administration, nanocarriers are dilution in the bloodstream, which can destabilize micellar systems with relatively high CMC values, leading to premature disassembly and drug leakage. The lower CMC of FA-Fud-P403 ensures that the nanogels remain structurally intact even under highly diluted physiological conditions, thereby preserving their drug-loading capacity and preventing faster release acceleration of encapsulated agents. Moreover, the enhanced stability of the micellar core directly contributes to improved solubilization of hydrophobic drugs, as the strengthened hydrophobic environment provides a more favorable reservoir for drug retention. At the same time, the stable core–shell architecture supports controlled and sustained drug release profiles, which are essential for maintaining therapeutic drug levels over extended periods. Overall, the decrease in CMC following FA conjugation reflects a critical improvement in the self-assembly behavior and physicochemical stability of the nanogels system, enhancing stability under physiological dilution conditions that not only ensures efficient drug encapsulation and retention but also supports prolonged systemic circulation and improved bioavailability at target sites. Such properties are essential for maximizing therapeutic efficacy and underscore the advantage of incorporating FA as both a targeting ligand and a structural modulator in advanced drug delivery platforms.

Table 3.1. The CMC value of Fud-P403 and FA-Fud-P403 nanogels

Sample (wt/wt)	CMC value (ppm)
Fud-P403 (1:3)	240.21 ± 1.76
Fud-P403 (1:6)	218.53 ± 3.76
Fud-P403 (1:9)	186.67 ± 2.65
Fud-P403 (1:12)	206.21 ± 1.85
FA-Fud-P403	74.34 ± 5.324

3.1.2.2. Size distribution and zeta potenial of nanogels

According to the DLS analysis **(Table 3.2)**, the physicochemical characteristics of Fud-P403 nanogels were strongly dependent on the grafting ratio between Fud and P403, indicating that the self-assembly behavior of the copolymers system is governed by a delicate hydrophilic–hydrophobic balance. As the grafting ratio increased from 1:3 to 1:9, the hydrodynamic diameter significantly decreased from 503.19 ± 185.93 nm to 241.08 ± 6.12 nm. Importantly, the size reduction can be mechanistically attributed to strengthened hydrophobic interactions among the PPO segments of P403. The increased PPO content enhances core-forming hydrophobic interactions driven by entropy gain from water molecule release, thereby promoting tighter micellar packing and thermodynamically more stable nanostructures. The lowest PDI value (0.29 ± 0.249) observed at the 1:9 grafting ratio further confirms the formation of a relatively homogeneous nanoparticle population, suggesting that this composition approaches an optimal amphiphilic equilibrium. However, further increasing the grafting ratio to 1:12 resulted in a marked enlargement of particle size (518.17 ± 71.24 nm) and a broader distribution (PDI = 0.52 ± 0.192). This phenomenon likely arises from excessive hydrophobic domain incorporation, which disturbs the hydrophilic–hydrophobic balance and promotes interparticle aggregation rather than controlled intramolecular self-assembly. Steric congestion along the polymer backbone may also hinder proper micellar compaction, favoring intermolecular association and thus increasing particle size.

The surface charge characteristics further elucidate the physicochemical stability and structural evolution of the nanogels system. Fud-P403 nanogels exhibit negative zeta potentials in the range of −17.70 to −24.25 mV, which can be primarily attributed to the abundant sulfate ($-SO_3^-$) groups present on the Fud backbone. These negatively charged functionalities generate electrostatic repulsion between particles, thereby contributing to colloidal stabilization and preventing premature aggregation in aqueous environments. Specifically, the FA-Fud-P403 nanogels display a significantly reduced hydrodynamic diameter of 115.1 ± 6.00 nm, suggesting that FA conjugation induces structural compaction rather than expansion. This behavior can be mechanistically rationalized by considering the physicochemical nature of FA. The presence of aromatic rings and relatively hydrophobic domains within the FA structure promotes additional intramolecular interactions, including hydrophobic association

and potential π–π stacking between adjacent FA moieties that effectively reduce chain mobility at the nanogels, leading to contraction of the shell layer and formation of a more compact and tightly organized core–shell structure [147]. FA conjugation leads to a substantial increase electronegativity in the zeta potential, shifting from approximately -20.05 ± 1.021 mV to -38.6 ± 1.2 mV that can be attributed to the incorporation of carboxylate ($-COO^-$) groups from FA, which act sulfate groups of Fud to increase overall surface electronegativity. The contribution from terminal PEO segments, which facilitate hydration and surface exposure of charged groups, may further amplify this effect. Importantly, the zeta potential exceeding 30 mV (in absolute terms) is widely recognized as a critical threshold for achieving strong electrostatic stabilization, as it provides sufficient repulsive force to counterbalance attractive interactions such as van der Waals forces [148], increasing in surface charge not only reinforces colloidal stability but also having important biological implications. A high negatively charged surface can reduce nonspecific protein adsorption and opsonization, thereby potentially prolonging systemic circulation and improving biodistribution. Moreover, the strong agreement between the enhanced zeta potential and the FA content determined by UV–Vis analysis provides evidence for the successful and efficient conjugation of FA onto the Fud-P403 framework. Taken together, the reduction in particle size, increase in surface charge and maintenance of a size distribution collectively indicate that FA conjugation does not merely introduce targeting functionality but actively modulates the self-assembly behavior of the nanogels system. The resulting nanostructure enhances stability, reflecting a synergistic interplay physical organization [149]. Application standpoint, the particle size of approximately 115 nm, with high colloidal stability is particularly favorable for systemic drug delivery. Nanocarriers within this size regime are well-suited to exploit the enhanced permeability and retention (EPR) effect, allowing efficient accumulation in tumor tissues while avoiding rapid renal clearance and minimizing uptake by the mononuclear phagocyte system [150]. Therefore, the optimized physicochemical properties of FA-Fud-P403 nanogels not only validate the effectiveness of the design strategy but also highlight their strong potential as a robust and multifunctional platform for targeted and combination anticancer therapy.

Table 3.2. The size distribution and Polydispersity Index (PDI) of Fud-P403 with various grafted ratio and FA-Fud-P403

Sample (wt/wt)	Diameter (nm)	PDI	Zeta potential (mV)
Fud-P403 (1:3)	503.19 ± 185.93	0.37 ± 0.168	-24.25 ± 1.485
Fud-P403 (1:6)	310.88 ± 10.48	0.41 ± 0.262	-22.70 ± 3.561
Fud-P403 (1:9)	241.08 ± 6.12	0.29 ± 0.249	-20.05 ± 1.021
Fud-P403 (1:12)	518.17 ± 71.24	0.52 ± 0.192	-18.40 ± 2.394
FA-Fud-P403	115.1 ± 6.00	0.42 ± 0.358	-38.6 ± 1.200

3.2. Characterization of FA-Fud-P403@Cur/Cis

3.2.1. Structural characterization of FA-Fud-P403@Cur/Cis

The co-encapsulation of Cur and Cis within FA-Fud-P403 nanogels is primarily driven by a combination of hydrophobic and electrostatic interactions, arising from the amphiphilic nature of the P403-based system and the distinct physicochemical properties of the two drugs. The hydrophobic PPO segments self-assemble into a core that favors the incorporation of hydrophobic compounds, while the surrounding hydrated PEO shell and interfacial regions offer a more polar microenvironment suitable for hydrophilic or partially charged species [146]. Cur, a highly hydrophobic polyphenol with an extended conjugated aromatic structure, is preferentially localized within the PPO core, supported by UV–Vis spectroscopy, where the dual drug-loaded nanogels display a characteristic absorption peak at 426 nm **(Figure 3.10)**, corresponding to the π–π^* transition of the diketone group of Cur [152]. In addition, FT-IR analysis shows absorption bands at 1516–1509 cm^{-1} attributed to C=O and C=C stretching vibrations of Cur, along with a shift in the C=C stretching band from 1653 cm^{-1} to 1639 cm^{-1} upon encapsulation **(Figure 3.11)**. These spectral changes indicate strong intermolecular interactions and confirm the confinement of Cur within the hydrophobic nanogels core

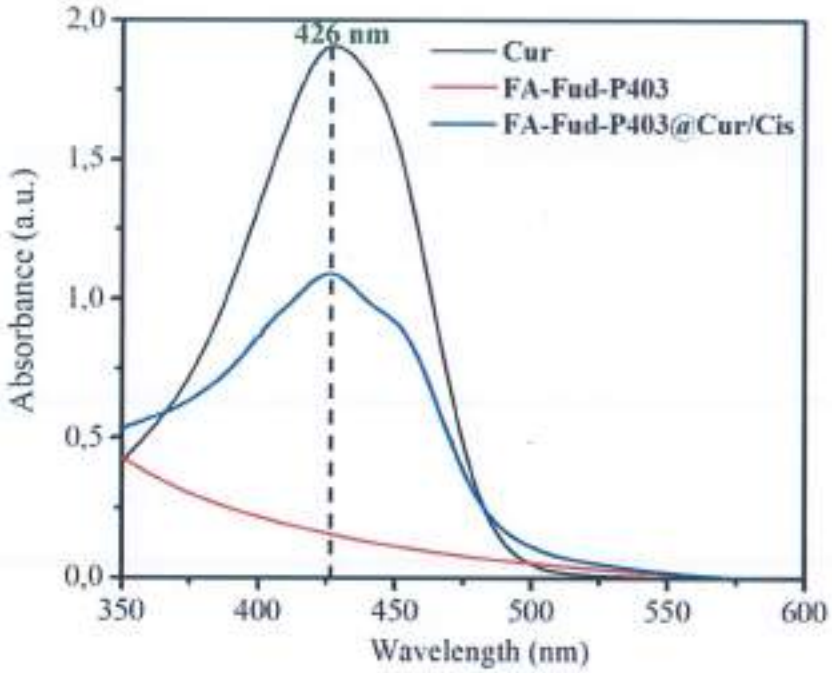

Figure 3.10. The UV-Vis result of Cur, FA-Fud-P403, and FA-Fud-P403@Cur/Cis

Meanwhile, Cis is a polar platinum complex that is primarily driven by electrostatic interactions and coordination bonds in aqueous solution between Pt of Cis and sulfate groups (-OSO_3-) of the Fud chains that is mainly localized on the surface or the hydrophilic shell of the nanogels system [153], evidenced by the emergence of FT-IR absorption bands in the range of 3200–3000 cm^{-1}, corresponding to N–H stretching vibrations of Cis in FA-Fud-P403@Cur/Cis nanogels [154] **(Figure 3.10)** that confirms the successful co-encapsulation of Cur and Cis within the FA-Fud-P403 nanogels through a spatially differentiated loading mechanism, wherein Cur is predominantly confined within the hydrophobic PPO core, while Cis is associated with the interfacial or shell regions via hydrophobic and electrostatic interactions [46,155] which not only enhances drug-loading stability but also mitigates premature Cis hydrolysis while preserving Cur in a protected hydrophobic microenvironment, thereby controlled release behavior.

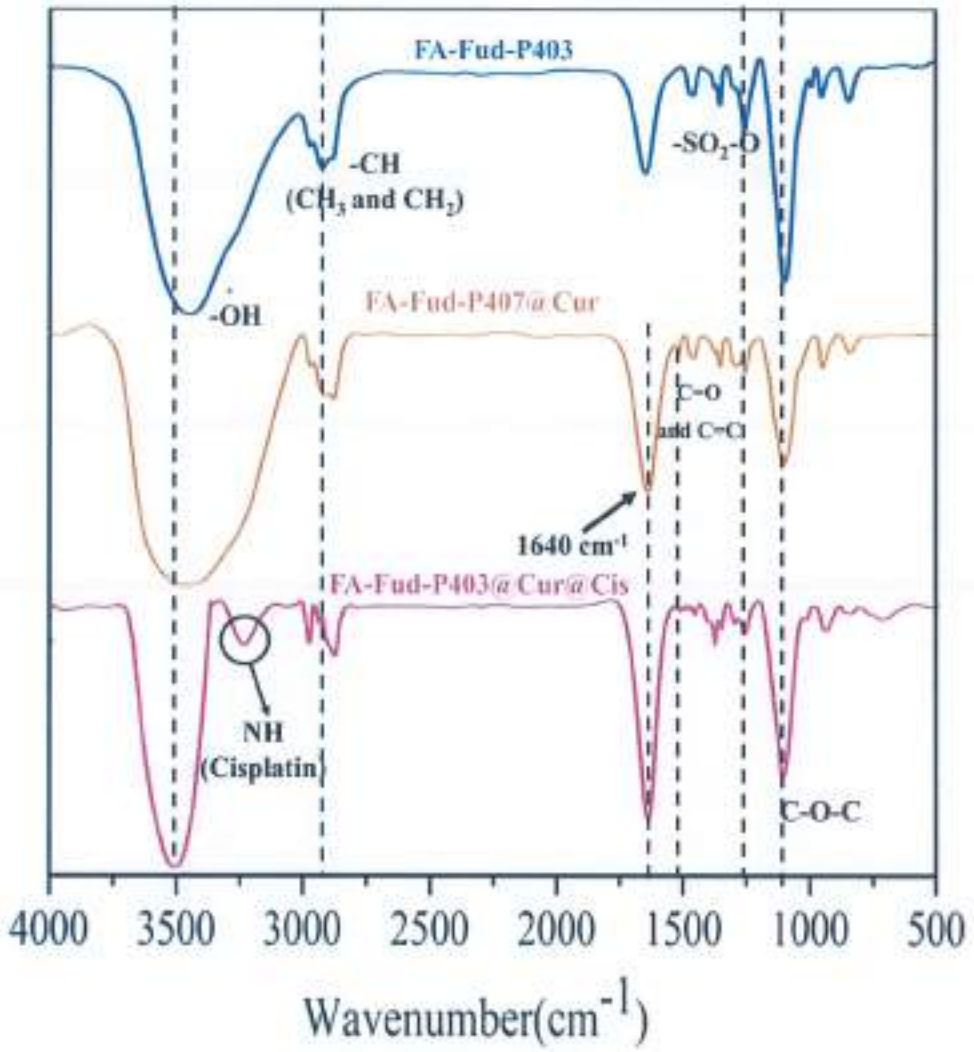

Figure 3.11. The FT-IR results of FA-Fud-P403, FA-Fud-P403@Cur, and FA-Fud-P403@Cur/Cis

3.2.2. Entrapment efficiency and morphological properties of FA-Fud-P403 nanogels

The co-encapsulation behavior of Cur and Cis within the nanogels is intrinsically governed by the structural characteristics of the FA-Fud-P403 carrier, particularly the length of the PPO core. The drug-loading study clearly demonstrates that the extended PPO segment of P403 (70 units) plays a decisive role in enhancing drug accommodation through intensified hydrophobic interactions and electrostatic attractions with the encapsulated agents. As shown in **Figure 3.12A**, FA-Fud-P403 achieved remarkably high entrapment efficiencies of 95.72% for Cur and 68.34% for Cis, underscoring the importance of hydrophobic domain engineering in nanogels design. Mechanistically, the enlarged PPO core provides a stable microenvironment

that favors the partitioning of hydrophobic drug molecules explaining to strong affinity of Cur toward the PPO core compared to Cis that is further reinforced by extensive intermolecular hydrogen bonding between the methoxyl and hydroxyl groups on Cur's aromatic rings and the functional groups of the FA-Fud-P403 nanogels, as well as interactions involving Cur's aliphatic carbonyl chain [156]. These findings collectively highlight the structure–interaction–loading relationship that governs the differential encapsulation behavior of the two drugs.

Importantly, the excellent colloidal stability observed is relatively high absolute zeta potential values reported in **Figure 3.12B**, further confirming the physicochemical robustness of the FA-Fud-P403 nanogels system. Afrer the co-loading of Cur and Cis, the zeta potential exhibited a slight decrease from −38.6 ± 1.2 mV to −33.9 ± 2.4 mV, attributing to the partial surface localization of Cis, which carries positively charged species under physiological conditions. The presence of negatively charged sulfate groups of Fud leads to a reduction in surface electronegativity. Nevertheless, despite this decrease, the absolute zeta potential remains well within the range of ±30–60 mV, which is widely recognized as a threshold for maintaining strong electrostatic repulsion between colloidal particles [146]. Such repulsive interactions effectively prevent aggregation, preserving nanoscale dispersion over extended periods reduce nonspecific serum protein adsorption, and minimize opsonization, thereby enhancing dispersion stability in biological environments [157]. In addition, a high surface charge contributes to reducing nonspecific protein adsorption and limiting opsonization processes in biological environments, which are critical factors influencing nanoparticle clearance and biodistribution. Consequently, the maintained zeta potential values strongly support the observed long-term colloidal stability and suggest favorable behavior under physiological conditions [158]. Upon co-encapsulation of Cur and Cis, the hydrodynamic diameter showed only a marginal increase, with FA-Fud-P403@Cur/Cis exhibiting an average size of 138.8 ± 3.68 nm as determined by **Figure 3.12C.** This slight enlargement reflects the successful incorporation of drugs into the nanogels core without inducing structural disruption or aggregation. The preservation of size distribution which is essential for reproducible biological performance. In contrast, TEM images **(Figure 3.12D)** reveal spherical nanogels with a significantly smaller average diameter of approximately 71.2 ± 1.17 nm. The difference between

DLS and TEM measurements explained by measurement conditions. DLS determines the hydrodynamic diameter of particles in a fully hydrated and swollen state, including the solvation layer and polymer chain extension in aqueous media. Conversely, TEM analysis is conducted under dry conditions, where solvent removal leads to contraction of the polymer network, resulting in smaller observed particle sizes. The particle size of ~140 nm falls within the optimal range for passive tumor targeting via the enhanced permeability and retention (EPR) effect. Nanoparticle size are suitable to avoid rapid renal clearance as well as efficiently extravasate through the leaky vasculature of tumor tissues while minimizing uptake by the mononuclear phagocyte system. This is critical for achieving prolonged systemic circulation and enhanced tumor accumulation [159]. Collectively, these results highlight that the structural design of FA-Fud-P403—particularly the incorporation of a hydrophobic PPO core and hydrophilic PEO shell—not only enables efficient co-encapsulation of both hydrophobic (Cur) and relatively hydrophilic (Cis) drugs, but also imparts excellent colloidal stability, controlled size distribution, and favorable surface properties. These physicochemical attributes are directly correlated with improved *in vivo* performance, underscoring the potential of this nanogels system as a highly effective platform for targeted and synergistic cancer therapy.

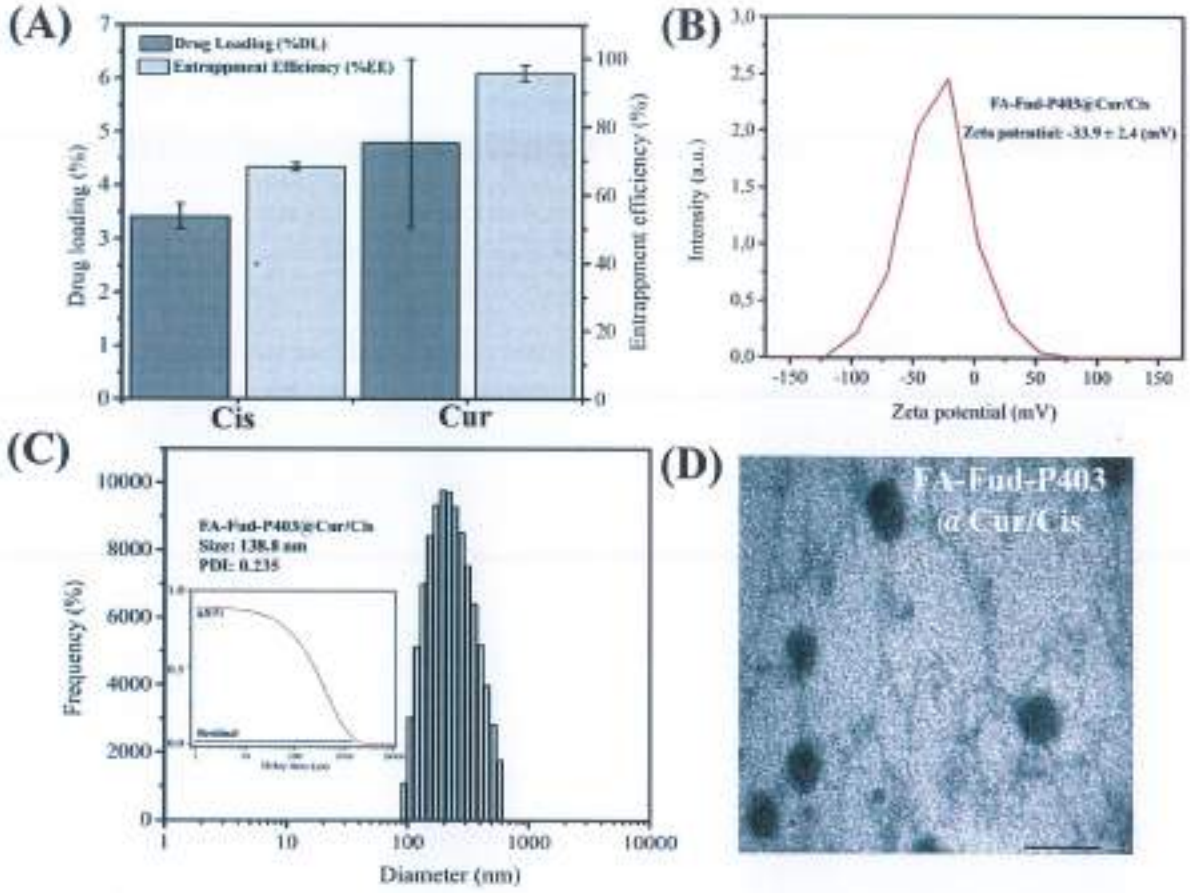

Figure 3.12. (A) The entrapped efficiency (EE%) and drug-loading (DL%). (B) Zeta potential, (C) Hydrodynamic sizes, and (D) TEM images (Scale bars = 100 nm) of drug loaded FA–Fud–P403 nanogels

3.3. Stability of drug-loaded nanogels

Nanogels systems are prone to colloidal instability in aqueous and biological environments, where interparticle interactions, ionic strength, and protein adsorption may induce aggregation, leading to increased particle size. Therefore, evaluation of colloidal stability under physiologically relevant conditions is essential to *in vivo* behavior. As depicted in **Figure 3.13**, the hydrodynamic diameter of FA-Fud-P403@Cur/Cis nanogels was monitored over 96 h in PBS (pH 7.4) and MEM medium. In both conditions, the nanogels exhibit only an increase in particle size, with all values consistently remaining below 200 nm throughout the study. This behavior confirms that the nanogels system maintains its colloidal integrity even in protein-containing media. The slight increase in particle size can be rationalized by dynamic interfacial phenomena rather than instability. In PBS, this effect is primarily associated with hydration layer expansion surrounding the hydrophilic PEO corona. In MEM,

additional contributions from protein corona formation are expected, arising from nonspecific adsorption of biomolecules onto the nanogels surface. Importantly, these processes remain controlled and reversible, as evidenced by the absence of uncontrolled particle growth. Mechanistically, the excellent stability of the system can be attributed to synergistic steric and electrostatic stabilization. The PEO chains provide a dense hydration shell that generates steric repulsion, while the negatively charged sulfate groups of Fud introduce electrostatic barriers that prevent particle–particle contact. This dual stabilization mechanism effectively suppresses aggregation even under conditions of high ionic strength and biological complexity. Maintaining particle sizes below 200 nm is critically important for exploiting the enhanced permeability and retention (EPR) effect, enabling preferential accumulation in tumor tissues while avoiding rapid renal clearance (<10 nm) and minimizing opsonization and uptake by the mononuclear phagocyte system [159]. Consequently, such size stability contributes to prolonged circulation time and improved tumor targeting efficiency. Collectively, the minimal size variation and sustained nanoscale dimensions over 96 h demonstrate that FA-Fud-P403@Cur/Cis nanogels possess robust colloidal stability under physiological conditions. This property is fundamental for ensuring reproducible *in vivo* performance and highlights the suitability of this system as a reliable platform for targeted drug delivery.

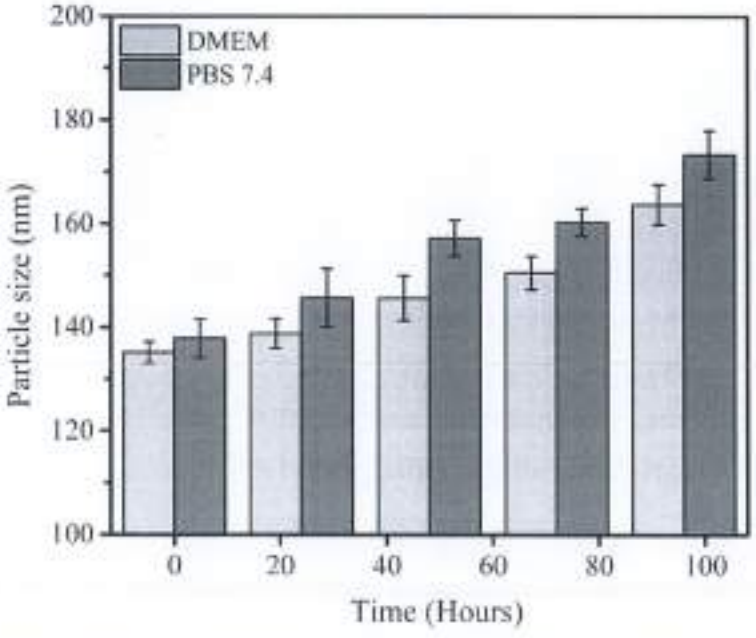

Figure 3.13. The colloidal stability of FA-Fud-P403@Cur/Cis nanogels in PBS and DMEM media by DLS

The enhanced stability of Cur upon encapsulation within FA-Fud-P403 nanogels highlights the critical role of the polymeric microenvironment in protecting labile hydrophobic drugs under physiological conditions [160]. As demonstrated in **Figure 3.14**, free Cur underwent rapid degradation in both PBS (pH 7.4) and MEM media, with its remaining content dropping dramatically to approximately 20% within 48 h. This pronounced instability is consistent with the intrinsic chemical susceptibility of Cur, which readily undergoes hydrolytic degradation, oxidative transformation, and structural breakdown in aqueous environments, particularly under neutral or slightly alkaline conditions [156]. In contrast, Cur encapsulated in FA-Fud-P403@Cur/Cis nanogels retained more than 80% of its initial content even after 96 h of incubation. Such a substantial improvement cannot be attributed solely to physical entrapment but rather reflects a synergistic stabilization mechanism arising from the amphiphilic nanogels architecture. Firstly, the hydrophobic domains formed by the P403 segments create a compact core region that serves as a thermodynamically favorable reservoir for Cur. Strong hydrophobic interactions between Cur and the polymer chains reduce drug diffusion into the surrounding aqueous medium, thereby limiting direct exposure to water molecules and dissolved oxygen—two primary drivers of Cur degradation [161]. These hydrophobic regions effectively suppress hydrolysis and oxidative cleavage pathways. Secondly, the nanogels network likely restricts molecular mobility within the core, generating a confined microenvironment that slows chemical transformation kinetics. The reduced diffusion rate of reactive species into the core further contributes to stabilization. In this context, the nanogels acts not merely as a carrier but as a protective nanoreactor that modulates the local chemical environment of Cur. Interestingly, the stability of Cur in MEM medium was comparable to that observed in PBS, suggesting that the nanogels structure effectively resists serum-associated destabilization mechanisms. This indicates that protein–nanogels interactions do not significantly disrupt the hydrophobic core or accelerate drug diffusion, reflecting structural cohesion of the FA-Fud-P403 network. Overall, the FA-Fud-P403@Cur/Cis nanogels demonstrate excellent colloidal stability and strong drug-protective capability under physiological and serum-mimicking conditions, supporting their suitability for systemic anticancer drug delivery.

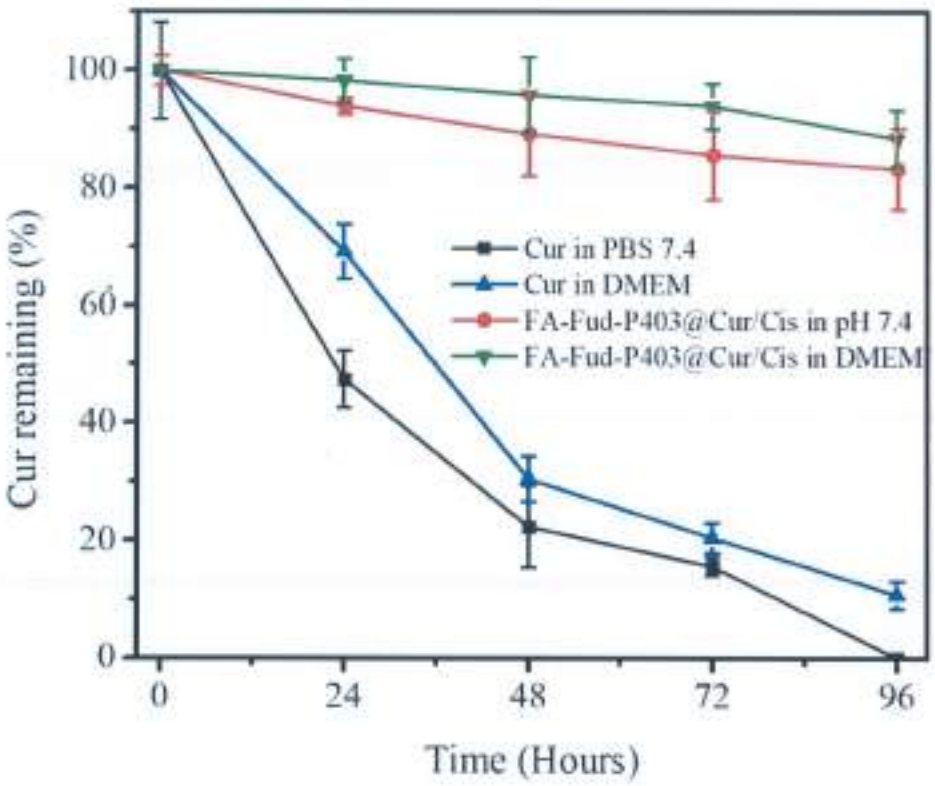

Figure 3.14. The chemical stability of free Cur and Cur-loaded FA-Fud-P403 nanogels in PBS and DMEM media for 96 hours

3.4. *In vitro* drug-released profiles and release kinetics of drugs from nanogels

3.4.1. *In vitro* drug-released profiles

The controlled and sustained release behavior of Cis/Cur from FA-Fud-P403 nanogels plays a pivotal role in optimizing therapeutic efficacy while minimizing systemic toxicity. By maintaining drug concentrations within the therapeutic window over extended periods, such systems reduce the high dosing frequency and limit off-target exposure to healthy tissues [137]. In this study, *in vitro* release studies were systematically conducted under two physiologically relevant pH conditions (pH 7.4 and pH 5.5), which mimick the normal physiological environment and the mildly acidic tumor microenvironment, respectively [13]. As illustrated in **Figure 3.15**, the free drug forms of Cis and Cur exhibited a rapid release profile, characterized by an initial burst release and complete diffusion within 24 h at both pH conditions. This behavior reflects the absence of any diffusion barrier or retention mechanism, leading to uncontrolled drug availability and potential systemic toxicity. In contrast, the FA-Fud-P403@Cur/Cis nanogels system displayed a markedly sustained and controlled release during extented 96 h period, demonstrating the effective encapsulation and

retention capability of the nanocarrier. At pH 5.5, the release profiles showed a significantly enhanced drug release, with approximately 75.6% of Cis and 60.79% of Cur released over the studied period. This accelerated release under acidic conditions can be attributed to protonation of functional groups within the nanogels matrix, including amine and sulfate moieties. Such protonation weakens electrostatic interactions and disrupts hydrogen bonding within the polymeric network, leading to partial swelling or destabilization of the nanogels structure [161]. Consequently, the micellar core–shell architecture facilitates faster diffusion of the encapsulated drugs into the surrounding medium. In contrast, at physiological enviroment (pH 7.4), the nanogels system exhibited a substantially slower release profile, with only 46.41–55.62% of Cis and 38.17–45.16% of Cur released over the same duration. Under these conditions, the polymer network remains relatively stable, supported by stronger intermolecular interactions micellar structure. This stability effectively restricts premature drug leakage during systemic circulation, thereby enhancing drug retention and improving *in vivo* safety. Notably, the release rate of Cis was consistently higher than that of Cur under both pH conditions. This difference can be rationalized by considering the distinct physicochemical properties and interaction mechanisms of the two drugs within the nanogels core. Cis, being relatively more hydrophilic and less strongly associated with the hydrophobic domains of the micelle, is more readily released upon structural relaxation. In contrast, Cur exhibits strong hydrophobic interactions with the PPO core, resulting in greater encapsulation and slower diffusion kinetics [162]. These differential release behaviors further support the role of hydrophobic interactions as a key factor governing the pH-responsive release characteristics of the nanogels system. Overall, the FA-Fud-P403 nanogels demonstrate a well-defined pH-dependent release profile, characterized by enhanced drug release under acidic conditions and sustained retention at physiological pH. This dual behavior is highly desirable for targeted cancer therapy, as it enables preferential drug release at tumor sites while minimizing premature leakage in the bloodstream. Such controlled and stimuli-responsive release properties not only improve therapeutic efficiency but also contribute to reducing systemic side effects, thereby highlighting the potential of this nanoplatform as an effective and intelligent drug delivery system.

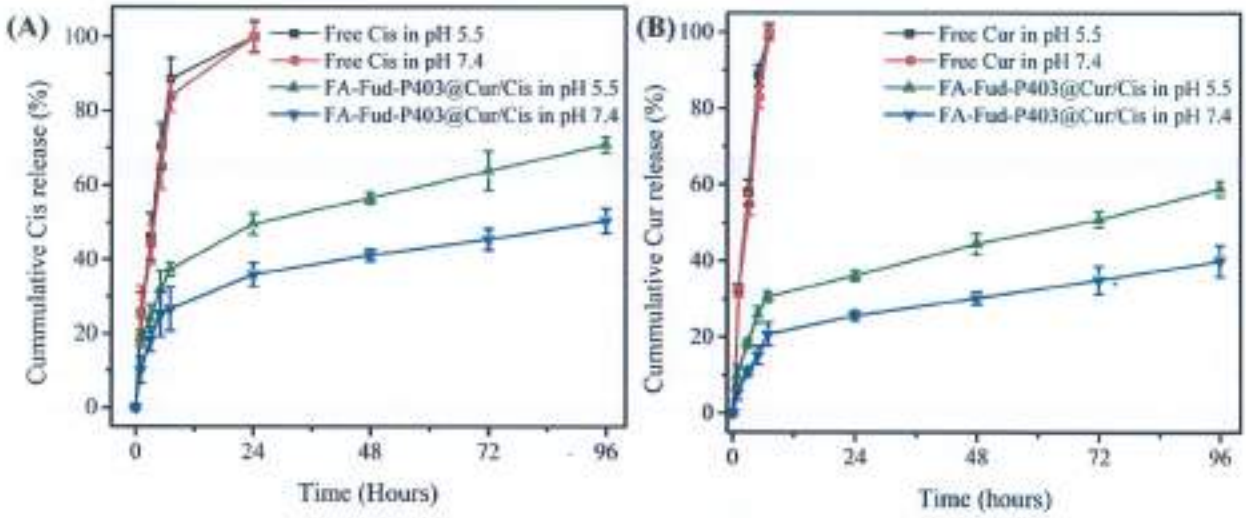

Figure 3.15. The in vitro pH-responsive release profiles of (A) Cur and (B) Cis in the forms of free and FA-Fud-P403 nanoformulations

3.4.2. Release kinetics of drugs from nanogels

The *in vitro* drug release behavior of FA-Fud-P403 nanogels was systematically investigated under both acidic (pH 5.5) and physiological (pH 7.4) conditions to elucidate the underlying release mechanism and its correlation with nanogels structure. As summarized in **Tables 3.3–3.4**, kinetic fitting analysis revealed that the release profiles of both Cis and Cur were predominantly diffusion-controlled. Among the evaluated mathematical models, the Korsmeyer–Peppas model provided the best description of the experimental data, as evidenced by the greatest correlation coefficients (R^2) compared to other mathematical models, ranging from 0.9674 to 0.9927 for Cis and from 0.9548 to 0.9919 for Cur. Notably, the release exponent (n) values for both drugs were ranged from 0.26 to 0.36, indicating that drug release from the FA-Fud-P403 nanogels follows a predominantly Fickian diffusion mechanism. This observation suggests that the release process is governed primarily by concentration-gradient-driven diffusion through the nanogels matrix rather than polymer chain relaxation or matrix erosion. Although the release mechanism is diffusion-dominated, the dissolution behavior of the encapsulated drugs differed markedly from that of their free counterparts. Free Cis and Cur exhibited rapid dissolution, as reflected by short MDT value of 4.822–5.303 h for Cis and 4.116–4.576 h for Cur. In contrast, co-encapsulation within FA-Fud-P403 nanogels resulted in a dramatic prolongation of MDT, reaching 83.981–268.577 h for Cis and 129.1109–341.0759 h for Cur, depending on the pH condition **(Table 3.5-3.6)**. This pronounced

increase in MDT demonstrates that, despite following Fickian diffusion, drug transport within the nanogels is substantially hindered. The extended MDT can be directly attributed to the structural characteristics of the FA-Fud-P403 carrier, particularly the presence of highly hydrophobic PPO core. The hydrophobic PPO domains provide a stable microenvironment that enhances drug–polymer interactions, increases diffusion pathways, and effectively restricts molecular mobility within the nanogels matrix. This effect is especially pronounced for Cur, whose hydrophobic aromatic structure favors stronger interaction into the PPO core, resulting in slower diffusion and more sustained release compared to the relatively more hydrophilic Cis. Collectively, these findings demonstrate that the rational design of the FA-Fud-P403 nanogels enables precise control drug release behavior by combining diffusion-dominated kinetics with strong hydrophobic retention. By effectively suppressing burst release and prolonging drug residence time, this nanogels system enhances the sustained release and bioavailability of both Cis and Cur. Such controlled release characteristics are highly desirable for cancer therapy, as they are expected to maintain therapeutic drug concentrations over extended periods, reduce systemic toxicity, and ultimately improve antitumor efficacy.

Table 3.1. The compatibility of Cis released in four kinetic modes

Cis Formulation	pH	The mathematical models of Cis-released kinetics								
		Zero order		First order		Higuchi		Korsmeyer-Peppas		
		K_0	R^2	K_1	R^2	K_h	R^2	K_n	n	R^2
Cis	5.5	0.03	0.83	-0.32	0.95	0.14	0.96	0.38	0.34	0.97
FA-Fud-P403@Cur/Cis	5.5	0.01	0.84	-0.01	0.92	0.06	0.97	0.22	0.27	0.99
Cis	7.4	0.03	0.70	-0.26	0.96	0.19	0.84	0.34	0.36	0.99
FA-Fud-P403@Cur/Cis	7.4	0.01	0.88	-0.01	0.95	0.04	0.98	0.15	0.27	0.98

Table 3.2. The compatibility of Cur released in four kinetic modes

Cur Formulation	pH	The mathematical models of Cis-released kinetics								
		Zero order		First order		Higuchi		Zero order		
		K_0	R^2	K_1	R^2	K_h	R^2	K_n	n	R^2

Cur	5.5	0.02	0.59	-0.45	0.93	0.12	0.81	0.46	0.27	0.96
FA-Fud-P403@Cur/Cis	5.5	0.01	0.88	-0.01	0.94	0.05	0.95	0.14	0.32	0.98
Cur	7.4	0.03	0.68	-0.34	0.95	0.20	0.85	0.42	0.29	0.97
FA-Fud-P403@Cur/Cis	7.4	0.01	0.87	-0.01	0.91	0.04	0.93	0.09	0.35	0.98

Table 3.3. The dissolution parameter of Cis release from the FA-Fud-P403@Cur/Cis

Cis formulation	pH	Order of release	$t_{25\%}$ (hours)	$t_{50\%}$ (hours)	$t_{75\%}$ (hours)	$t_{90\%}$ (hours)	MDT (hours)
Free Cis	5.5	Fickian	0.308	2.430	8.142	14.023	4.822
FA-Fud-P403@Cur/Cis	5.5	Fickian	2.196	29.605	135.597	268.797	83.981
Free Cis	7.4	Fickian	0.410	2.878	9.001	15.031	5.303
FA-Fud-P403@Cur/Cis	7.4	Fickian	7.468	97.100	435.383	854.857	268.577

Table 3.4. The dissolution parameter of Cur release from the FA-Fud-P403@Cur/Cis

Cur formulation	pH	Order of release	$t_{25\%}$ (hours)	$t_{50\%}$ (hours)	$t_{75\%}$ (hours)	$t_{90\%}$ (hours)	MDT (hours)
Free Cur	5.5	Fickian	0.1122	1.4762	6.6643	13.1251	4.1162
FA-Fud-P403@Cur/Cis	5.5	Fickian	6.5757	59.5668	216.1966	386.0013	129.1109
Free Cur	7.4	Fickian	0.1651	1.8390	7.5336	14.2032	4.5756
FA-Fud-P403@Cur/Cis	7.4	Fickian	23.2563	176.4075	577.1255	983.4094	341.0759

3.5. *In vitro* hemolysis assay

Hemocompatibility is a fundamental requirement for nanocarriers designed for intravenous administration, as it reflects their potential to interact safely with red blood cells (RBCs) in circulation. In this context, the hemolysis assay serves as a reliable indicator of membrane integrity and cytotoxic effects induced by the tested materials.

As shown on **Figure 3.16**, the hemolysis rate reveal that free Cur and Cis induced noticeable hemolysis at concentrations ranging from 25 to 100 ppm, with values exceeding the 5% threshold, suggesting significant disruption of erythrocyte membranes. In contrast, nanogels incorporating both drugs (FA–Fud–P403@Cur/Cis) exhibited markedly reduced hemolytic activity, with all measured values remaining below 5%, thereby meeting the criteria for non-hemolytic materials [164]. This reduced toxicity can be explained by the nano-architectural design of the carrier. The hydrophobic PPO domains act as a effectively shielding them from direct contact with RBC membranes. Taken together, these observations indicate that encapsulation within the FA–Fud–P403 nanogels matrix significantly improves blood compatibility while preserving drug functionality. Such a balance between safety and performance highlights the suitability of this system as a promising platform for systemic drug delivery, particularly in anticancer applications where minimizing off-target toxicity is essential

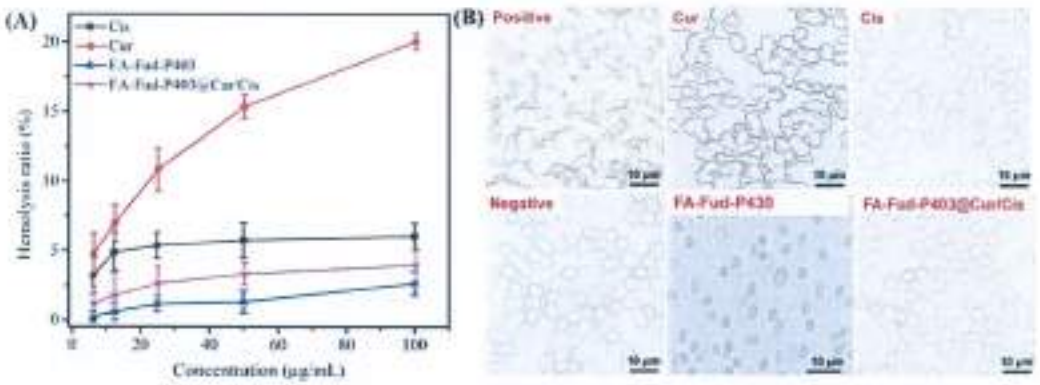

Figure 3.16. (A) The hemolysis rate after treatment with free Cur/Cis and FA-Fud-P403@Cur/Cis nanogels at various concentrations and (B) the images of erythrocytes after treament with free Cur/Cis and FA-Fud-P403@Cur/Cis nanogels at 100 ppm

3.6. *In vitro* cytotoxic assay

3.6.1. The cytotoxicity of nanogels on various cell lines

The biological safety and tumor-selective response of FA–Fud–P403 nanogels were investigated through a series of in vitro evaluations using both normal and cancerous cell models. Human dermal fibroblasts (HDF) were selected to represent healthy cells, while MCF-7 breast cancer cells were used to assess anticancer activity. Cell viability and membrane integrity were examined via WST-1 and Live/Dead assays, respectively. The results shown on **Figure 3.17A** indicate that FA–Fud–P403

nanogels exert minimal toxicity toward HDF cells, with viability remaining above 80% even at 125 ppm. This outcome demonstrates that the material satisfies commonly accepted cytocompatibility benchmarks outlined in ISO 10993 guidelines and regulatory frameworks recognized by the FDA [146]. In contrast, a markedly different response was observed in MCF-7 cells. Exposure to the FA-Fud-P403 nanogels formulation resulted in a significant cytotoxicity on MCF-7 cell line, with the decrease to 58.07% in cell viability, suggesting a preferential inhibitory effect on cancer cells. This selective behavior is likely governed by the specific recognition of FA onto nanogels folate receptor. In addition, physicochemical properties of the P403 segment, particularly its hydrophobic PPO chains of P403 also cause to reduce cell viability of cancer cell line by enhancing interactions with lipid membranes and intracellular structures, thereby disrupting mitochondrial function and limiting ATP generation, which is essential for rapid cancer cell proliferation. Furthermore, the P403 component has been reported to interfere with the function of P-glycoprotein, a membrane transporter responsible for drug efflux in resistant cancer cells. By modulating this pathway, the nanogels may promote higher intracellular retention of therapeutic agents, thereby enhanced their anticancer efficacy. The Live/Dead staining results **(Figure 3.17B)** further support these findings. HDF cells predominantly exhibited green fluorescence, confirming high viability, whereas MCF-7 cells showed a significant increase in red fluorescence, indicative of cell death. Overall, these observations highlight that FA–Fud–P403 nanogels combine good compatibility with normal cells and a distinct cytotoxic effect against cancer cells, underscoring their promise as a targeted nanocarrier system.

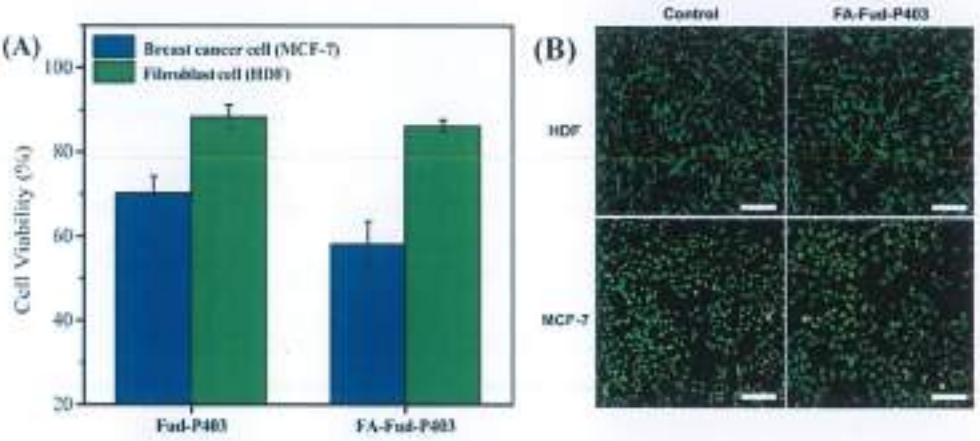

Figure 3.17. The in vitro cytotoxicity profiles of FA–Fud–P403 nanogels toward normal cells (HDF) and cancer cells (MCF-7). (A) Cell viability assessed by WST-

l assay. (B) Live/Dead staining (calcein-AM/PI) after 24 h incubation with bare nanogels (125 ppm)

Meanwhile, after drug loading, a notable difference in cytotoxicity was observed between FA-Fud-P403 depending on the single and dual-drug nanoformulation. As illustrated in **Figure 3.18A**, the Cis-loaded formulation (FA–Fud–P403@Cis) induced pronounced toxicity in HDF cells across the all tested concentration (6.25–100 ppm), suggesting a relatively rapid release of the drug and limited control over its distribution. In contrast, the co-loaded system (FA–Fud–P403@Cur/Cis) exhibited a more favorable cytocompatibility profile toward normal cells. This improvement can be associated with enhanced stabilization of the payloads within the hydrophobic P403 core, which restricts premature drug diffusion and promotes a more sustained release behavior. Such controlled release reduces acute exposure of healthy cells to cytotoxic concentrations that further refinement is still required to optimize selectivity.

From a therapeutic standpoint, the co-delivery strategy offers a means to overcome the inherent drawbacks of Cis and Cur, including poor pharmacokinetics, limited tumor selectivity, and systemic side effects. The anticancer performance of these nanoformulations was evaluated in MCF-7 cells **(Figure 3.18B)**. Notably, the dual drug-loaded nanogels demonstrated significantly greater suppression of cancer cell proliferation compared to the single-drug system across all tested concentrations. This enhanced efficacy can be rationalized by synergistic mechanisms at the cellular level. The nanogels platform is capable of modulating ATP-dependent drug efflux transporters, such as P-gp, MRP1, and BCRP, which are typically responsible for reducing intracellular drug accumulation. Their inhibition leads to increased retention of Cis within cancer cells, thereby amplifying its cytotoxic effect. Cur acts through multiple complementary pathways: it downregulates HER2-associated signaling, suppresses NF-κB-mediated inflammatory responses, and interferes with cell cycle progression. In particular, Cur induces G1 phase arrest via cyclin D1 suppression, which limits proliferative capacity and enhances cellular sensitivity to chemotherapeutic stress [166]. Overall, the integration of controlled drug release and multi-target biological activity results in a pronounced inhibition of tumor cell growth while partially mitigating toxicity toward normal cells. These findings highlight the potential of FA–Fud–P403 nanogels as an effective co-delivery platform for

combination chemotherapy, capable of improving therapeutic outcomes through both physicochemical and biological synergisms.

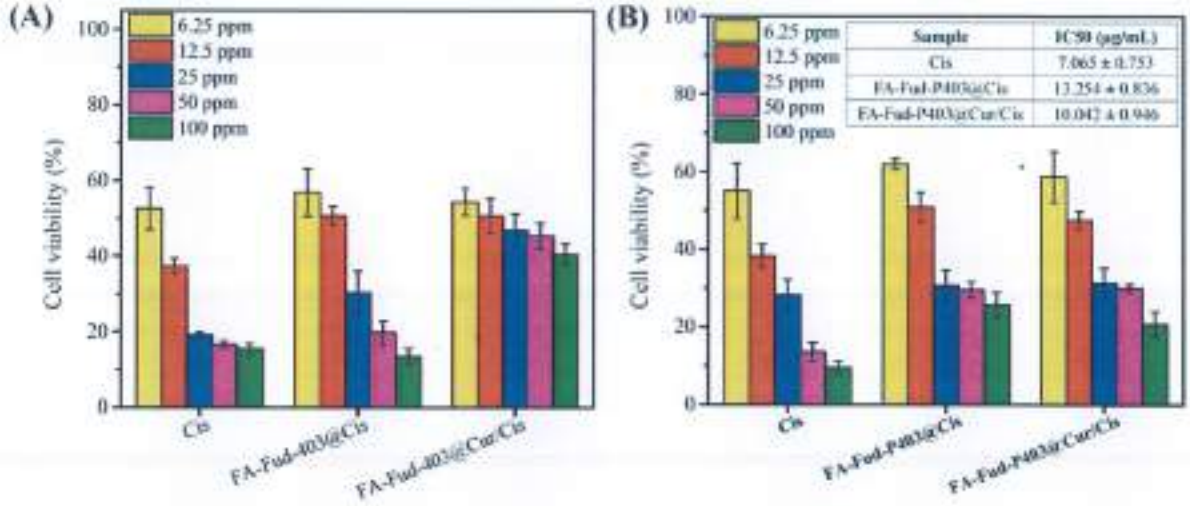

Figure 3.18. The in vitro cytotoxicity profiles of bare and dual drug-loaded FA–Fud–P403 nanogels toward normal cells (HDF) and cancer cells (MCF-7). The quantitative cytotoxicity assay of (A) L929 and (B) MCF-7 after co-incubation with different drug-loaded nanoformulations at varied concentrations

3.6.2. The cellular uptake assay

Cellular internalization is a critical prerequisite for evaluating the active targeting efficiency of nanogels-based drug delivery systems toward cancer cells. In this study, Rhodamine B (RhB) was employed as a fluorescent probe to monitor intracellular uptake, and the internalization behavior of FA-Fud-P403 nanogels in MCF-7 cells was examined using CLSM. As illustrated on **Figure 3.19**, cells treated with FA-Fud-P403 nanogels exhibited only blue fluorescence corresponding to DAPI-stained nuclei, with no detectable red fluorescence signal. This observation indicates negligible nonspecific cellular uptake in the absence of the fluorescent probe. In contrast, cells incubated with RhB-loaded FA-Fud-P403 nanogels displayed intense red fluorescence predominantly localized within the cytoplasm and accumulated around the perinuclear region after 4 h of incubation, primarily localized in the cytoplasm, with noticeable accumulation around the perinuclear region. The pronounced intracellular red fluorescence clearly confirms the efficient internalization of the nanogels. The difference in fluorescence intensity between the two groups clearly demonstrates the successful internalization of the RhB-loaded nanogels. This enhanced uptake is most likely attributed to FA–mediated recognition of folate

receptors, which are overexpressed on MCF-7 cells, thereby facilitating receptor-mediated endocytosis. These findings substantiate the active targeting function of FA-modified nanogels and support their potential application in improving intracellular drug accumulation in folate receptor–positive breast cancer cells.

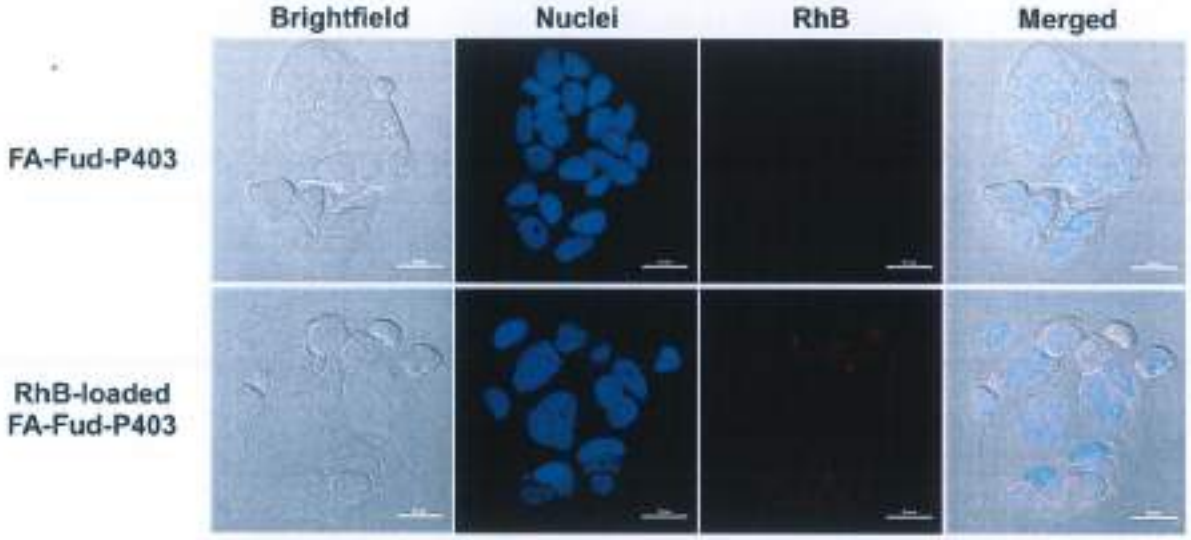

Figure 3.19. The confocal laser scanning confocal images for MCF-7cells treated with FA-Fud-P403 nanogels with and without loading rhodamine B. The nuclei were stained with DAPI (blue) and nanogels were stained with rhodamine B (red). The scale bars = 20 μm.

3.6.3. The synergism effect of combinatorial drugs against cancer cell

The synergistic interaction between Cis (Cis) and Cur (Cur) was quantitatively evaluated using the Chou–Talalay combination index (CI) model, which provides a rigorous framework for distinguishing synergistic, additive, and antagonistic effects based on the dose–response relationship. As presented in **Table 3.7**, the FA-Fud-P403@Cur/Cis formulation exhibited a CI value of 0.4969, significantly lower than 1, confirming a strong synergistic interaction between the two agents upon co-delivery within the nanogels system. According to the CI classification criteria, values in the range of 0.3–0.7 correspond to pronounced synergism, indicating that the combined cytotoxic effect substantially exceeds the expected additive outcome of Cis and Cur administered individually. Importantly, the CI–Fa profile **(Figure 3.20)** demonstrates that this synergistic behavior is maintained across a broad range of fractional inhibition (Fa ≈ 0.45–0.95). All CI values consistently remain below unity, indicating that the interaction is not only synergistic but also stable over increasing levels of cytotoxic response. This trend suggests that the cooperative effect between Cis and Cur is

preserved even under conditions requiring high therapeutic efficacy. From a mechanistic perspective, this sustained synergism can be attributed to the complementary modes of action of the two drugs. Cis exerts its cytotoxicity primarily through DNA crosslinking and apoptosis induction, whereas Cur modulates multiple cellular pathways, including oxidative stress and survival signaling. The co-encapsulation within a single nanocarrier enables intracellular delivery, thereby facilitating simultaneous action and enhancing the therapeutic response. Furthermore, the FA-functionalized Fud–P403 nanogels likely contributes to this effect by improving cellular uptake via receptor-mediated endocytosis and promoting co-localization of both drugs within tumor cells that not only enhances drug bioavailability but also maximizes the probability of interaction between their mechanisms of action, thereby reinforcing the observed synergistic outcome. Collectively, these results demonstrate that the FA-Fud-P403@Cur/Cis system achieves a robust and sustained synergistic effect over a wide therapeutic range. Such behavior is particularly advantageous for anticancer applications, as it enables enhanced tumor inhibition while potentially reducing the required dosage of each individual drug, thereby minimizing systemic toxicity and improving overall treatment efficiency.

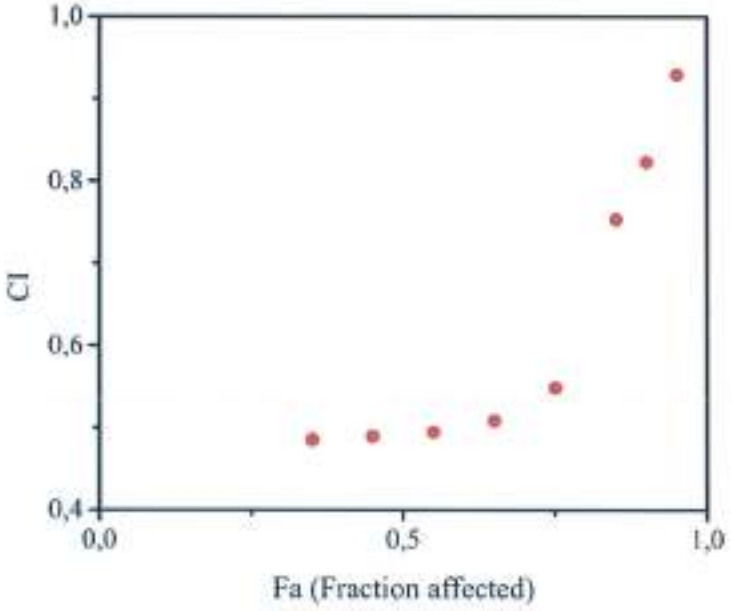

Figure 3.20. The CI values at different levels of growth inhibition effect (Fa) of FA- Fud-P403@Cur/Cis

A comparison of IC_{50} values further highlights the therapeutic advantage of the nanogels-based co-delivery strategy. The IC_{50} values of free Cis and free Cur against MCF-7 cells were 7.07 μg/mL and 9.96 μg/mL, respectively, whereas co-encapsulation within FA-Fud-P403 nanogels significantly reduced the effective IC_{50} values to 1.40 μg/mL for Cis and 5.46 μg/mL for Cur. This substantial decrease indicates a marked dose reduction while maintaining enhanced cytotoxic efficacy, suggesting improved pharmacological efficiency of the combined drugs. From a therapeutic perspective, such dose reduction is highly desirable, as it may potentially minimize systemic toxicity and adverse side effects commonly associated with conventional platinum-based chemotherapy. The observed synergistic effect can be attributed to the complementary and mutually reinforcing anticancer mechanisms of Cis and Cur. Cis primarily induces cytotoxicity through the formation of DNA crosslinks, leading to DNA damage and apoptosis, whereas Cur is known to modulate multiple oncogenic signaling pathways, including NF-κB, PI3K/Akt, and oxidative stress-related pathways, thereby sensitizing cancer cells to chemotherapeutic agents and enhancing apoptotic signaling [167]. The simultaneous delivery of these agents within a single nanocarrier likely promotes coordinated intracellular accumulation and synchronized pharmacodynamic interactions, resulting in amplified anticancer efficacy compared to monotherapy. In addition, the FA-functionalized Fud-P403 nanogels carrier plays a critical role in maximizing therapeutic performance. The presence of FA ligands enables folate receptor-mediated endocytosis, which is particularly effective in cancer cells that overexpress folate receptors, such as MCF-7 breast cancer cells. This active targeting mechanism enhances intracellular drug accumulation within tumor cells while minimizing nonspecific uptake in normal tissues. Furthermore, the nanogels matrix provides a sustained and localized drug release profile, which may prolong intracellular drug retention and further strengthen the cooperative pharmacological activity between Cis and Cur. Collectively, the CI analysis, CI–Fa relationship, and significant reduction in IC_{50} values clearly demonstrate that the FA-Fud-P403@Cur/Cis nanogels system achieves a robust and sustained synergistic anticancer effect, enabling effective tumor cell inhibition at substantially reduced drug doses. These findings highlight the strong potential of FA-Fud-P403 nanogels as an efficient nanocarrier platform for synergistic combination

This result suggests not only improved safety but also a potential synergistic benefit arising from the co-delivery of Cur and Cis. The enhanced tolerability observed in the dual-drug system can be attributed, at least in part, to the protective role of Cur. Cur is well known for its potent antioxidant and anti-inflammatory properties, which enable it to mitigate oxidative stress and inflammatory responses induced by Cis treatment. By scavenging reactive oxygen species and modulating key cellular signaling pathways, Cur may help preserve normal tissue function and reduce collateral damage during chemotherapy. Additionally, the co-encapsulation of both agents within a single nanocarrier ensures synchronized delivery, which may further optimize their interaction at the biological level.

Furthermore, tumor growth inhibition data further substantiate the superiority of the dual-loaded formulation **(Figure 3.21B-D)**. At day 15, tumors in the saline-treated group reached 2137.53 mm^3, confirming aggressive and uncontrolled tumor progression. Free Cis moderately suppressed tumor growth (1449.98 mm^3), yet the reduction was limited, likely due to rapid systemic clearance and suboptimal intratumoral retention. Encapsulation of Cis within FA-Fud-P403 nanogels significantly enhanced therapeutic efficacy, reducing tumor volume to 691.83 mm^3 ($p < 0.01$ vs free Cis), demonstrating improved tumor accumulation and sustained drug release. Importantly, the FA-Fud-P403@Cur/Cis formulation achieved the most pronounced tumor suppression, with tumor volume restricted to 365.47 mm^3 at the endpoint ($p < 0.001$ vs free Cis; $p < 0.01$ vs FA-Fud-P403@Cis). The magnitude of tumor inhibition observed in the dual-loaded group exceeds the expected additive effect of the individual treatments, strongly supporting a synergistic interaction between Cur and Cis *in vivo*. Mechanistically, this synergism can be rationalized at multiple levels. Cis exerts cytotoxicity primarily through DNA crosslinking and apoptosis induction; however, tumor resistance frequently arises via enhanced DNA repair, activation of pro-survival signaling pathways. Cur has been extensively reported to suppress NF-κB activation, inhibit PI3K/Akt signaling, modulate Bcl-2/Bax balance, and enhance ROS-mediated apoptosis. Therefore, co-delivery of Cur may sensitize tumor cells to Cis by downregulating survival pathways and impairing resistance mechanisms, thereby amplifying apoptosis induction. Moreover, synchronized intracellular delivery via the same nanocarrier ensures spatial and temporal co-localization of both drugs, maximizing pharmacodynamic interaction

chemotherapy, offering improved therapeutic efficacy and the possibility of reduced systemic toxicity in breast cancer treatment.

Table 3.5. The dose-effect relationship of two-drug combination on the MCF-7 cell line.

Sample	Cis IC_{50} (μg/mL)	Cur IC_{50} (μg/mL)	CI
Free Cis	7.06959	/	/
FA-Fud-P403@Cis	10.0422	/	/
Free Cur	/	9.9641	/
FA-Fud-P403@Cur	/	41.7356	/
FA-Fud-P403@Cur/Cis	1.3987	5.4605	0.4969

3.7. *In vivo* tumor inhibition

The *in vivo* therapeutic efficacy and synergistic potential of the dual-loaded FA-Fud-P403@Cur/Cis nanogels were rigorously evaluated in an MCF-7 subcutaneous xenograft model under dose-equivalent conditions (Cis 2.5 $mg \cdot kg^{-1}$). All formulations were administered intravenously over a 15-day treatment period, ensuring a consistent dosing regimen and enabling a direct, unbiased comparison of therapeutic outcomes across different groups. Body weight served as a critical indicator of systemic toxicity and overall treatment tolerability **(Figure 3.21A)**. Mice treated with free Cis exhibited a pronounced and continuous loss of body weight throughout the treatment period, which is a well-established manifestation of systemic toxicity associated with platinum-based chemotherapy. This adverse effect was further accompanied by visible signs of local tissue damage, including severe desquamation and inflammation at the injection site, suggesting nonspecific biodistribution and off-target cytotoxicity. These observations highlight the inherent limitations of free Cis administration, particularly its lack of selectivity and associated damage to healthy tissues. In contrast, mice treated with FA-Fud-P403@Cis and FA-Fud-P403@Cur/Cis nanogels showed a markedly improved physiological profile, characterized by steady and sustained body weight gain over the entire experimental period. This trend indicates a significant reduction in systemic toxicity upon nanogels encapsulation, likely due to improved pharmacokinetics, reduced premature drug release, and enhanced tumor-targeted delivery. Notably, the dual-loaded FA-Fud-P403@Cur/Cis group demonstrated the most favorable outcome, achieving the highest final body weight (27.79 g), which was significantly greater than both the free Cis and single-drug nanogels groups ($p < 0.05$).

within tumor cells. Histopathological analysis **(Figure 3.21E)** further corroborated these findings. Tumors from the saline group displayed densely packed viable tumor cells with intact morphology. Free Cis treatment induced only focal necrotic regions, indicating limited therapeutic penetration. FA-Fud-P403@Cis treatment resulted in more extensive necrosis and reduced tumor cell density, consistent with enhanced intratumoral accumulation. Strikingly, the dual-loaded FA-Fud-P403@Cur/Cis group exhibited diffuse and widespread tumor necrosis, large acellular void regions, nuclear condensation, and focal intratumoral hemorrhage associated with vascular disruption. These pathological features reflect severe structural collapse of tumor tissue and confirm profound cytotoxic impact.

Collectively, the statistically significant tumor suppression, improved safety profile, and extensive histological destruction observed in the FA-Fud-P403@Cur/Cis group demonstrate that the dual-drug nanogels system not only enhances Cis delivery but also effectively overcomes intrinsic resistance mechanisms through pharmacological synergism. These results provide compelling *in vivo* evidence that co-encapsulation of Cur and Cis within a targeted nanogels platform represents a superior therapeutic strategy compared to conventional monotherapy.

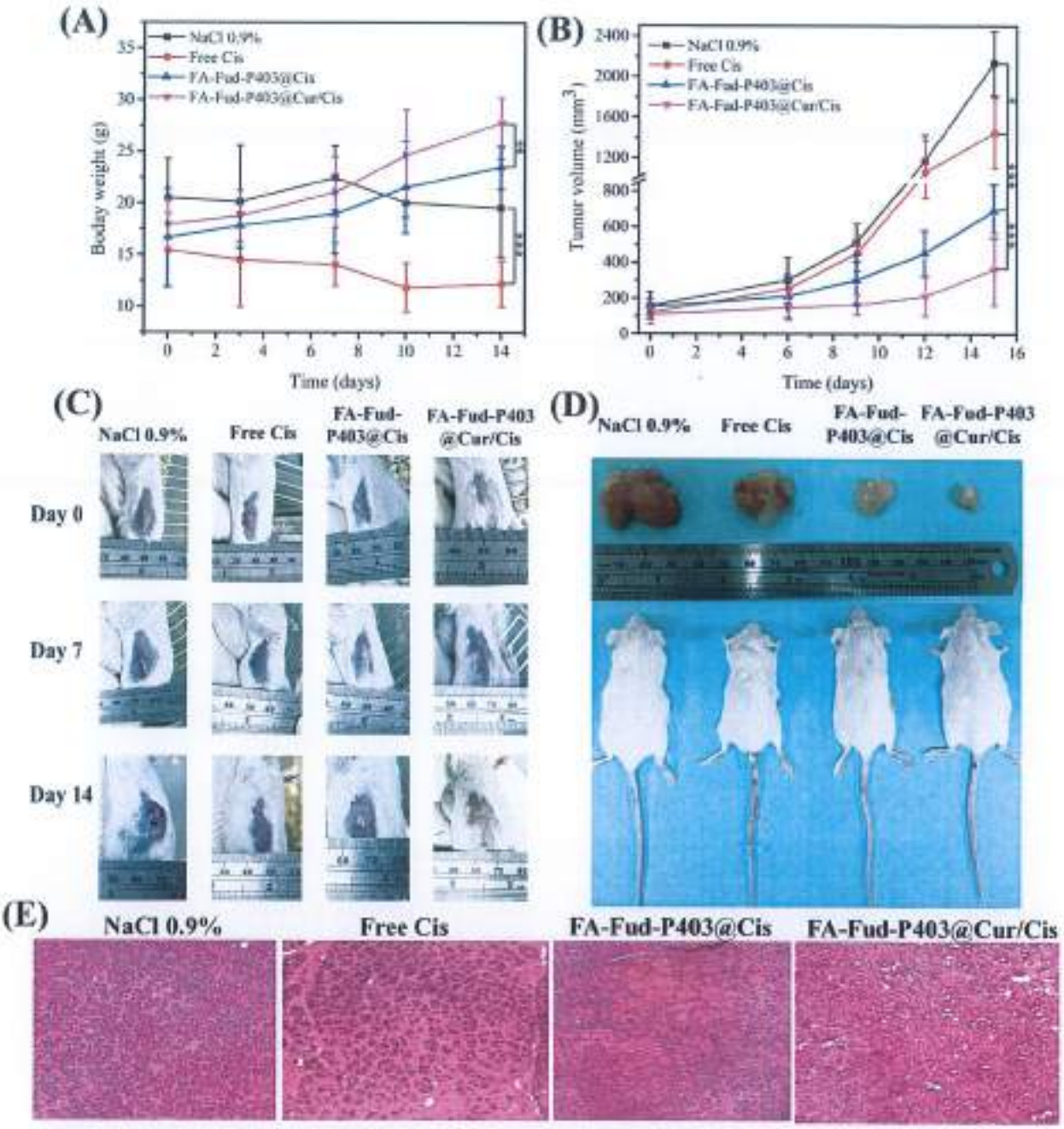

Figure 3.21. (A) The body weight and (B) relative tumor volumes of MCF-7 tumor-bearing mice treated with saline (negative control), free Cis (positive control), FA-Fud-P403@Cis, and FA-Fud-P403@Cur/Cis (n=3). (C) Photographs of tumor-bearing mice at interval time points with different treatments. (D) Photographs of isolated tumor tissues and (E) H&E images of stained tumor sections after 15 days of different treatments.

CONCLUSION AND FUTURE PROSPECT

1. Conclusion

This study successfully developed a biocompatible FA–Fud–P403 nanogels system for the co-delivery of Cur and Cis, enabling targeted breast cancer therapy. The nanogels, with a uniform size of 80–100 nm, are well-suited for tumor accumulation via the EPR effect, while minimizing premature clearance and degradation in biological environments. Folate functionalization conferred active targeting capability toward folate receptor-overexpressing cancer cells, significantly enhancing selective cytotoxicity. Among the formulations, FA–Fud–P403 exhibited superior performance, primarily due to the longer hydrophobic PPO segments of P403. This structural advantage resulted in a lower CMC value, higher drug-loading efficiency, and improved drug-retention capacity, ultimately leading to enhanced anticancer activity against MCF-7 cells, as evidenced by lower IC_{50} values. The nanogels system further demonstrated pH-responsive drug release, with accelerated release under acidic conditions that mimic the tumor microenvironment and intracellular compartments, thereby supporting controlled and site-specific delivery. Importantly, the co-delivery strategy produced a synergistic therapeutic effect, where Cur mitigated the systemic toxicity of Cis while potentiating its anticancer efficacy. Both *in vitro* and *in vivo* evaluations confirmed that FA–Fud–P403 effectively suppressed tumor growth while maintaining a favorable safety profile, with minimal cytotoxicity toward normal cells and no observable systemic toxicity in treated models. These findings highlight the potential of FA–Fud–P403 as an advanced dual-drug nanocarrier for precision oncology, suggesting a promising nanotherapeutic system, and synergistic drug delivery, active targeting, and controlled release, with strong potential for clinical development in targeted cancer therapy.

2. Future prospect

- Comprehensive *in vivo* biodistribution and targeting analysis restricts a full understanding of the nanogels behavior in complex biological systems.
- Increased sample size in animal studies may affect statistical robustness.
- Prioritize quantitative biodistribution studies using minimally invasive imaging strategies, alongside expanded *in vivo* cohorts to enhance statistical validity.
- Mechanistic investigations, including immunofluorescence-based receptor-binding analyses, as well as pharmacokinetic and long-term safety evaluations, are also essential to advance the translational potential of this platform.

THE LIST OF PUBLICATION

Dinh-Chuong Pham, Phuong Le Thi, Van Du Cao, Hoang Duy Nguyen, Hai Van Ngo, Anh Quan Hoang, Vu Phu Chi, Dinh Trung Nguyen, **Thanh Phu Nguyen**; "Effect of different poloxamers on anti-cancer activities of targeting folic acid-fucoidan nanogels for multi-drug delivery." *International Journal of Biological Macromolecules* (2026): 151417.

REFERENCE

[1] Siegel, R.L., Miller, K.D., Wagle, N.S., and Jemal, A. , 2023, Cancer statistics, 2023. *CA: A Cancer Journal for Clinicians*. 73 (1), 17–48.

[2] Wei, G., Wang, Y., Yang, G., Wang, Y., and Ju, R. , 2021, Recent progress in nanomedicine for enhanced cancer chemotherapy. *Theranostics*. 11 (13), 6370–6392.

[3] Anand, U., Dey, A., Chandel, A.K.S., Sanyal, R., Mishra, A., Pandey, D.K., et al. , 2023, Cancer chemotherapy and beyond: Current status, drug candidates, associated risks and progress in targeted therapeutics. *Genes & Diseases*. 10 (4), 1367–1401.

[4] Alqosaibi, A.I. , 2022, Nanocarriers for anticancer drugs: Challenges and perspectives. *Saudi Journal of Biological Sciences*. 29 (6), 103298.

[5] Wu, L., Sun, J., Su, X., Yu, Q., Yu, Q., and Zhang, P. , 2016, A review about the development of fucoidan in antitumor activity: Progress and challenges. *Carbohydrate Polymers*. 154 96–111.

[6] Kaushik, N., Borkar, S.B., Nandanwar, S.K., Panda, P.K., Choi, E.H., and Kaushik, N.K. , 2022, Nanocarrier cancer therapeutics with functional stimuli-responsive mechanisms. *Journal of Nanobiotechnology*. 20 (1), 152.

[7] Alexis, F., Pridgen, E.M., Langer, R., and Farokhzad, O.C. , 2010, Nanoparticle Technologies for Cancer Therapy. in: pp. 55–86.

[8] Niu, J., Wang, L., Yuan, M., Zhang, J., Chen, H., and Zhang, Y. , 2020, Dual-targeting nanocarrier based on glucose and folic acid functionalized pluronic P105 polymeric micelles for enhanced brain distribution. *Journal of Drug Delivery Science and Technology*. 57 101343.

[9] Mi, F.-L., Wang, L.-F., Chu, P.-Y., Peng, S.-L., Feng, C.-L., Lai, Y.-J., et al. , 2018, Active Tumor-Targeted co-Delivery of Epigallocatechin Gallate and Doxorubicin in Nanoparticles for Combination Gastric Cancer Therapy. *ACS Biomaterials Science & Engineering*. 4 (8), 2847–2859.

[10] Anirudhan, T.S., Varghese, S., and Manjusha, V. , 2021, Hyaluronic acid coated Pluronic F127/Pluronic P123 mixed micelle for targeted delivery of Paclitaxel and Curcumin. *International Journal of Biological Macromolecules*. 192 950–957.

[11] Van Thoai, D., Nguyen, D.T., Dang, L.H., Nguyen, N.H., Nguyen, V.T., Doan, P., et al. , 2020, Lipophilic effect of various pluronic-grafted gelatin copolymers on the quercetin delivery efficiency in these self-assembly nanogels. *Journal of Polymer Research*. 27 (12), 369.

[12] Nguyen, V.T., Nguyen, D.T., Nguyen, D.N., Tran, N.Q., and Do, H. , 2024, Investigation of the properties of chitosan–Pluronic based nanogels drug delivery systems utilizing various Pluronic types. *Polymer Engineering & Science*. 64 (11), 5392–5410.

[13] Nguyen, N.T., Nguyen, V.T., Vu, T.T., Le Nguyen, T.V., Nguyen, T.T.T., Huynh, P.D., et al. , 2024, Efficient and controllable co-delivery of paclitaxel and curcumin from fucoidan-pluronic F127 nanogels for synergistic breast cancer treatment. *Macromolecular Research*. 32 (5), 427–442.

[14] Nguyen, V.T., Doan, P., Nguyen, D.T., Doan, V.-D., Dao, T.P., Plavskii, V., et al. , 2022, Effect of targeting ligand designation of self-assembly chitosan-poloxamer nanogels loaded Paclitacel on inhibiting MCF-7 cancer cell growth. *Journal of Biomaterials Science, Polymer Edition*. 33 (4), 426–442.

[15] Nguyen, D.T., Nguyen, T.P., Dinh, V.T., Nguyen, N.H., Nguyen, K.T.H., Nguyen, T.H., et al. , 2023, Potential from synergistic effect of quercetin and paclitaxel co-encapsulated in the targeted folic–gelatin–pluronic P123 nanogels for chemotherapy. *International Journal of Biological Macromolecules*. 243 125248.

[16] Nguyen, V.T., Nguyen, T.H., Dang, L.H., Vu-Quang, H., and Tran, N.Q. , 2019, Folate-Conjugated Chitosan-Pluronic P123 Nanogels: Synthesis and Characterizations towards Dual Drug Delivery. *Journal of Nanomaterials*. 2019 1–14.

[17] Torre, L.A., Siegel, R.L., Ward, E.M., and Jemal, A. , 2016, Global Cancer Incidence and Mortality Rates and Trends—An Update. *Cancer Epidemiology, Biomarkers & Prevention*. 25 (1), 16–27.

[18] Bray, F., Laversanne, M., Sung, H., Ferlay, J., Siegel, R.L., Soerjomataram, I., et al. , 2024, Global cancer statistics 2022: GLOBOCAN estimates of incidence and mortality worldwide for 36 cancers in 185 countries. *CA: A Cancer Journal for Clinicians*. 74 (3), 229–263.

[19] Ha, L., Tran, A., Bui, L., Giovannucci, E., Mucci, L., Song, M., et al. , 2023, Proportion and number of cancer cases and deaths attributable to behavioral risk factors in Vietnam. *International Journal of Cancer*. 153 (3), 524–538.

[20] Islami, F., Goding Sauer, A., Miller, K.D., Siegel, R.L., Fedewa, S.A., Jacobs, E.J., et al. , 2018, Proportion and number of cancer cases and deaths attributable to potentially modifiable risk factors in the United States. *CA: A Cancer Journal for Clinicians*. 68 (1), 31–54.

[21] Sriharikrishnaa, S., Suresh, P.S., and Prasada K., S. , 2023, An Introduction to Fundamentals of Cancer Biology. in: pp. 307–330.

[22] Rajput, J. , 2023, CANCER: A COMPREHENSIVE REVIEW. *International Journal of Research in Pharmacy and Chemistry*. 1 42–49.

[23] Zafar, A., Khatoon, S., Khan, M.J., Abu, J., and Naeem, A. , 2025, Advancements and limitations in traditional anti-cancer therapies: a comprehensive review of surgery, chemotherapy, radiation therapy, and hormonal therapy. *Discover Oncology*. 16 (1), 607.

[24] Yang, S.-M., Hsu, H.-H., and Chen, J.-S. , 2017, Recent advances in surgical management of early lung cancer. *Journal of the Formosan Medical Association*. 116 (12), 917–923.

[25] Greenhalgh, T.A. and Symonds, R.P. , 2014, Principles of chemotherapy and radiotherapy. *Obstetrics, Gynaecology & Reproductive Medicine*. 24 (9), 259–265.

[26] Kim, S.M., Faix, P.H., and Schnitzer, J.E. , 2017, Overcoming key biological barriers to cancer drug delivery and efficacy. *Journal of Controlled Release : Official Journal of the Controlled Release Society*. 267 15–30.

[27] Lovejoy, K.S., Todd, R.C., Zhang, S., McCormick, M.S., D'Aquino, J.A., Reardon, J.T., et al. , 2008, *cis* -Diammine(pyridine)chloroplatinum(II), a monofunctional platinum(II) antitumor agent: Uptake, structure, function, and prospects. *Proceedings of the National Academy of Sciences*. 105 (26), 8902–8907.

[28] Sullivan, E.J., Kurtoglu, M., Wangpaichitr, M., Savaraj, N., and Lampidis, T. , 2011, Abstract 4087: Metabolic changes associated with acquired cisplatin resistance. *Cancer Research*. 71 (8_Supplement), 4087–4087.

[29] Cecati, M., Pozzi, V., Pompei, V., Schiavoni, V., Fumarola, S., Romagnoli, A., et al. , 2026, Cisplatin as a Xenobiotic Agent: Molecular Mechanisms of Actions and Clinical Applications in Oncology. *Journal of Xenobiotics*. 16 (1), 9.

[30] Tchounwou, P.B., Dasari, S., Noubissi, F.K., Ray, P., and Kumar, S. , 2021, Advances in Our Understanding of the Molecular Mechanisms of Action of Cisplatin in Cancer Therapy. *Journal of Experimental Pharmacology*. Volume 13 303–328.

[31] Alassaf, N. and Attia, H. , 2023, Autophagy and necroptosis in cisplatin-induced acute kidney injury: Recent advances regarding their role and therapeutic potential. *Frontiers in Pharmacology*. 14.

[32] Wang, Z. and Zhu, G. , 2018, DNA Damage Repair Pathways and Repair of Cisplatin-Induced DNA Damage. in: Reference Module in Chemistry, Molecular Sciences and Chemical Engineering, Elsevier, .

[33] Xu, F., Gao, Y., Zhou, X., Cui, J., Wei, R., and Peng, T. , 2026, Calcium overloaded multifunctional composite nanomaterials synergistically treat cancer by ferroptosis pathway. *Journal of Colloid and Interface Science*. 710 139961.

[34] Zaroon, Z., D'Ambrosio, C., and de Nigris, F. , 2026, Mitochondrial Dysfunction in Acute Kidney Injury: Intersections Between Chemotherapy and Novel Cancer Immunotherapies. *Biomolecules*. 16 (1), 120.

[35] Pang, S., Lin, Q., Pang, T., Hou, J., Li, P., Guo, E., et al. , 2026, Efficacy and mechanisms of cisplatin and sulforaphane nanoparticles in alleviating cisplatin resistance in non-small cell lung cancer. *Translational Lung Cancer Research*. 15 (1), 15–15.

[36] Tang, C., Livingston, M.J., Safirstein, R., and Dong, Z. , 2023, Cisplatin nephrotoxicity: new insights and therapeutic implications. *Nature Reviews Nephrology*. 19 (1), 53–72.

[37] Merheb, D., Dib, G., Zerdan, M.B., Nakib, C. El, Alame, S., and Assi, H.I. , 2022, Drug-Induced Peripheral Neuropathy: Diagnosis and Management. *Current Cancer Drug Targets*. 22 (1), 49–76.

[38] Ranasinghe, R., Mathai, M.L., and Zulli, A. , 2022, Cisplatin for cancer therapy and overcoming chemoresistance. *Heliyon*. 8 (9), e10608.

[39] Su, Y., Zhang, X., Li, S., Xie, W., and Guo, J. , 2022, Emerging Roles of the Copper–CTR1 Axis in Tumorigenesis. *Molecular Cancer Research*. 20 (9), 1339–1353.

[40] Lugones, Y., Loren, P., and Salazar, L.A. , 2022, Cisplatin Resistance: Genetic and Epigenetic Factors Involved. *Biomolecules*. 12 (10),.

[41] Aldossary, S.A. , 2019, Review on Pharmacology of Cisplatin: Clinical Use, Toxicity and Mechanism of Resistance of Cisplatin. *Biomedical and Pharmacology Journal*. 12 (1), 07–15.

[42] Mittal, D. and Verma, A.K. , 2025, Nanotherapeutic interventions to enhance cisplatin sensitivity in ovarian cancer cells. *Egyptian Journal of Medical Human Genetics*. 26 (1), 131.

[43] Molski, M. , 2025, Reactivity of Curcumin: Theoretical Insight from a Systematic Density Functional Theory-Based Review. *International Journal of Molecular Sciences*. 26 (21), 10374.

[44] Sanphui, P. and Bolla, G. , 2018, Curcumin, a Biological Wonder Molecule: A Crystal Engineering Point of View. *Crystal Growth & Design*. 18 (9), 5690–5711.

[45] Zhai, K., Brockmüller, A., Kubatka, P., Shakibaei, M., and Büsselberg, D. , 2020, Curcumin's Beneficial Effects on Neuroblastoma: Mechanisms, Challenges, and Potential Solutions. *Biomolecules*. 10 (11), 1469.

[46] Jacob, S., Kather, F., Morsy, M., Boddu, S., Attimarad, M., Shah, J., et al. , 2024, Advances in Nanocarrier Systems for Overcoming Formulation Challenges of Curcumin: Current Insights. *Nanomaterials*. 14 (8), 672.

[47] Gao, H., Seidi, F., Cai, Y., Sun, Z., Bian, H., Dai, H., et al. , 2025, Construction of curcumin-conjugated pH-responsive lignin-based nanoparticles for alleviating oxidative stress: Stability, antioxidant activity and biocompatibility. *International Journal of Biological Macromolecules*. 302 140036.

[48] Maheshwari, R.K., Singh, A.K., Gaddipati, J., and Srimal, R.C. , 2006, Multiple biological activities of curcumin: A short review. *Life Sciences*. 78 (18), 2081–2087.

[49] Indira Priyadarsini, K. , 2013, Chemical and Structural Features Influencing the Biological Activity of Curcumin. *Current Pharmaceutical Design*. 19 (11), 2093–2100.

[50] Waghule, T., Gorantla, S., Rapalli, V.K., Shah, P., Dubey, S.K., Saha, R.N., et al. , 2020, Emerging Trends in Topical Delivery of Curcumin Through Lipid Nanocarriers: Effectiveness in Skin Disorders. *AAPS PharmSciTech*. 21 (7), 284.

[51] Jobin, C., Bradham, C.A., Russo, M.P., Juma, B., Narula, A.S., Brenner, D.A., et al. , 1999, Curcumin blocks cytokine-mediated NF-kappa B activation and proinflammatory gene expression by inhibiting inhibitory factor I-kappa B kinase activity. *Journal of Immunology (Baltimore, Md. : 1950)*. 163 (6), 3474–83.

[52] Menon, V.P. and Sudheer, A.R. n.d. ANTIOXIDANT AND ANTI-INFLAMMATORY PROPERTIES OF CURCUMIN. in: The Molecular Targets and Therapeutic Uses of Curcumin in Health and Disease, Springer US, Boston, MApp. 105–125.

[53] Phan, T.-T., See, P., Lee, S.-T., and Chan, S.-Y. , 2001, Protective Effects of Curcumin against Oxidative Damage on Skin Cells In Vitro: Its Implication for Wound Healing. *The Journal of Trauma: Injury, Infection, and Critical Care*. 51 (5), 927–931.

[54] Lai, H.-W., Chien, S.-Y., Kuo, S.-J., Tseng, L.-M., Lin, H.-Y., Chi, C.-W., et al. , 2012, The Potential Utility of Curcumin in the Treatment of HER-2-Overexpressed Breast Cancer: An *In Vitro* and *In Vivo* Comparison Study with Herceptin. *Evidence-Based Complementary and Alternative Medicine*. 2012 1–12.

[55] Guo, L., Chen, X., Hu, Y., Yu, Z., Wang, D., and Liu, J. , 2013, Curcumin Inhibits Proliferation and Induces Apoptosis of Human Colorectal Cancer Cells by Activating the Mitochondria Apoptotic Pathway. *Phytotherapy Research*. 27 (3), 422–430.

[56] Shanmugam, M., Rane, G., Kanchi, M., Arfuso, F., Chinnathambi, A., Zayed, M., et al. , 2015, The Multifaceted Role of Curcumin in Cancer Prevention and Treatment. *Molecules*. 20 (2), 2728–2769.

[57] Irani, S. , 2019, Emerging insights into the biology of metastasis: A review article. *Iranian Journal of Basic Medical Sciences*. 22 (8), 833–847.

[58] Kim, K., Lee, E.N., Park, J.K., Lee, J., Kim, J., Choi, H., et al. , 2012, Curcumin Attenuates TNF-α-induced Expression of Intercellular Adhesion Molecule-1,

Vascular Cell Adhesion Molecule-1 and Proinflammatory Cytokines in Human Endometriotic Stromal Cells. *Phytotherapy Research*. 26 (7), 1037–1047.

[59] Dasari, S. and Bernard Tchounwou, P. , 2014, Cisplatin in cancer therapy: Molecular mechanisms of action. *European Journal of Pharmacology*. 740 364–378.

[60] Cheng, Y., Zhao, P., Wu, S., Yang, T., Chen, Y., Zhang, X., et al. , 2018, Cisplatin and curcumin co-loaded nano-liposomes for the treatment of hepatocellular carcinoma. *International Journal of Pharmaceutics*. 545 (1–2), 261–273.

[61] Oršolić, N. and Jazvinšćak Jembrek, M. , 2024, Potential Strategies for Overcoming Drug Resistance Pathways Using Propolis and Its Polyphenolic/Flavonoid Compounds in Combination with Chemotherapy and Radiotherapy. *Nutrients*. 16 (21), 3741.

[62] Mohan, A., Narayanan, S., Sethuraman, S., and Maheswari Krishnan, U. , 2013, Combinations of Plant Polyphenols & Anti-Cancer Molecules: A Novel Treatment Strategy for Cancer Chemotherapy. *Anti-Cancer Agents in Medicinal Chemistry*. 13 (2), 281–295.

[63] Toden, S., Okugawa, Y., Jascur, T., Wodarz, D., Komarova, N.L., Buhrmann, C., et al. , 2015, Curcumin mediates chemosensitization to 5-fluorouracil through miRNA-induced suppression of epithelial-to-mesenchymal transition in chemoresistant colorectal cancer. *Carcinogenesis*. 36 (3), 355–367.

[64] Kumar, P., Barua, C.C., Sulakhiya, K., and Sharma, R.K. , 2017, Curcumin Ameliorates Cisplatin-Induced Nephrotoxicity and Potentiates Its Anticancer Activity in SD Rats: Potential Role of Curcumin in Breast Cancer Chemotherapy. *Frontiers in Pharmacology*. 8.

[65] Abadi, A.J., Mirzaei, S., Mahabady, M.K., Hashemi, F., Zabolian, A., Hashemi, F., et al. , 2022, Curcumin and its derivatives in cancer therapy: Potentiating antitumor activity of cisplatin and reducing side effects. *Phytotherapy Research*. 36 (1), 189–213.

[66] Li, T. and Li, Y. , 2023, Quercetin acts as a novel anti-cancer drug to suppress cancer aggressiveness and cisplatin-resistance in nasopharyngeal carcinoma (NPC) through regulating the yes-associated protein/Hippo signaling pathway. *Immunobiology*. 228 (2), 152324.

[67] Aqil, F., Munagala, R., Jeyabalan, J., and Vadhanam, M. V , 2013, Bioavailability of phytochemicals and its enhancement by drug delivery systems. *Cancer Letters*. 334 (1), 133–41.

[68] Golzardi, M. and Glamočlija, U. , 2025, Solubility of phytochemicals and challenges in in vitro studies: a literature review. *Periodicals of Engineering and Natural Sciences (PEN)*. 13 (2), 417–424.

[69] Kumar, G., Virmani, T., Sharma, A., and Pathak, K. , 2023, Codelivery of Phytochemicals with Conventional Anticancer Drugs in Form of Nanocarriers. *Pharmaceutics*. 15 (3), 889.

[70] Patel, D., Kuperkar, K., Yusa, S., and Bahadur, P. , 2023, Nanoscale Self-Assemblies from Amphiphilic Block Copolymers as Proficient Templates in Drug Delivery. *Drugs and Drug Candidates*. 2 (4), 898–922.

[71] Bodratti, A.M. and Alexandridis, P. , 2018, Amphiphilic block copolymers in drug delivery: advances in formulation structure and performance. *Expert Opinion on Drug Delivery*. 15 (11), 1085–1104.

[72] Bajracharya, R., Song, J.G., Patil, B.R., Lee, S.H., Noh, H.-M., Kim, D.-H., et al. , 2022, Functional ligands for improving anticancer drug therapy: current status and applications to drug delivery systems. *Drug Delivery*. 29 (1), 1959–1970.

[73] Prakash, S. , 2023, Nano-based drug delivery system for therapeutics: a comprehensive review. *Biomedical Physics & Engineering Express*. 9 (5), 052002.

[74] De, R., Mahata, M.K., and Kim, K. , 2022, Structure-Based Varieties of Polymeric Nanocarriers and Influences of Their Physicochemical Properties on Drug Delivery Profiles. *Advanced Science*. 9 (10),.

[75] Mauri, E., Giannitelli, S.M., Trombetta, M., and Rainer, A. , 2021, Synthesis of Nanogels: Current Trends and Future Outlook. *Gels*. 7 (2), 36.

[76] Suhail, M., Rosenholm, J.M., Minhas, M.U., Badshah, S.F., Naeem, A., Khan, K.U., et al. , 2019, Nanogels As drug-delivery Systems: a Comprehensive Overview. *Therapeutic Delivery*. 10 (11), 697–717.

[77] Kumar, A. and Chang, D.W. , 2024, Active Polymers Decorated with Major Acid Groups for Water Treatment: Potentials and Challenges. *Polymers*. 17 (1), 29.

[78] Cai, Y.-E., Huang, Y.-H., Tsui, K.-H., Chuang, A.E.-Y., Huang, S.-F., Lee, K.-T., et al. , 2026, Optimization of freeze–thawed humic acid/polyvinyl alcohol supramolecular hydrogels via Taguchi method: structural, mechanical, and biological evaluations. *Journal of Polymer Research*. 33 (1), 26.

[79] Narayanan, K., Bhaskar, R., and Han, S. , 2022, Recent Advances in the Biomedical Applications of Functionalized Nanogels. *Pharmaceutics*. 14 (12), 2832.

[80] Panico, S., Capolla, S., Bozzer, S., Toffoli, G., Dal Bo, M., and Macor, P. , 2022, Biological Features of Nanoparticles: Protein Corona Formation and Interaction with the Immune System. *Pharmaceutics*. 14 (12), 2605.

[81] Pustulka, S.M., Ling, K., Pish, S.L., and Champion, J.A. , 2020, Protein Nanoparticle Charge and Hydrophobicity Govern Protein Corona and Macrophage Uptake. *ACS Applied Materials & Interfaces*. 12 (43), 48284–48295.

[82] Miyata, T. , 2026, Design and Applications of Stimuli-Responsive Micro/Nanogels. in: Micro and Nano Gels, Wiley, pp. 481–517.

[83] Singh, R., Jadhav, K., Jhilta, A., Negi, S., and Verma, R.K. , 2026, Stimuli-Responsive Nanogels for Cancer Therapy. in: Advances in Stimuli-Responsive Nanosystems for Cancer Therapy, Springer Nature Singapore, Singaporepp. 213–231.

[84] Mohlala, R.L., Fakayode, O.J., Chauke, N.M., Mathumba, P., May, B.M., Mothudi, B.M., et al. , 2026, Design Principles for Smart Polymer Sensors: Selectivity, Sensitivity, Stability, and Regeneration. in: The Polymer-Water Nexus, Springer Nature Switzerland, Champp. 305–349.

[85] Le, M., Huang, W., Chen, K.-F., Lin, C., Cai, L., Zhang, H., et al. , 2022, Upper critical solution temperature polymeric drug carriers. *Chemical Engineering Journal*. 432 134354.

[86] Chung, J.E., Yokoyama, M., Yamato, M., Aoyagi, T., Sakurai, Y., and Okano, T. , 1999, Thermo-responsive drug delivery from polymeric micelles constructed using block copolymers of poly(N-isopropylacrylamide) and poly(butylmethacrylate). *Journal of Controlled Release*. 62 (1–2), 115–127.

[87] Ghaeini-Hesaroeiye, S., Razmi Bagtash, H., Boddohi, S., Vasheghani-Farahani, E., and Jabbari, E. , 2020, Thermoresponsive Nanogels Based on Different Polymeric Moieties for Biomedical Applications. *Gels*. 6 (3), 20.

[88] Toumpa, D., Angelopoulou, A., Avgoustakis, K., and Pasparakis, G. , 2026, Controlled delivery of camptothecin and gemcitabine using thermo- and ultrasound-responsive polymeric nanoparticles for pancreatic cancer.

[89] Yu, J., Qiu, H., Yin, S., Wang, H., and Li, Y. , 2021, Polymeric Drug Delivery System Based on Pluronics for Cancer Treatment. *Molecules*. 26 (12), 3610.

[90] Bomediano, M.P., da Silva, L.C.E., Plivelic, T.S., and de Oliveira, M.G. , 2026, Self-Assembly and Gelation Behavior of Methacrylated PEO–PPO–PEO Triblock Copolymers Pluronic F127. *Langmuir*. 42 (10), 7452–7462.

[91] Dave, R., Randhawa, G., Kim, D., Simpson, M., and Hoare, T. , 2022, Microgels and Nanogels for the Delivery of Poorly Water-Soluble Drugs. *Molecular Pharmaceutics*. 19 (6), 1704–1721.

[92] Onzi, G., Guterres, S.S., Pohlmann, A.R., and Frank, L.A. , 2021, Passive Targeting and the Enhanced Permeability and Retention (EPR) Effect. in: The ADME Encyclopedia, Springer International Publishing, Champp. 1–13.

[93] Attama, A.A., Nnamani, P.O., Onokala, O.B., Ugwu, A.A., and Onugwu, A.L. , 2022, Nanogels as target drug delivery systems in cancer therapy: A review of the last decade. *Frontiers in Pharmacology*. 13.

[94] Yazdan, M., Naghib, S.M., and Mozafari, M.R. , 2024, Polymeric Micelle-Based Nanogels as Emerging Drug Delivery Systems in Breast Cancer Treatment: Promises and Challenges. *Current Drug Targets*. 25 (10), 649–669.

[95] Alidriss, O.M., AlSudais, H., Alhumaidan, O.S., Altwaijry, H.D., Bakhsh, A., Almuhanna, Y., et al. , 2025, Targeted Drug Delivery Strategies in Overcoming Antimicrobial Resistance: Advances and Future Directions. *Pharmaceutics*. 17 (11), 1426.

[96] , 2025, Targeted Drug Delivery Systems for Cancer Management: Advancements, Challenges, and Future Directions. *EKSPLORIUM*.

[97] Li, J., Hou, Y., Wu, H., Chen, C., Fu, X., Liu, J., et al. , 2025, A poly (vinyl alcohol) coated core-shell nanoparticle with a tunable surface for pH and glutathione dual-responsive drug delivery. *Colloids and Surfaces B: Biointerfaces*. 247 114421.

[98] Zhao, L.-Y. and Zhang, W.-M. , 2017, Recent progress in drug delivery of pluronic P123: pharmaceutical perspectives. *Journal of Drug Targeting*. 25 (6), 471–484.

[99] Hezaveh, S., Samanta, S., De Nicola, A., Milano, G., and Roccatano, D. , 2012, Understanding the Interaction of Block Copolymers with DMPC Lipid Bilayer Using Coarse-Grained Molecular Dynamics Simulations. *The Journal of Physical Chemistry B*. 116 (49), 14333–14345.

[100] Wei, Z., Hao, J., Yuan, S., Li, Y., Juan, W., Sha, X., et al. , 2009, Paclitaxel-loaded Pluronic P123/F127 mixed polymeric micelles: Formulation, optimization and in vitro characterization. *International Journal of Pharmaceutics*. 376 (1–2), 176–185.

[101] Xiong, X.Y., Tam, K.C., and Gan, L.H. , 2006, Polymeric Nanostructures for Drug Delivery Applications Based on Pluronic Copolymers Systems. *Journal of Nanoscience and Nanotechnology*. 6 (9), 2638–2650.

[102] Xu, W., Ling, P., and Zhang, T. , 2013, Polymeric Micelles, a Promising Drug Delivery System to Enhance Bioavailability of Poorly Water-Soluble Drugs. *Journal of Drug Delivery*. 2013 1–15.

[103] Osorno, L., Brandley, A., Maldonado, D., Yiantsos, A., Mosley, R., and Byrne, M. , 2021, Review of Contemporary Self-Assembled Systems for the Controlled Delivery of Therapeutics in Medicine. *Nanomaterials*. 11 (2), 278.

[104] Nagarajan, R. , 1999, Solubilization of hydrocarbons and resulting aggregate shape transitions in aqueous solutions of Pluronic® (PEO–PPO–PEO) block copolymers. *Colloids and Surfaces B: Biointerfaces*. 16 (1–4), 55–72.

[105] Zhao, L., Du, J., Duan, Y., Zang, Y., Zhang, H., Yang, C., et al. , 2012, Curcumin loaded mixed micelles composed of Pluronic P123 and F68: Preparation, optimization and in vitro characterization. *Colloids and Surfaces B: Biointerfaces*. 97 101–108.

[106] Wei, Z., Yuan, S., Hao, J., and Fang, X. , 2013, Mechanism of inhibition of P-glycoprotein mediated efflux by Pluronic P123/F127 block copolymers: Relationship between copolymers concentration and inhibitory activity. *European Journal of Pharmaceutics and Biopharmaceutics*. 83 (2), 266–274.

[107] Murhammer, D.W. and Goochee, C.F. , 1990, Structural Features of Nonionic Polyglycol Polymer Molecules Responsible for the Protective Effect in Sparged Animal Cell Bioreactors. *Biotechnology Progress*. 6 (2), 142–148.

[108] Rahdar, A., kazemi, S., and Askari, F. , 2018, Pluronic as nano-carier for drug delivery systems. *Nanomedicine Research Journal*. 3 (4), 174–179.

[109] Bonacucina, G., Cespi, M., Mencarelli, G., Giorgioni, G., and Palmieri, G.F. , 2011, Thermosensitive Self-Assembling Block Copolymers as Drug Delivery Systems. *Polymers*. 3 (2), 779–811.

[110] Clerkin, S., Singh, K., Winning, D., Krupa, I., Crean, J., Brougham, D.F., et al. , 2025, Thermoresponsive polymers for cell support: poloxamers as a case study of promise and challenge. *Journal of Materials Chemistry B*. 13 (31), 9351–9376.

[111] Dheer, D., Arora, D., Jaglan, S., Rawal, R.K., and Shankar, R. , 2017, Polysaccharides based nanomaterials for targeted anti-cancer drug delivery. *Journal of Drug Targeting*. 25 (1), 1–16.

[112] The, N.N. , 2022, Synthesis of a novel nano-carrier system based on fucoidan conjugated to Pluronic for cell-targeted delivery of anti-cancer drugs. *Vietnam Journal of Chemistry*. 60 (S1), 80–85.

[113] Zayed, A., El-Aasr, M., Ibrahim, A.-R.S., and Ulber, R. , 2020, Fucoidan Characterization: Determination of Purity and Physicochemical and Chemical Properties. *Marine Drugs*. 18 (11), 571.

[114] Li, B., Lu, F., Wei, X., and Zhao, R. , 2008, Fucoidan: Structure and Bioactivity. *Molecules*. 13 (8), 1671–1695.

[115] Zhang, X., Wei, Z., and Xue, C. , 2022, Physicochemical properties of fucoidan and its applications as building blocks of nutraceutical delivery systems. *Critical Reviews in Food Science and Nutrition*. 62 (32), 8935–8953.

[116] Du, B., Zhao, Q., Cheng, C., Wang, H., Liu, Y., Zhu, F., et al. , 2022, A critical review on extraction, characteristics, physicochemical activities, potential health benefits, and industrial applications of fucoidan. *EFood*. 3 (4),.

[117] Iqbal, M.W., Riaz, T., Mahmood, S., Bilal, M., Manzoor, M.F., Qamar, S.A., et al. , 2024, Fucoidan-based nanomaterial and its multifunctional role for pharmaceutical and biomedical applications. *Critical Reviews in Food Science and Nutrition*. 64 (2), 354–380.

[118] Haggag, Y., Abd Elrahman, A., Ulber, R., and Zayed, A. , 2023, Fucoidan in Pharmaceutical Formulations: A Comprehensive Review for Smart Drug Delivery Systems. *Marine Drugs*. 21 (2), 112.

[119] Wang, Y., Xing, M., Cao, Q., Ji, A., Liang, H., and Song, S. , 2019, Biological Activities of Fucoidan and the Factors Mediating Its Therapeutic Effects: A Review of Recent Studies. *Marine Drugs*. 17 (3), 183.

[120] , 2015, Cover sheet Cover sheet Title The anti-cancer activity of the natural product, fucoidan, in haematological malignancies.

[121] Chen, P.-H., Chiang, P.-C., Lo, W.-C., Su, C.-W., Wu, C.-Y., Chan, C.-H., et al. , 2021, A novel fucoidan complex-based functional beverage attenuates oral cancer through inducing apoptosis, G2/M cell cycle arrest and retarding cell migration/invasion. *Journal of Functional Foods*. 85 104665.

[122] Chantree, P., Na-Bangchang, K., and Martviset, P. , 2021, Anticancer Activity of Fucoidan via Apoptosis and Cell Cycle Arrest on Cholangiocarcinoma Cell. *Asian Pacific Journal of Cancer Prevention*. 22 (1), 209–217.

[123] Senthilkumar, K., Manivasagan, P., Venkatesan, J., and Kim, S.-K. , 2013, Brown seaweed fucoidan: Biological activity and apoptosis, growth signaling mechanism in cancer. *International Journal of Biological Macromolecules*. 60 366–374.

[124] Atashrazm, F., Lowenthal, R., Woods, G., Holloway, A., and Dickinson, J. , 2015, Fucoidan and Cancer: A Multifunctional Molecule with Anti-Tumor Potential. *Marine Drugs*. 13 (4), 2327–2346.

[125] Lin, Y., Qi, X., Liu, H., Xue, K., Xu, S., and Tian, Z. , 2020, The anti-cancer effects of fucoidan: a review of both in vivo and in vitro investigations. *Cancer Cell International*. 20 (1), 154.

[126] Lu, K.-Y., Li, R., Hsu, C.-H., Lin, C.-W., Chou, S.-C., Tsai, M.-L., et al. , 2017, Development of a new type of multifunctional fucoidan-based nanoparticles for anticancer drug delivery. *Carbohydrate Polymers*. 165 410–420.

[127] Shamay, Y., Elkabets, M., Li, H., Shah, J., Brook, S., Wang, F., et al. , 2016, P-selectin is a nanotherapeutic delivery target in the tumor microenvironment. *Science Translational Medicine*. 8 (345),.

[128] Aquib, M., Farooq, M., Mensura, S., Filli, K., Boakye-Yiadom, K., Kesse, M., et al. , 2019, A REVIEW ON THE CHEMOTHERAPEUTIC ROLE OF

FUCOIDAN IN CANCER AS NANOMEDICINE. *Research Journal of Life Sciences Bioinformatics Pharmaceutical and Chemical Sciences*.

[129] Fenech, M. , 2001, The role of folic acid and Vitamin B12 in genomic stability of human cells. *Mutation Research - Fundamental and Molecular Mechanisms of Mutagenesis*. 475 (1–2), 57–67.

[130] Bourassa, P. and Tajmir-Riahi, H.A. , 2015, Folic acid binds DNA and RNA at different locations. *International Journal of Biological Macromolecules*. 74 337–342.

[131] Shulpekova, Y., Nechaev, V., Kardasheva, S., Sedova, A., Kurbatova, A., Bueverova, E., et al. , 2021, The Concept of Folic Acid in Health and Disease. *Molecules*. 26 (12), 3731.

[132] Yi, Y.-S. , 2016, Folate Receptor-Targeted Diagnostics and Therapeutics for Inflammatory Diseases. *Immune Network*. 16 (6), 337.

[133] Walters, C.L., Arend, R.C., Armstrong, D.K., Naumann, R.W., and Alvarez, R.D. , 2013, Folate and folate receptor alpha antagonists mechanism of action in ovarian cancer. *Gynecologic Oncology*. 131 (2), 493–498.

[134] Eaton, B.E., Gold, L., and Zichi, D.A. , 1995, Let's get specific: the relationship between specificity and affinity. *Chemistry & Biology*. 2 (10), 633–638.

[135] Narmani, A., Rezvani, M., Farhood, B., Darkhor, P., Mohammadnejad, J., Amini, B., et al. , 2019, Folic acid functionalized nanoparticles as pharmaceutical carriers in drug delivery systems. *Drug Development Research*. 80 (4), 404–424.

[136] Ngo, H. V., Nguyen, H.D., and Lee, B.-J. , 2025, Hyaluronic acid conjugates with controlled oleic acid substitution as new nanomaterials for improving ocular co-delivery of cyclosporine A and oleic acid. *Asian Journal of Pharmaceutical Sciences*. 20 (1), 101009.

[137] Nguyen, N.T., Bui, Q.A., Nguyen, H.H.N., Nguyen, T.T., Ly, K.L., Tran, H.L.B., et al. , 2022, Curcuminoid Co-Loading Platinum Heparin-Poloxamer P403 Nanogels Increasing Effectiveness in Antitumor Activity. *Gels*. 8 (1), 59.

[138] Chou, T.-C., Motzer, R.J., Tong, Y., and Bosl, G.J. , 1994, Computerized Quantitation of Synergism and Antagonism of Taxol, Topotecan, and Cisplatin Against Human Teratocarcinoma Cell Growth: a Rational Approach to Clinical

Protocol Design. *JNCI Journal of the National Cancer Institute*. 86 (20), 1517–1524.

[139] Lee, S. and Lee, K. , 2020, pH-Sensitive Folic Acid Conjugated Alginate Nanoparticle for Induction of Cancer-Specific Fluorescence Imaging. *Pharmaceutics*. 12 (6), 537.

[140] Dong, Z., Wang, Q., and Du, Y. , 2006, Alginate/gelatin blend films and their properties for drug controlled release. *Journal of Membrane Science*. 280 (1–2), 37–44.

[141] Nguyen, D.T., Doan, H.P., Tran, T.K.N., Huynh, C.K., Tran, N.Q., and Dang, L.H. , 2023, Fucoidan and dendrimer-based nanocapsule exhibiting effectiveness in methotrexate controlled delivery towards rheumatoid arthritis treatment. *Advances in Natural Sciences: Nanoscience and Nanotechnology*. 14 (4), 045013.

[142] Zhang, J., Rana, S., Srivastava, R.S., and Misra, R.D.K. , 2008, On the chemical synthesis and drug delivery response of folate receptor-activated, polyethylene glycol-functionalized magnetite nanoparticles. *Acta Biomaterialia*. 4 (1), 40–48.

[143] Dang, L.H., Doan, P., Nhi, T.T.Y., Nguyen, D.T., Nguyen, B.T., Nguyen, T.P., et al. , 2021, Multifunctional injectable pluronic-cystamine-alginate-based hydrogel as a novel cellular delivery system towards tissue regeneration. *International Journal of Biological Macromolecules*. 185 592–603.

[144] Geethakumari, D., Veettil, S.P., Nair Chandrika, S.K., Sathyabhama, A.B., Joseph, R., Padmini, S.S., et al. , 2024, Development of polyethyleneimine cross-linked fucoidan nanoparticles as delivery systems for improved anticancer efficiency of cytarabine in breast adenocarcinoma cell lines. *RSC Pharmaceutics*. 1 (2), 305–316.

[145] Hao, J., Tong, T., Jin, K., Zhuang, Q., Han, T., Bi, Y., et al. , 2017, Folic acid-functionalized drug delivery platform of resveratrol based on Pluronic 127/D-α-tocopheryl polyethylene glycol 1000 succinate mixed micelles. *International Journal of Nanomedicine*. Volume 12 2279–2292.

[146] Pham, D.-C., Le Thi, P., Du Cao, V., Nguyen, H.D., Van Ngo, H., Hoang, A.Q., et al. , 2026, Effect of different poloxamers on anti-cancer activities of targeting

folic acid-fucoidan nanogels for multi-drug delivery. *International Journal of Biological Macromolecules*. 354 151417.

[147] Liu, K., Jiang, X., and Hunziker, P. , 2016, Carbohydrate-based amphiphilic nano delivery systems for cancer therapy. *Nanoscale*. 8 (36), 16091–16156.

[148] Midekessa, G., Godakumara, K., Ord, J., Viil, J., Lättekivi, F., Dissanayake, K., et al. , 2020, Zeta Potential of Extracellular Vesicles: Toward Understanding the Attributes that Determine Colloidal Stability. *ACS Omega*. 5 (27), 16701–16710.

[149] Nasr, M., Hashem, F., Teiama, M., Tantawy, N., and Abdelmoniem, R. , 2024, Folic acid grafted mixed polymeric micelles as a targeted delivery strategy for tamoxifen citrate in treatment of breast cancer. *Drug Delivery and Translational Research*. 14 (4), 945–958.

[150] Suthiwangcharoen, N. and Nagarajan, R. , 2014, Controlled design and construction of multifunctional nanoparticles by molecular self-assembly. *RSC Advances*. 4 (20), 10076.

[151] Gupta, R., Kalita, P., Patil, O., and Mohanty, S. , 2015, An investigation of folic acid–protein association sites and the effect of this association on folic acid self-assembly. *Journal of Molecular Modeling*. 21 (12), 308.

[152] Chen, X., Zou, L.-Q., Niu, J., Liu, W., Peng, S.-F., and Liu, C.-M. , 2015, The Stability, Sustained Release and Cellular Antioxidant Activity of Curcumin Nanoliposomes. *Molecules*. 20 (8), 14293–14311.

[153] Gil, M.S., Thambi, T., Phan, V.H.G., Kim, S.H., and Lee, D.S. , 2017, Injectable hydrogel-incorporated cancer cell-specific cisplatin releasing nanogels for targeted drug delivery. *Journal of Materials Chemistry B*. 5 (34), 7140–7152.

[154] Le Thi, P., Nguyen, H.T., Quoc Nguyen, V., Tran Nguyen, H., Thinh Nguyen, T., and Nguyen, V.T. , 2025, Enhanced cytotoxicity of cisplatin-loaded Brij S100-alginate-taurine nanogels against HeLa cervical cancer cells. *Nanotechnology*. 36 (41), 415601.

[155] Duan, X., He, C., Kron, S.J., and Lin, W. , 2016, Nanoparticle formulations of cisplatin for cancer therapy. *Wiley Interdisciplinary Reviews. Nanomedicine and Nanobiotechnology*. 8 (5), 776–91.

[156] Kharat, M., Du, Z., Zhang, G., and McClements, D.J. , 2017, Physical and Chemical Stability of Curcumin in Aqueous Solutions and Emulsions: Impact

of pH, Temperature, and Molecular Environment. *Journal of Agricultural and Food Chemistry*. 65 (8), 1525–1532.

[157] Nguyen, N.T., Luu, C.H., Hoang, A.Q., Ly, H.Q., Ton, T.P., Tran, N.Q., et al. , 2025, Development and Characterization of Folic Acid-Decorated Fucoidan-Poloxamer 407 Self-Assembled Nanogels Co-Loading Curcumin and Paclitaxel for Synergistically Enhanced Chemotherapeutic Efficacy. *Journal of Polymer Science*. 63 (11), 2405–2421.

[158] Patil, S., Sandberg, A., Heckert, E., Self, W., and Seal, S. , 2007, Protein adsorption and cellular uptake of cerium oxide nanoparticles as a function of zeta potential. *Biomaterials*. 28 (31), 4600–4607.

[159] Hoshyar, N., Gray, S., Han, H., and Bao, G. , 2016, The Effect of Nanoparticle Size on *In Vivo* Pharmacokinetics and Cellular Interaction. *Nanomedicine*. 11 (6), 673–692.

[160] Zheng, B. and McClements, D.J. , 2020, Formulation of More Efficacious Curcumin Delivery Systems Using Colloid Science: Enhanced Solubility, Stability, and Bioavailability. *Molecules*. 25 (12), 2791.

[161] Pham, D.-C., Du Cao, V., Hoang, A.Q., Nguyen, T.P., Tran, Q.-H., Nguyen, H.D., et al. , 2025, Gelatinized-polyoxyethylene (100) stearyl ether nanoformulation for enhancing distribution, bioavailability and stability of curcumin in cancer therapy. *Macromolecular Research*. 33 (10), 1375–1391.

[162] Li, Y., Wang, Z., Wei, Q., Luo, M., Huang, G., Sumer, B.D., et al. , 2016, Non-covalent interactions in controlling pH-responsive behaviors of self-assembled nanosystems. *Polymer Chemistry*. 7 (38), 5949–5956.

[163] Weber, M., Steinle, H., Golombek, S., Hann, L., Schlensak, C., Wendel, H.P., et al. , 2018, Blood-Contacting Biomaterials: In Vitro Evaluation of the Hemocompatibility. *Frontiers in Bioengineering and Biotechnology*. 6.

[164] Li, X., Yang, Z., Yang, K., Zhou, Y., Chen, X., Zhang, Y., et al. , 2009, Self-Assembled Polymeric Micellar Nanoparticles as Nanocarriers for Poorly Soluble Anticancer Drug Ethaselen. *Nanoscale Research Letters*. 4 (12), 1502.

[165] Xue, X., Yu, J.-L., Sun, D.-Q., Zou, W., Kong, F., Wu, J., et al. , 2013, Curcumin as a multidrug resistance modulator — A quick review. *Biomedicine & Preventive Nutrition*. 3 (2), 173–176.

[166] Zhou, Y., Ming, J., Deng, M., Li, Y., Li, B., Li, J., et al. , 2020. Chemically modified curcumin (CMC2.24) alleviates osteoarthritis progression by restoring cartilage homeostasis and inhibiting chondrocyte apoptosis via the NF-κB/HIF-2α axis. *Journal of Molecular Medicine*. 98 (10), 1479–1491.

[167] Shukla, S., Zaher, H., Hartz, A., Bauer, B., Ware, J.A., and Ambudkar, S. V , 2009. Curcumin inhibits the activity of ABCG2/BCRP1, a multidrug resistance-linked ABC drug transporter in mice. *Pharmaceutical Research*. 26 (2), 480–7.